Femtosecond Laser Interaction with Ultrathin Metal Films: Modifying Structure, Composition, and Morphology

by

Keegan James Schrider

A dissertation submitted in partial fulfillment
of the requirements for the degree of
Doctor of Philosophy
(Materials Science and Engineering)
in the University of Michigan
2017

Doctoral Committee:

Professor Steven M. Yalisove, Chair
Professor Roy Clarke
Professor Emmanuelle Marquis
Assistant Research Scientist Ben Torralva

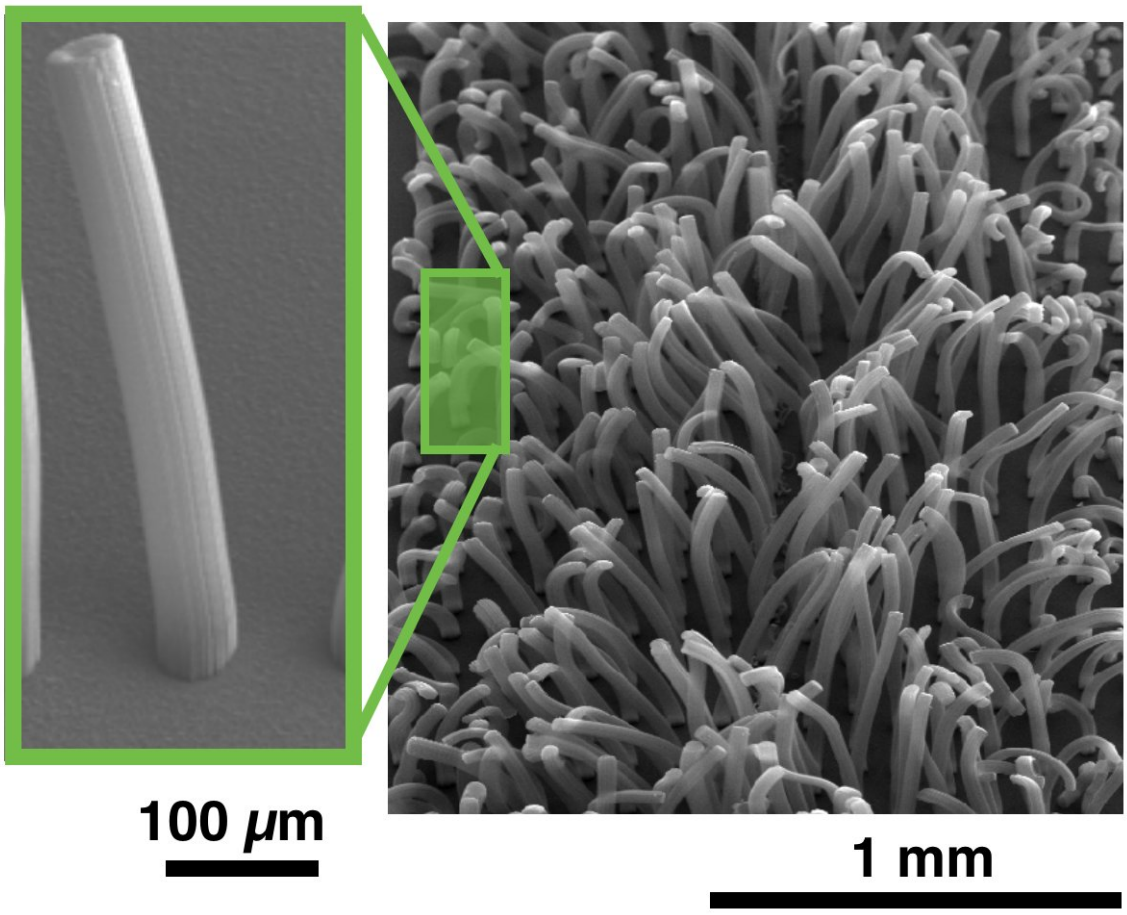
100 μm
1 mm

Keegan James Schrider

keegschr@umich.edu

ORCID iD: 0000-0001-5303-0615

DEDICATION

This dissertation is dedicated to my wife Beth and to my parents. Thank you for your love and support.

ACKNOWLEDGMENTS

Thank you Ben Torralva, Rico Cahyadi, Michael Abere, and Ryan Murphy for your support and insight.

Thank you Steve, you are a great teacher and mentor. I have enjoyed being an undergraduate student in your classes, a graduate student in your group, and your assistant in teaching materials science to undergraduates: you worked hard to get the best out of all three. I have seen your methods evolve in each area over the years and I believe many students have benefited from the care you give to education.

TABLE OF CONTENTS

LIST OF FIGURES

LIST OF APPENDICES

LIST OF ABBREVIATIONS

STEM Scanning Transmission Electron Microscopy

AFM Atomic Force Microscopy

TEM Transmission Electron Microscopy

SEM Scanning Electron Microscopy

LIFT Laser Induced Forward Transfer

CNT Carbon Nanotube

HAADF High Angle Annular Dark Field

CVD Chemical Vapor Deposition

PLV Pulsed Laser Vaporization

SWNT Single Walled Nanotube

RMS Root Mean Square

sccm Standard Cubic Centimeter per Minute

MD Molecular Dynamics

ND Neutral Density

ASE Amplified Spontaneous Emission

HRTEM High Resolution Transmission Electron Microscopy

FFT Fast Fourier Transform

EDS Energy-dispersive X-ray Spectroscopy

APT Atom Probe Tomography

XRD X-Ray Diffraction

ABSTRACT

Femtosecond laser pulses allow for the study of materials in unique, and often extreme, conditions. As research regarding femtosecond laser interaction with materials progresses, the mechanisms for damage and modification are better understood. As a result, more complicated configurations of the target material can be explored often revealing new routes to modify materials. This work explores femtosecond laser irradiation of thin metal films and characterizes the resulting morphology, microstructure, and composition using optical microscopy, scanning electron microscopy, atomic force microscopy, transmission electron microscopy, and time-resolved pump-probe microscopy.

Three areas are addressed; the removal of ultrathin metal films from non-absorbing substrates, mixing of multilayer Ni-W and Ni-Ag films to form thermally stable nanocrystalline alloys, and in-situ irradiation of Fe catalyst thin films to stimulate chemical vapor deposition of carbon nanotubes. A mechanistic understanding of the materials response was pursued for each case studied including the role of interfaces, and the interaction of solid, liquid, and gaseous phases formed by irradiation.

The dynamics of femtosecond laser removal of ultrathin Ni films from glass substrates were measured using time-resolved pump-probe microscopy. Within 50 ps of irradiation the film-substrate interface separated and the removed layer accelerated to a constant velocity, faster than predicted by previous models. The Ni film was driven into extreme thermodynamic states after irradiation that caused the Ni film to rapidly decompose into a liquid-vapor mixture, similar to spinodal decomposition. Spinodal-like decomposition of a bulk metal after irradiation causes homogeneous nucleation of vapor; in this study

spinodal-like decomposition caused heterogeneous nucleation at the Ni-substrate interface at relatively low fluences, broadening the range of temperatures to observe this process compared to previous studies. Studying the removal of ultrathin films provides a route to explore the extreme states of matter that occur after femtosecond laser irradiation.

It has been predicted in previous studies that rapid cooling after femtosecond laser irradiation can drive homogeneous solidification in pure metals to form nanocrystalline material at the surface, however this is not generally observed. Ultrathin, multilayer films of Ni-W and Ni-Ag were irradiated with a single pulse and the resulting morphology and microstructure of the films were studied at a range of laser fluences. For Ni-W, a thermally stable nanocrystalline film was formed possibly due to solute stabilization of grain boundaries. The method for femtosecond laser mixing of multilayer metal thin films can be applied to create nanocrystalline surface layers for a wide range of alloy compositions that possess robust mechanical properties, increased corrosion resistance, unique magnetic properties, and are used as catalyst.

Irradiation of carbon nanotube catalyst during Chemical Vapor Deposition stimulates the growth of aligned forests and in some cases increasing the terminal length of the aligned forest by up to 150X. It is shown that the femtosecond laser stimulates growth by combining Pulsed Laser Vaporization synthesis and Chemical Vapor Deposition, vaporizing the initial population of carbon nanotubes to jump start forest growth. This method provides a novel and simple route to efficient growth in systems where the static growth parameters are not optimized. Laser irradiation may also be used to pattern growth of aligned CNT forests without pre-pattering catalyst via photolithography, or post processing.

CHAPTER 1

Introduction

Femtosecond laser pulses allow for the study of materials in unique, and often extreme, conditions. The femtosecond laser is a variety of pulsed laser where energy is compressed into a period on the order of 100 fs (10^{-13} s) making it possible to achieve extremely high maximum intensities with relatively low energy pulses. While high power CW lasers for marking or laser cutting reach 1000 W, the peak power of a femtosecond laser pulse is routinely higher than 10^{12} W. This class of laser has opened a new field of research in laser-material interaction making it possible to add significant energy to the target material before mechanical or thermal responses can take place[1]. In metals, light is absorbed primarily by conduction electrons during the term of the laser pulse. Energy absorbed by the electrons is transferred to the ionized atoms via electron-phonon coupling which occurs over a period of several picoseconds. The transfer of energy between the electrons and ions increases both the temperature and pressure in the target material to high values. In this work phenomena are studied where the energy deposited after irradiation is near the threshold for material removal via liquid spallation; in that regime the material reaches temperatures from 4,000 to 10,000 K and pressures of 1 GPa[1]. The relaxation of the target material from far from equilibrium pressures and temperatures drives dynamic processes and final states that are unique to femtosecond laser irradiation. For longer laser pulses, such as nanosecond lasers, the deposition of energy, heating of the lattice, and the mechanical response occur simultaneously. At moderate intensities the target material is

close to equilibrium[2]. Though ns pulsed lasers can be used to reach the same extreme conditions as femtosecond laser irradiation, the total energy of the pulse must be much higher resulting in an excessive melting depth and excessive material removal.

This dissertation explores femtosecond laser irradiation as a route to modify the morphology, microstructure, and composition of thin metal films. Three areas are addressed: the removal of ultrathin metal films from non-absorbing substrates, mixing of multilayer Ni-W and Ni-Ag films to form thermally stable nanocrystalline alloys, and in-situ irradiation of Fe catalyst thin films to stimulate chemical vapor deposition of carbon nanotubes. A mechanistic understanding of the materials response was pursued for each case studied including the role of interfaces, and the interaction of solid, liquid, and gaseous phases formed by irradiation.

The mechanism for removal of ultrathin metal films is frequently exploited in the production of patterned thin films for microelectronic devices by subtractive machining of thin films or Laser Induced Forward Transfer (LIFT) of layers or nanoparticles[3–5]. As the thickness of films nears the excitation depth of the laser pulse the mechanism for removal is less clearly attributable to a single mechanism, possibly occurring by liquid spallation or vaporization at the interface. This work uses time-resolved microscopy to put bounds on the time for separation and acceleration of removed layers, and measure the velocity of films removed from an interface and use those results to differentiate between the possible mechanisms. Investigations of removal at interfaces indicate that separation is driven by a phase transformation that occurs due to the unique evolution of the thermodynamic state of material during the excitation and relaxation driven by femtosecond laser irradiation.

Previous studies had shown that alloying at metal-metal interfaces can be driven by a femtosecond pulse[6, 7]. The earlier observation of a rapid heterogeneous phase transformation for removal of metal films, extreme thermodynamic states observed in simulations of bulk and thin film irradiation[8–13], and the high heating and quenching rates after pulse-laser irradiation together inspired an investigation to produce alloys of metals be-

yond their equilibrium solubility by irradiating layered metal films. The Ni-W system was chosen because nanocrystalline alloys of Ni-W had been produced by electrodeposition by precisely controlling the composition of the deposited layer[14]. In electrodeposited or sputtered Ni-W, nanocrystalline Ni grains are stabilized because W solute atoms segregate to grain boundaries, reducing the grain boundary energy and preventing coarsening[15–17]. It is understood that rapid quenching of materials after femtosecond laser irradiation should lead to the formation of nanocrystalline material via the homogeneous nucleation of solid crystals in the melt, as in the synthesis of nanocrystalline and glassy materials via melt spinning or splat quenching. However, nanocrystalline materials is not observed experimentally at the surface of metals after femtosecond laser irradiation. It is likely that the nanocrystalline material is consumed by larger grains in the bulk because pure materials coarsen at low temperature. In this dissertation multilayer Ni-W films with controlled thickness of each material were used as an alternative approach to control the overall composition of Ni-W films, then the films were irradiated. This dissertation presents the first observation of the formation of thermally stable nanocrystalline microstructures at the surface of metals after femtosecond laser materials processing. Using the Ni-W system two aspects of the materials response to irradiation were considered: what fluence range heats the multilayer Ni-W films for mixing and will the solidification of the mixed material permit forming nanocrystalline microstructure that is thermally stable. It was then considered if the high degree of mixing that is observed in the Ni-W system can possibly be replicated in the immiscible Ni-Ag system.

Carbon nanotubes can be produced by a variety of methods including electric Arc Discharge, Pulsed Laser Vaporization (PLV), and CVD. PLV synthesis of CNTs can be performed with continuous wave and pulsed lasers[18]. As the carbon bonds reform new allotropes of carbon including Fullerenes and CNTs can form. Often a catalyst, such as metal nanoparticles, are included in this process because they absorb the carbon and precipitate a nanotube[19]. Similarly, CVD often uses a metal nanoparticle as a catalyst to break down

gas molecules containing carbon, absorb carbon, and precipitate a nanotube[20]. The process of CVD is limited by a process called poisoning, eventually the reaction at the catalyst stops and CNT growth is terminated. The mechanism for this process is not fully understood but one common model is that amorphous carbon coats the catalyst and prevents the absorption of new carbon to extend the nanotube[21]. The femtosecond laser was proposed as a means to remove amorphous carbon and reactivate catalyst, or to prevent catalyst poisoning altogether by irradiating material during growth. In pursuing that question it was observed that irradiation of catalyst with a single pulse at the beginning of CVD growth greatly enhanced the growth of CNT forests for up to 30 minutes and yielding forests up to 150 times taller. For the first time pulsed laser irradiation was combined with an active CVD process during nucleation; it is shown that technique increases the number of catalyst nanoparticles that produce CNTs and consequently improve self-organization of CNTs into aligned forests.

The goals of this thesis :

Determine the mechanism for separation of ultrathin metal films from a substrate after irradiation by

1. Observing the dynamics of removal for ultrathin Ni thin film on glass substrates using time-resolved pump-probe microscopy.

2. Identifying a mechanism for the rapid formation of vapor that severs the Ni-substrate interface.

Explore femtosecond laser irradiation of ultrathin multilayer, multicomponent metal films as a technique to form alloys of metals with limited solubility by

1. Demonstrating that homogeneous mixtures of elements can be formed by femtosecond laser melting and quenching.

2. Observing the morphology of the removal craters and microstructure of alloys formed via irradiation in terms of the local fluence.

3. Defining the conditions after irradiation that lead to the observed range of removal craters and microstructures in multicomponent, multilayer metal films.

Explore the effect of irradiation on Chemical Vapor Deposition Carbon Nanotubes by

1. Demonstrating that femtosecond laser irradiation of catalyst during CVD growth dramatically increases the terminal length of aligned CNT forests.

2. Demonstrating that the enhancement of forest growth is highly dependent on the dynamics of nucleation and growth of CNTs.

3. Identifying the mechanism for enhancement of aligned forest growth as laser stimulated nucleation of CNTs via combination of PLV and CVD synthesis.

This dissertation explores the effect of irradiation with a single femtosecond laser pulse on the microstructure and composition of thin metal films using time resolved and post mortem microscopy methods. The experimental results in this dissertation provide a fundamental understanding of materials response to femtosecond laser irradiation, as in the case of spinodal-like decomposition of metal stabilized by an interface. Simultaneously, new materials processing techniques were discovered as in the case of laser stimulated nucleation of CNTs during thermal CVD or the formation of nanocrystalline alloy films after irradiation.

Fs-laser mixing of ultrathin multilayer films is a novel method to study alloy formation with a wide range of compositions, particularly any composition that is difficult to synthesize using other alloying methods. In this dissertation the method is applied to mix

multilayer Ni-W films on Ni substrates and create a nanocrystalline film on the Ni surface. Fs-laser synthesized nanocrystalline coatings could be produced on metal surfaces to take advantage of their useful mechanical, chemical or magnetic properties. The same method could be potentially applied to create thin films of almost any alloy system; it is only necessary that the materials can be deposited in a sufficiently thin film on the same substrate. This technique could be used to study the formation of alloys with unique compositions such as typically immiscible alloys[22–24].

Enhancing CNT nucleation with the femtosecond laser provides a novel route to improve CVD growth in situations where the chamber and growth recipe are not optimized, and also compensate for natural variation in growth runs, making efficient growth of aligned CNT forests more easy to achieve. New methods to widen the range of parameters for efficient growth are critical for the widespread application of CNT based materials that are derived from aligned forests, including fibers, sheets, or coatings[25–27]. Additionally the methods demonstrated here may be used to pattern growth of aligned CNT forests without pre-pattering catalyst, masking, or post processing. It is also shown here that enhanced growth can be patterned by using diffraction or photo lithography masks to change the spatial distribution of the laser energy at the surface.

References

1. *Lasers in Materials Science* (eds Castillejo, M., Ossi, P. M. & Zhigilei, L.) (Springer International Publishing, Cham, 2014).
2. Lorazo, P., Lewis, L. J. & Meunier, M. Thermodynamic pathways to melting, ablation, and solidification in absorbing solids under pulsed laser irradiation. *Physical Review B* **73,** 134108 (Apr. 14, 2006).
3. Adrian, F. J. A study of the mechanism of metal deposition by the laser-induced forward transfer process. *Journal of Vacuum Science & Technology B: Microelectronics and Nanometer Structures* **5,** 1490–1494 (Sept. 1987).
4. Banks, D. P., Grivas, C., Mills, J. D., Eason, R. W. & Zergioti, I. Nanodroplets deposited in microarrays by femtosecond Ti:sapphire laser-induced forward transfer. *Applied Physics Letters* **89,** 193107 (2006).
5. Kaur, K. S., Fardel, R., May-Smith, T. C., Nagel, M., Banks, D. P., Grivas, C., Lippert, T. & Eason, R. W. Shadowgraphic studies of triazene assisted laser-induced forward transfer of ceramic thin films. *Journal of Applied Physics* **105,** 113119 (2009).
6. Gurevich, E. L., Kittel, S. & Hergenröder, R. Experimental and numerical study of surface alloying by femtosecond laser radiation. *Applied Surface Science* **258,** 2576–2579 (Jan. 15, 2012).
7. Thomas, D. A., Lin, Z., Zhigilei, L. V., Gurevich, E. L., Kittel, S. & Hergenröder, R. Atomistic modeling of femtosecond laser-induced melting and atomic mixing in Au film – Cu substrate system. *Applied Surface Science* **255,** 9605–9612 (Sept. 2009).
8. Cheng, C. R. & Xu, X. F. Mechanisms of decomposition of metal during femtosecond laser ablation. *Physical Review B* **72,** 165415 (Oct. 2005).
9. Povarnitsyn, M. E., Itina, T. E., Sentis, M., Khishchenko, K. V. & Levashov, P. R. Material decomposition mechanisms in femtosecond laser interactions with metals. *Physical Review B* **75,** 235414 (June 2007).
10. Vidal, F., Johnston, T. W., Laville, S., Barthélemy, O., Chaker, M., Le Drogoff, B., Margot, J. & Sabsabi, M. Critical-Point Phase Separation in Laser Ablation of Conductors. *Physical Review Letters* **86,** 2573–2576 (Mar. 19, 2001).
11. Colombier, J.-P., Combis, P., Stoian, R. & Audouard, E. High shock release in ultrafast laser irradiated metals: Scenario for material ejection. *Physical Review B* **75,** 104105 (2007).
12. Perez, D. & Lewis, L. Thermodynamic evolution of materials during laser ablation under pico and femtosecond pulses. *Applied Physics A* **79** (July 26, 2004).

13. Lorazo, P., Lewis, L. & Meunier, M. Thermodynamic pathways to melting, ablation, and solidification in absorbing solids under pulsed laser irradiation. *Physical Review B* **73,** 134108 (Apr. 2006).

14. Chookajorn, T., Murdoch, H. A. & Schuh, C. A. Design of Stable Nanocrystalline Alloys. *Science* **337,** 951–954 (Aug. 24, 2012).

15. Weissmüller, J. Alloy effects in nanostructures. *Nanostructured Materials. Proceedings of the First International Conference on Nanostructured Materials* **3,** 261–272 (Jan. 1, 1993).

16. Detor, A. & Schuh, C. Tailoring and patterning the grain size of nanocrystalline alloys. *Acta Materialia* **55,** 371–379 (Jan. 2007).

17. Detor, A. J., Miller, M. K. & Schuh, C. A. Solute distribution in nanocrystalline Ni-W alloys examined through atom probe tomography. *Philosophical Magazine* **86,** 4459–4475 (Oct. 1, 2006).

18. Szabó, A., Perri, C., Csató, A., Giordano, G., Vuono, D. & Nagy, J. B. Synthesis Methods of Carbon Nanotubes and Related Materials. *Materials* **3,** 3092–3140 (May 7, 2010).

19. Geohegan, D. B., Puretzky, A. A., Rouleau, C., Jackson, J., Eres, G., Liu, Z., Styers-Barnett, D., Hu, H., Zhao, B. & Ivanov, I. in *Laser-Surface Interactions for New Materials Production* 1–17 (Springer, 2010).

20. Dupuis, A.-C. The catalyst in the CCVD of carbon nanotubes—a review. *Progress in Materials Science* **50,** 929–961 (Nov. 2005).

21. Stadermann, M., Sherlock, S. P., In, J.-B., Fornasiero, F., Park, H. G., Artyukhin, A. B., Wang, Y., De Yoreo, J. J., Grigoropoulos, C. P., Bakajin, O., Chernov, A. A. & Noy, A. Mechanism and Kinetics of Growth Termination in Controlled Chemical Vapor Deposition Growth of Multiwall Carbon Nanotube Arrays. *Nano Letters* **9,** 738–744 (Feb. 11, 2009).

22. Wang, F. E. *Bonding Theory for Metals and Alloys* 219 pp. (Gulf Professional Publishing, Sept. 30, 2005).

23. Ratke, L. & Diefenbach, S. Liquid immiscible alloys. *Materials Science and Engineering: R: Reports* **15,** 263–347 (Dec. 15, 1995).

24. Ma, E. Alloys created between immiscible elements. *Progress in Materials Science* **50,** 413–509 (May 2005).

25. Zhang, X., Li, Q., Tu, Y., Li, Y., Coulter, J. Y., Zheng, L., Zhao, Y., Jia, Q., Peterson, D. E. & Zhu, Y. Strong Carbon-Nanotube Fibers Spun from Long Carbon-Nanotube Arrays. *Small* **3,** 244–248 (Feb. 5, 2007).

26. Zhang, M. Strong, Transparent, Multifunctional, Carbon Nanotube Sheets. *Science* **309,** 1215–1219 (Aug. 19, 2005).

27. Volder, M. F. L. D., Tawfick, S. H., Baughman, R. H. & Hart, A. J. Carbon Nanotubes: Present and Future Commercial Applications. *Science* **339,** 535–539 (Feb. 1, 2013).

CHAPTER 2

Background

A review of prior research regarding the interaction of fs-laser pulses with solid materials is presented in this chapter with emphasis on materials on the nanoscale including thin metal films, metal nanoparticles, and CNTs. The influence of interfaces on absorption, energy deposition, and the mechanisms for damage will be addressed where appropriate in order to understand the thresholds for damage, dynamics of damage, and resulting morphology presented in this dissertation. A review of CNT growth methods, previous experiments using lasers to drive or modify growth, and laser interaction with CNTs is also presented.

2.1 Material Response to Femtosecond Laser Irradiation

This section will give an overview of the interaction of a fs pulse with metals, including the absorption and redistribution of laser energy, the evolution of stress and strain, and phase transformations that occur after irradiation.

2.1.1 Absorption of Radiation and Heating

Femtosecond lasers like that used in this work have a pulse duration of 150 fs and a pulse energy of more than 1 mJ. When focused the maximum irradiance of a pulse can reach 10^{14} W/cm^2. For femtosecond lasers energy is absorbed primarily by electrons, not by the lattice. For the most part, the lattice remains unexcited until after the laser pulse has passed

and absorption is over. The energetic electrons couple with phonons to transfer energy to the lattice and begin the major relaxation processes like thermal transport, hydrodynamic motion, and phase transformation. In many cases the absorption of light and material response can be considered largely separate; the fluence deposited in the material is the most important quantity and is expressed in J/cm^2.

Radiation is absorbed by electrons that are excited to higher energy states. In metals, femtosecond laser energy is linearly absorbed by free electrons. The skin depth is the point where the intensity of the incoming laser light has dropped to 1/e^2 of its initial value and 86% of the laser energy has been deposited. The definition of the skin depth is given in equation 2.1, where λ is the laser wavelength and k is the imaginary component of the refractive index.

$$l_s = \frac{\lambda}{k4\pi} \tag{2.1}$$

Within 200 fs the excited electrons thermalize[1] via electron-electron collisions and attain a temperature in excess of 11,000 K[2, 3]. Ballistic electrons[4, 5] and high temperature electrons[6–8] have a mean free path on the order of 100 nm and greatly increase the depth where energy is deposited in the electron system[9] and ultimately the temperature profile of the lattice[10].

While the laser pulse is "on," and light is absorbed by the electrons, the lattice remains close to room temperature. The separate high temperature electrons and a room temperature lattice are treated theoretically using the two-temperature model[11]. The lattice is heated as the electron and lattice temperatures equilibrate through electron-phonon coupling[9], rapidly heating the lattice over several picoseconds after irradiation[10, 12, 13]. With a sufficiently short pulse the heating rate of the lattice is limited by the electron-phonon coupling coefficient. The rapid transfer of energy between the electrons and lattice drive a mechanical response and phase transformation that occur far from equilibrium unlike with other types of laser excitation, e.g. nanosecond laser excitation[2].

Aspects of femtosecond laser interaction with thin films are still being explored, including the effect of the evolving absorption coefficient[14], electrons scattering at interfaces[15], and electron energy loss to the substrate[15].

2.1.2 Evolution of Stress and Strain

Over the few picoseconds it takes for the electron system and lattice to equilibrate, the temperature of the lattice rises without a significant increase in volume, so the pressure in the heated layer rises. Since the pressure at the surface of the target material must remain zero, a sharp pressure gradient is created across the free surface. The high pressure in the heated layer relaxes via expansion in the direction the pressure gradient, toward the free surface. There is also a pressure gradient in the target material below the heated surface layer and a compressive wave is launched into the bulk[16–18]. Behind the compressive wave an unloading rarefaction wave is created putting the material under tensile stress. As the tensile wave travels deeper into the material it forms a trough that broadens and intensifies.

At sufficiently high fluences, the mechanical response to irradiation is strong enough to overcome the cohesive strength of the target. This process is called spallation and is the dominant mechanism for material removal in metals. Typically spallation occurs above the threshold to melt, and the compressive and tensile stress evolves in the thin molten layer at the surface. As the tensile trough intensifies, free volume in the hot liquid coalesces through the homogeneous nucleation of voids. The voids perforate the liquid along a plane[17, 19–21] reducing the cross sectional area of liquid along that plane and weakening it. As the cross sectional area falls the tensile stress increases and eventually exceeds the cohesive strength of the liquid; the remaining liquid tendrils break similar to cavitation[22] releasing the upper layer of liquid.

2.1.3 Femtosecond Laser Driven Phase Transformations

Femtosecond laser irradiation drives phase transformations by a variety of mechanisms. At a threshold fluence below liquid spallation, melting occurs homogeneously[13] in the heated material where the energy deposited in the lattice exceeds the heat of fusion of the metal[2].

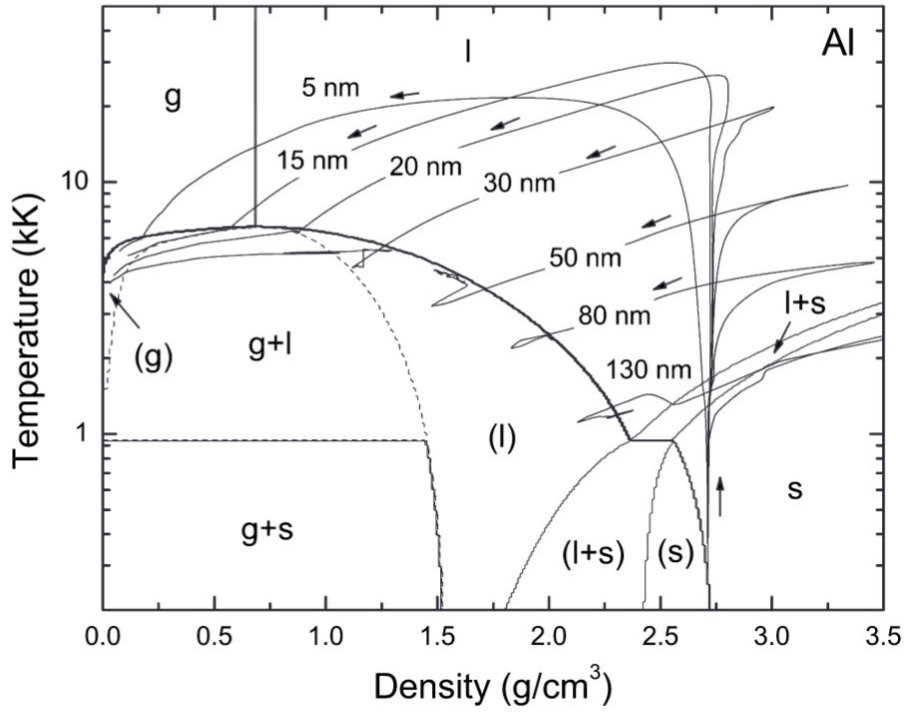

Figure 2.1: Hydrodynamic simulation of Al irradiated with 5 J/cm^2 peak fluence showing trajectories in density/temperature phase diagram. Trajectories represent the time evolution of density and temperature at different depths in a bulk Aluminum target irradiated with a peak fluence of 5 J/cm^2. In the diagram the solid curves represent the phase boundaries and the dashed curve represents the spinodal. The phases are g, stable gas; l, stable liquid; s,stable solid; l+s, stable melting; g+l, liquid-gas mixture; g+s: solid-gas mixture; (g), metastable gas; (l), metastable liquid; (l+s), metastable melting; (s), metastable solid. The phase trajectories correspond to depths of 5, 15, 20, 30, 50, 80, and 130 nm from the initial target surface. Arrows along the trajectories show the flow of time. The laser pulse is 100 fs long and the center wavelength is 800 nm. Reprinted from [23]

As fluence is increased irradiation drives the liquid to vapor transition; this occurs in several regimes and depends on both the thermal and mechanical evolution of the mate-

rial. The liquid to vapor transformation is most easily discussed in terms of the T-ρ phase diagram, shown for aluminum in Figure 2.1. Of particular importance to understand the laser driven liquid/vapor transformation is the lower density region where the liquid and vapor phases coexist called the vapor dome. The peak of the vapor dome is called the critical point, above the vapor dome the liquid and vapor are indistinguishable at constant temperature. The trajectories in Figure 2.1 represent hydrodynamic simulations of the time evolution of density and temperature at different depths in a bulk Aluminum target irradiated with a peak fluence of 5 J/cm^2[23]. Initially the material increases in temperature at solid density, crosses the liquid-solid boundary, and the superheated material melts homogeneously. In the deeper simulated layers, where the energy per unit volume is relatively low, the compressive and tensile waves cause the density to rise then to fall. The material briefly enters the vapor dome then equilibrates to the liquid line and will eventually cool returning to the solid state. Within the vapor dome the liquid is metastable: if the material could be held at this point for an infinite time the liquid would decompose into a coexistence of liquid and vapor. During liquid spallation, the tensile stress is intensified in a plane due to the generation of voids and the reduced cross sectional area. Cavitation occurs since some trajectories in that region drop in density and pass through the vapor dome[24], that material transforms to the vapor phase instead of returning to the liquid phase and break the connection between the upper and lower layers of the liquid.

At layers closer to the surface where the absorbed energy and the peak temperature of the liquid are much higher, such as the trajectories at 20 and 30 nm in Figure 2.1, the material enters the vapor dome near the critical point. The liquid excited into this region is unstable and local variations in the density and temperature[25] allow the material to spontaneously decompose into a mixture of the liquid and vapor phases, similar to spinodal decomposition, called critical point phase separation[16, 23, 25, 26]. The critical point phase separation region is usually defined as the area inside the vapor dome within 10% of the critical point.

If the material is excited to extremely high energies it will transition directly to the vapor phase passing over the critical point as shown with the trajectory at 5 and 15 nm in Figure 2.1. This is called explosive boiling and is characterized by the homogeneous nucleation of vapor forming a mixture of liquid droplets and vapor that are ejected from the material[23, 26, 27].

The processes of explosive boiling or critical point phase separation share some similarities, such as a rapid and uniform decomposition into liquid and vapor and the emission of droplets from the surface. As a result there is some confusion regarding terminology, like the term phase explosion sometimes being used to refer to either process as noted by Povarnitsyn et. al.[23].

For longer pulses where heating and expansion occur concurrently and the trajectories do not enter the vapor dome as significantly as with femtosecond pulses[28]. This is especially true at lower fluences where the trajectories enter the vapor dome at lower temperature where the tensile waves drives the density of the liquid toward lower values, and the strong tensile wave is a consequence of relaxation from the far from equilibrium temperature and pressure after femtosecond laser irradiation. The effects of the unique relaxation dynamics after femtosecond laser irradiation are explored in Chapter 4 regarding the liquid to vapor phase transformation that occurs in the vapor dome, and again in Chapter 5 regarding the effect of the highly non-equilibrium relaxation path and the vapor dome on binary alloys.

2.2 Fs-Laser Damage Thresholds of Ultrathin Films

The damage threshold of metal films is lower than bulk materials due to several factors[4, 7, 29]. First, the specific energy deposited by the laser increases as the film thickness is reduced. In a bulk material high energy density at the surface will equilibrate with lower energy density deeper in the material. As the film thickness is reduced the low energy tail

is not absorbed, and the high energy deposited in the surface layer is not redistributed.

This section reviews previous work regarding femtosecond laser irradiation of films including the effect on the distribution of energy, the evolution of stress and strain, and the observed damage mechanisms.

2.2.1 Distribution of Laser Energy in Ultrathin Metal Films

Here, an ultrathin film is defined as sufficiently thin so that it approaches a uniform temperature distribution after irradiation due to electron transport and thermal transport, before major relaxation processes like hydrodynamic flow or vaporization. Electron transport before electron-phonon coupling is the primary factor in the redistribution of absorbed laser energy. Gold, a noble metal with a longer ballistic electron range and lower coupling coefficient, can be considered ultrathin below 443 nm and Nickel, a transition metal with a higher coupling coefficient, can be considered ultrathin below 31 nm[7]. Simulations also show that the critical thickness of a Ni film to transition to a uniform energy distribution and damage mechanism is between 50 and 20 nm [30, 31].

2.2.2 Confinement of Stress

The compressive and tensile waves launched after irradiation of a bulk material are transmitted into the underlying solid material. In a thin film, the strain pulse can be reflected by a boundary either with a free surface or the substrate material. Molecular Dynamics (MD) simulations of free standing ultrathin metal films show that after irradiation above the liquid spallation threshold the laser energy is distributed uniformly and stress in the film evolves symmetrically[22, 31]. Under these conditions the maximum tensile stress occurs at the midpoint of the film and the film breaks into two layers with equal thickness.

In other MD simulations of thicker suspended films show that the compressive wave launched from the from irradiated surface of the film travels to, and is reflected from the rear free surface[17]. Upon reflection from the rear free surface, the sign of the compressive

pressure wave reverses and a tensile wave travels back into the film. The unloading tensile wave and the counterpropagating reflected wave can then constructively interfere creating a maximum tensile stress. The location of the maximum is dependent on the film thickness, speed of sound, and relative intensity of each tensile wave. For thin metal films on a substrate the strain pulse is reflected or transmitted at a solid-solid interface depending on the acoustic impedances of the film and the substrate materials. The acoustic impedance of a material is equal to ρc, where ρ is the density of the material and c is the speed of sound. The ratio of the reflected intensity of an acoustic wave at an interface is give in Equation 2.2. R is the ratio of the reflected and incident intensities for a wave propagating from the film with density ρ_{f} and speed of sound $\mathrm{c_f}$ to a substrate with density ρ_{s} and speed of sound $\mathrm{c_s}$. The reflected wave changes sign when it is reflected from a substrate with a lower acoustic impedance, similar to the case of a suspended film. The type of substrate will determine the sign and intensity of the reflected wave and therefore significantly change the location and intensity of the maximum tensile stress in the film.

$$R = \frac{(\rho_2 c_2 - \rho_1 c_1)^2}{(\rho_2 c_2 + \rho_1 c_1)^2} \tag{2.2}$$

For ultrathin films on a substrate, it has been observed in MD simulations[32] and experimentally[29] that the depth removed by liquid spallation is slightly less than half of the film thickness.

2.2.3 The Effect of an Interface on Femtosecond Laser Induced Damage

Interfaces can play a significant role in the removal mechanisms of ultrathin films having an effect on the absorption of light by the film, changing the mechanical response of the film by reflecting or transmitting pressure waves, or providing a stable location for heterogeneous phase transformations. In an ultrathin metal film, a significant amount of light still reaches

the film substrate interface and is reflected. It has been shown that the damage threshold of ultrathin Ni is proportional to the absorbance of the film calculated using equations for thin film interference[33, 34].

Interfaces influence the mechanism of laser damage by serving as a location for increased light absorption, creating a location for heterogeneous nucleation in laser induced phase transformations[29, 32], or as a discontinuity in the strength of material[35]. Distinguishing between these removal mechanisms can be complicated and is examined in Chapter 4.

Taking advantage of preferential removal from interfaces, femtosecond laser irradiation of thin films of metal, dielectrics, or ceramics is used as method to create nanoparticles[36] or to deposit thin films by LIFT. Femtosecond LIFT has the advantage that it is possible to remove materials "gently," without destroying their structure.

Research into the effect of interfaces on the absorption and distribution of laser energy is ongoing. Recent work has shown that interfaces can increase light absorption and scatter or reflect electrons[37], ultimately influencing energy deposition in the lattice near the substrate.

It has been observed that melting of multilayer materials can be used to create solid solutions. In the Mo/Si[38] system an amorphous solution was created within 20 nm of the irradiated surface. Reactive foils of CoAl[39] and AlPt[40], where mixing is an exothermic reaction, were mixed after irradiation with a single ultrashort pulse. At high fluence, exothermic mixing in the irradiated spot was sufficient to ignite the film, propagating the reaction throughout the target material. Simulations[41] and experiments[42] show that femtosecond laser irradiation of an Au/Cu bilayer, above the threshold to melt the interface, causes interdiffusion of Cu/Au in the melt zone. The mixed composition is retained after resolidification. The systems investigated previously alloy spontaneously and form stable compounds. Chapters 5 and 6 of this dissertation explore mixing of multilayer materials whose elements/compositions are immiscible.

2.2.4 Pump-probe Microscopy of Thin Film Removal

The dynamics of material removal after irradiation can be studied using pump-probe microscopy. A pump-probe experiment refers to the use of a laser to excite a response in a sample that is repeatable, and then uses a probe with a variable delay to collect information about the state of the material with some time resolution. Pump-probe imaging uses the probe pulse as a fast illumination source to create an image, similar to a flash bulb. Pump-probe imaging of materials irradiated by femtosecond pulses was first applied to measure the dynamics of electron and lattice heating and melting[43, 44]. In studies where the peak fluence exceeded the liquid spallation threshold, concentric interference fringes were observed in the crater area[18, 45–49]. Fringes in the liquid spallation region are generated similarly to thin film interference. Instead of reflection occurring at the upper and lower bounds of a single layer, light is reflected by the ejected liquid "spall" layer and the stationary surface of the sample. As the displacement of the moving layer increases, the phase difference between the reflected rays increases. With increasing phase difference interference causes successive maxima and minima in the reflected intensity. It has been shown in previous studies that the speed of material ejected after femtosecond laser irradiation is proportional to the local fluence of the laser pulse[46]. Since the laser pulse has a Gaussian spatial distribution, the ejected layer forms a dome with a displacement proportional to the local fluence. Interference maxima and minima form concentric rings marking incremental displacements of the ejected film, similar to a contour map. Concentric interference rings of this same type had previously been used by Issac Newton to characterize the curvature of lenses, and are called Newton's rings[50]. Other pump-probe studies using an imaging interferometer confirm that after irradiation with a Gaussian pulse liquid is ejected in a dome[51].

In previous work Newton's rings were used to measure the displacement of thin glass films from a surface after femtosecond laser irradiation[52, 53]. The removal of glass films from silicon substrate was studied to determine what fills the gap between the ejected ma-

terial and the silicon surface during removal near the liquid spallation threshold of silicon. The refractive index of the gap material was measured to be 0.9 and it was suggested that the gap material was a plasma.

Pump-probe microscopy was performed of molybdenum films 320 to 500 nm thick on glass substrates[54, 55]. Experiments show that ultrathin Mo films would be less than 66 nm thick[7]. The films were irradiated through the glass substrate, as they would be during LIFT, to study material ejection to the confinement of vaporized material at the interface. The time resolved reflectivity was used to observe acoustic waves launched within the Mo film and Newton's rings were used to measure separation at the Mo-glass interface. For removal of glass films on silicon substrates and thick Mo films on glass substrates, the fluences used are high enough to drive the liquid to vapor transformation at a free surface.

In summary, the effect of fs-laser vaporization on an interface has been studied, but no previous study has shown the effect of an interface on vapor formation. Also no previous experiment has permitted the measurement of two removed layers simultaneously, which allows a direct comparison of interface removal with the known mechanism of liquid spallation. In Chapter 4 of this dissertation, pump-probe microscopy of ultrathin films is used to determine the role of interfaces in the liquid to vapor phase transformation and clarify the mechanism of removal at an interface at fluences close to the liquid spallation threshold.

2.3 Nanocrystalline alloys

2.3.1 Stability of Nanocrystalline Metals by Alloying

Polycrystalline metals with nanoscale grain size exhibit unique characteristics such as enhanced mechanical properties including high hardness, wear resistance, ductility, and strength[56–59], increased corrosion resistance[60, 61], and unique magnetic properties[62]. However, nanoscale grains are thermally unstable and in pure metals grain growth occurs at a fraction of the melt temperature and at room temperature in some metals such as Cu, Pd,

Sn, Pb, Mg, and Al[58, 63–65]. This is particularly dramatic in the case of Pd which has a melting temperature of 1552 °C. In nanocrystalline Ni, grain growth has been observed near 100 °C[66].

Thermally stable nanocrystalline metals can be created through the addition of a solute species that preferentially occupies sites on grain boundaries. The solute atoms reduce the grain boundary free-energy effectively "pinning" the grain boundary and preventing grain growth[67]. This technique has been demonstrated in electrodeposited nanocrystalline Ni with W as the solute species. At equilibrium, W is soluble in fcc-Ni up to 12.4 at%, increased W composition will lead to the formation of the Ni_4W ordered compound. In electrodeposited nanocrystalline Ni, W can be added up to 30 at%[68–70], without forming ordered phases. For W compositions from 5 to 30 at%, nanocrystalline fcc-Ni with dissolved W are formed with W rich grain boundaries[70]. With increasing W concentration, the volume of W rich grain boundaries increases[71, 72] and consequently the average grain size decreases. Average grain sizes between 2-140 nm in diameter are produced for compositions ranging from 25 to 2 at% W respectively.

2.3.2 Formation of Nanocrystalline Metals via Laser Quenching

The layer of molten metal formed in a bulk material after irradiation with a short laser pulse is thin, either because the fluence was low and the melt depth was limited or a high laser fluence was used and most of the molten material was removed. The remaining molten layer is in contact with the bulk material which serves as an excellent thermal bath. In simulations of bulk Ni irradiated with picosecond pulses, thermal transport into the bulk quenches the melt layer at rates exceeding 10^{11} K/s[73]. Experimentally, the extreme quench rates after short pulse laser irradiation have been used to widen the range of compositions for glass formation in alloys compared to other methods having slower quench rates including splat quenching or melt spinning[74].

Simulations of pure Ni thin films irradiated with a femtosecond pulse were performed

to determine if laser quenching could produce a metallic glass, instead they predicted that the crystalline solid phase nucleates homogeneously in the deeply undercooled liquid and forms a nanocrystalline microstructure[30]. Simulations of bulk Ag irradiated just below the liquid spallation threshold also predicted the formation of a nanocrystalline surface layer[75], despite the formation of subsurface voids that would limit heat transport into the bulk. However, the nanocrystalline microstructure is not observed experimentally at the surface of pure metals after irradiation. Recent parallel experiments and simulation regarding the incubation of femtosecond laser damage in pure metals show that during solidification the melt resolidifies epitaxially from the bulk, however the extreme solidification rate leads to a large concentration of twin boundaries in the near surface[76, 77].

Chapter 5 of this thesis will explore grain boundary stabilization as a method to preserve the nanocrystalline microstructure after rapid heating and quenching via femtosecond laser irradiation.

2.4 Carbon Nanotubes

2.4.1 Methods for CNT Growth

A carbon nanotube is a sheet of graphene that forms a hollow cylinder. Graphene is a two dimensional hexagonal lattice of sp^2 bonded carbon. CNTs can be produced by many methods[78, 79], most notably arc discharge[80], laser vaporization with continuous or pulsed lasers[81–83], and CVD[84]. Typically in each of these processes CNTs formed by nucleation and growth from a metal catalyst nanoparticle. The nanoparticle serves as a catalyst for the absorption of carbon from the atmosphere, precipitates sp^2 carbon on the surface to form graphene structure of the CNT, and assists in the absorption and transport of carbon from the atmosphere for continued CNT growth[85]. During nucleation carbon is absorbed by the catalyst nanoparticle from the atmosphere and precipitates on the surface forming a roughly hemispherical graphene sheet, similar to a Fullerene. The Fullerene is approxi-

mately the diameter of the catalyst nanoparticle and will later be the closed end or "cap" of a CNT. More carbon is absorbed by the catalyst nanoparticle and transported to the edge of the cap causing the cap to lift off the surface of the nanoparticle. Between the catalyst and the cap, additional carbon organizes into a cylindrical graphene sheet causing the growth of a CNT. It is common for multiple nanotubes to grow in a nested configuration, called multiwalled carbon nanotubes. The walls of the tubes are coupled due to van der Waals bonding and generally treated as a single unit.

In Arc Discharge and Laser Vaporization synthesis a graphite target impregnated with the metal catalyst nanoparticles is either vaporized or ionized in an inert gas atmosphere. The metal catalyst precipitates forming catalyst nanoparticles that react with vaporized carbon, in the form of C1, C2, and C3 clusters to form CNTs[86, 87]. CVD growth of CNTs is performed by passing a carbon feedstock, typically a hydrocarbon or CO, over heated catalyst nanoparticles. Thermal decomposition of the feedstock liberates carbon to be absorbed by the catalyst and form a CNT. The two processes are similar in that they involve the formation of the CNT cap using a catalyst nanoparticle as a template, and that the nanoparticle acts as a medium for the absorption and transport of carbon to the growing CNT, they differ in how the catalyst nanoparticle and carbon feedstock are produced and the state of the carbon as it is absorbed.

It should be noted that aspects of this process are complex; the catalyst nanoparticle changes shape during nucleation[88], many types of catalyst can be used including dielectrics[85, 89–91], and it is even possible to form CNTs without a catalyst[92].

2.4.2 Activation and Termination of Catalytic Chemical Vapor Deposition

A common method to form catalyst nanoparticles for CVD growth is reduction and dewetting of a thin metal oxide film. The process of reducing the catalyst and producing nanoparticles is referred to as annealing. In this work iron oxide was used on an Al_2O_3 support.

As-deposited iron oxide thin films are reduced to iron by heating them in a hydrogen atmosphere. The high interfacial energy of metallic iron and the substrate drives a reduction in the surface area and the film dewets forming a distribution of metal nanoparticles on the support[85]. Recent work has shown that iron catalyst on an Al_2O_3 support only partially dewets during annealing and that the formation of nanoparticles is not complete until after the carbon carrying gas is introduced for CVD growth[93]. This is in agreement with the ubiquitous observation that CNT furnaces are more efficient if they have some adsorbed carbon on the internal surfaces[94].

After nucleation of a CNT on the catalyst nanoparticle, growth proceeds in a random direction. If the number of active catalyst nanoparticles per unit area on a surface is high, the randomly growing CNTs will impinge on one another preventing growth parallel to the substrate. This can prevent further growth of the nanotubes. If the area density is sufficiently high, above 1.7×10^9 cm^2[95], the CNTs will collectively orient perpendicular to the surface forming an aligned forest [96].

Recent work shows that growth of aligned forests terminates when the area density of active catalyst falls below a critical value and CNTs are too diffuse to support alignment [97]. The area density of catalyst falls due to Oswald ripening[98], mass transport into the substrate[98], or poisoning by the growth of an encompassing amorphous carbon layer[99]. Most research to increase the terminal length of CNT forests aims to extend the lifetime of the catalyst by optimizing static parameters such as: the atmosphere, pressure, and temperature; the composition, size, and distribution of catalyst; the support; or by introducing a plasma [78, 79].

2.4.3 Lasers in Chemical Vapor Deposition of CNTs

Apart from PLV synthesis of CNTs, continuous wave, nanosecond, and femtosecond lasers have been used to machine CNT forests, provide spatially resolved heat for CVD, and pre-irradiate catalyst to improve growth. Continuous wave[100–108] and pulsed lasers[109]

have been used as a means to heat catalyst, either directly or via absorption in a buried layer, for spatially resolved thermal CVD growth. Nanosecond laser pretreatment of metal catalyst layers, before annealing, was observed to dramatically increase the height of the aligned CNT forests[110]. It was found that the pretreatment caused CNTs in the treated area to have a smaller diameter and fewer walls and that the total catalytic activity in the treated area increased. It was proposed that the primary reason for the increased growth rate in the laser treated areas was that for the same mass of carbon, greater lengths of CNTs must be produced if the nanotubes are narrower and have fewer walls.

A different combination of the PLV and CVD methods has been investigated previously. Catalyst Co-Ni nanoparticles were produced by pulsed laser deposition using a nanosecond pulsed laser. The nanoparticles were heated to 700-1100 °C in an argon atmosphere atmosphere, similar to CVD. Instead of using a carbon carrying gas, for example acetylene, carbon for CVD growth was provided by pulsed laser ablation of a pure graphite target[111]. Normally during PLV synthesis of CNTs the catalyst nanoparticles condense in the presence of carbon. The previous study attempted to replicate PLV synthesis of CNTs in two discrete steps: the condensation of catalyst and later the absorption of carbon. Ultimately the process was more similar to CVD growth. Unlike in this dissertation, the catalyst was not irradiated with the laser during CVD growth.

2.4.4 Laser Breakdown of Carbon Nanotubes

Studies of femtosecond laser irradiation of graphite targets show that material removal occurs above a threshold of ~0.1 J/cm^2[112–115]. Two mechanisms have been proposed for damage at fluences near the threshold. First, electronic excitation causes vibrations in the graphene sheets and momentum is transferred into the direction normal to the graphene sheets breaking the weak van der Waals bonds between layers and ejecting intact graphene layers[115, 116]. Second, sp^2 bonds within graphene sheets are broken by nanoscopic coulomb explosion resulting in the emission of carbon ions and clusters[112, 114, 117].

After femtosecond laser ablation of graphite, light was emitted from the plume of ejected carbon by blackbody emission from large carbon clusters and characteristic emission from carbon atoms and small clusters[118].

Several studies have shown that absorption of laser radiation also break sp^2 bonds in fullerenes and CNTs. MD simulations show that bonds in the CNT cap are broken at lower fluences than the graphene in the CNT walls[119]. Simulations show that the threshold for fragmentation of Single Walled Nanotube (SWNT)s is 2.8 eV/atom[119–121] corresponding to a fluence of 0.48 J/cm^2[119].

Femtosecond laser machining of CNT forests has been studied[122] showing that CNTs can be removed cleanly without damaging the substrate allowing the machining of shapes with high aspect ratios. Femtosecond laser irradiation of CNT forests with 0.48 J/cm^2 at room temperature caused the surface of CNT forests to be destroyed; in the irradiated regions large iron nanoparticles precipitated and CNTs were highly defective. Other experiments show that isolated bundles of SWNT on glass substrates disintegrated after irradiation above ~0.05 J/cm^2[123]. Femtosecond laser irradiation of thick aligned forests with a single pulse produced by the laser used in this dissertation showed that the crust of the forest was destroyed above a threshold fluence of 0.1 J/cm^2[33].

Studies of irradiation with multiple nanosecond pulses show that with increasing pulse energy the sp^2 bonds of CNTs are broken generating a structure of amorphous carbon[124]. Irradiation with a series of higher energy nanosecond laser pulses was found to damage the surface layer of an aligned CNT forest. Light was also emitted from the ablation plume, similar to previously discussed femtosecond laser ablation of graphite, indicating the carbon nanotubes were broken down into some combination of clusters and ions[125]. Irradiation of aligned forests with nanosecond laser pulses produces shallow damage craters[126]. Nanosecond and CW lasers have also been used to machine structures in CNT forests [127] to produce tips for field emission of electrons.

In summary, lasers can be used in CNT production by creating free carbon, to create or

modify catalyst nanoparticles, and as a local heat source to drive CVD. In Chapter 7 of this dissertation femtosecond laser irradiation was used to augment CVD growth of CNTs. The processes of catalyst activation and poisoning and the mechanism for forest growth that were described in this section are used to understand how irradiation with a single pulse has a long term effect on the alignment and terminal length of CNTs grown using CVD.

References

1. Chen, J., Tzou, D. & Beraun, J. A semiclassical two-temperature model for ultrafast laser heating. *International Journal of Heat and Mass Transfer* **49,** 307–316 (Jan. 2006).
2. Gamaly, E. & Rode, A. Physics of ultra-short laser interaction with matter: From phonon excitation to ultimate transformations. *Progress in Quantum Electronics* **37,** 215–323 (Sept. 2013).
3. Qiu, T. Q. & Tien, C. L. Heat Transfer Mechanisms During Short-Pulse Laser Heating of Metals. *Journal of Heat Transfer* **115,** 835–841 (1993).
4. Amoruso, S., Nedyalkov, N., Wang, X., Ausanio, G., Bruzzese, R. & Atanasov, P. Ultrashort-pulse laser ablation of gold thin film targets: Theory and experiment. *Thin Solid Films* **550,** 190–198 (Jan. 2014).
5. Brorson, S. D., Fujimoto, J. G. & Ippen, E. P. Femtosecond electronic heat-transport dynamics in thin gold films. *Physical Review Letters* **59,** 1962–1965 (1987).
6. Hohlfeld, J., Müller, J. G., Wellershoff, S.-S. & Matthias, E. Time-resolved thermoreflectivity of thin gold films and its dependence on film thickness. *Applied Physics B* **64,** 387–390 (1997).
7. Wellershoff, S.-S., Hohlfeld, J., Güdde, J. & Matthias, E. The role of electron–phonon coupling in femtosecond laser damage of metals: *Applied Physics A* **69,** S99–S107 (S1 Dec. 1999).
8. Bonn, M., Denzler, D. N., Funk, S., Wolf, M., Wellershoff, S.-S. & Hohlfeld, J. Ultrafast electron dynamics at metal surfaces: Competition between electron-phonon coupling and hot-electron transport. *Physical Review B* **61,** 1101–1105 (2000).
9. Anisimov, S. I., Inogamov, N. A., Petrov, Y. V., Zhakhovskii, V. V. & Nishihara, K. in *Laser Ablation and its Applications* (ed Phipps, C.) *Springer Series in Optical Sciences* 129, 1–16 (Springer US, Jan. 1, 2007).
10. Chowdhury, I. H. & Xu, X. F. Heat transfer in femtosecond laser processing of metal. *Numerical Heat Transfer Part a-Applications* **44,** 219–232 (Aug. 15, 2003).
11. Anisimov, S. I., Kapeliovich, B. L. & Perelman, T. L. Electron Emission from Metal Surfaces Exposed to Ultra-Short Laser Pulses. *Sov. Phys.-JETP* **39,** 375–377 (Feb. 1, 1974).
12. Rethfeld, B., Sokolowski-Tinten, K., von der Linde, D. & Anisimov, S. Timescales in the response of materials to femtosecond laser excitation. *Applied Physics A* **79** (July 26, 2004).

13. Rethfeld, B., Sokolowski-Tinten, K., von der Linde, D. & Anisimov, S. Ultrafast thermal melting of laser-excited solids by homogeneous nucleation. *Physical Review B* **65** (Feb. 2002).

14. Ren, Y., Chen, J. & Zhang, Y. Modeling of ultrafast phase changes in metal films induced by an ultrashort laser pulse using a semi-classical two-temperature model. *International Journal of Heat and Mass Transfer* **55,** 1620–1627 (Feb. 2012).

15. Hopkins, P. E. & Norris, P. M. Substrate influence in electron–phonon coupling measurements in thin Au films. *Applied Surface Science* **253,** 6289–6294 (May 2007).

16. Colombier, J.-P., Combis, P., Stoian, R. & Audouard, E. High shock release in ultrafast laser irradiated metals: Scenario for material ejection. *Physical Review B* **75,** 104105 (2007).

17. Zhigilei, L. V., Ivanov, D. S., Leveugle, E., Sadigh, B. & Bringa, E. M. Computer modeling of laser melting and spallation of metal targets. *Proceedings of SPIE* (ed Phipps, C. R.) 505–519 (Sept. 20, 2004).

18. Von der Linde, D. & Sokolowski-Tinten, K. The physical mechanisms of short-pulse laser ablation. *Applied Surface Science* **154,** 1–10 (2000).

19. Reis, D. A., Gaffney, K. J., Gilmer, G. H. & Torralva, B. Ultrafast dynamics of laser-excited solids. *MRS bulletin* **31,** 601–606 (2006).

20. Upadhyay, A. K. & Urbassek, H. M. Response of ultrathin metal films to ultrafast laser irradiation: A comparative molecular-dynamics study. *Journal of Physics: Conference Series* **59,** 68–74 (Apr. 1, 2007).

21. Leveugle, E., Ivanov, D. S. & Zhigilei, L. V. Photomechanical spallation of molecular and metal targets: molecular dynamics study. *Applied Physics A* **79,** 1643–1655 (Nov. 2004).

22. Upadhyay, A. K. & Urbassek, H. M. Melting and fragmentation of ultra-thin metal films due to ultrafast laser irradiation: a molecular-dynamics study. *Journal of Physics D: Applied Physics* **38,** 2933–2941 (Aug. 21, 2005).

23. Povarnitsyn, M. E., Itina, T. E., Sentis, M., Khishchenko, K. V. & Levashov, P. R. Material decomposition mechanisms in femtosecond laser interactions with metals. *Physical Review B* **75,** 235414 (June 2007).

24. Lorazo, P., Lewis, L. & Meunier, M. Thermodynamic pathways to melting, ablation, and solidification in absorbing solids under pulsed laser irradiation. *Physical Review B* **73,** 134108 (Apr. 2006).

25. Vidal, F., Johnston, T. W., Laville, S., Barthélemy, O., Chaker, M., Le Drogoff, B., Margot, J. & Sabsabi, M. Critical-Point Phase Separation in Laser Ablation of Conductors. *Physical Review Letters* **86,** 2573–2576 (Mar. 19, 2001).

26. Cheng, C. R. & Xu, X. F. Mechanisms of decomposition of metal during femtosecond laser ablation. *Physical Review B* **72,** 165415 (Oct. 2005).

27. *Lasers in Materials Science* (eds Castillejo, M., Ossi, P. M. & Zhigilei, L.) (Springer International Publishing, Cham, 2014).

28. Perez, D. & Lewis, L. Thermodynamic evolution of materials during laser ablation under pico and femtosecond pulses. *Applied Physics A* **79** (July 26, 2004).

29. Murphy, R. D., Torralva, B. & Yalisove, S. M. The role of an interface on Ni film removal and surface roughness after irradiation by femtosecond laser pulses. *Applied Physics Letters* **102,** 181602 (2013).

30. Ivanov, D. S., Lin, Z., Rethfeld, B., O′Connor, G. M., Glynn, T. J. & Zhigilei, L. V. Nanocrystalline structure of nanobump generated by localized photoexcitation of metal film. *Journal of Applied Physics* **107,** 013519 (2010).

31. Ivanov, D. S. & Zhigilei, L. V. Combined atomistic-continuum modeling of short-pulse laser melting and disintegration of metal films. *Physical Review B* **68,** 064114 (Aug. 28, 2003).

32. Rouleau, C. M., Shih, C.-Y., Wu, C., Zhigilei, L. V., Puretzky, A. A. & Geohegan, D. B. Nanoparticle generation and transport resulting from femtosecond laser ablation of ultrathin metal films: Time-resolved measurements and molecular dynamics simulations. *Applied Physics Letters* **104,** 193106 (May 12, 2014).

33. Murphy, R. D. *Femtosecond Laser Interactions at Interfaces and Their Applications.* PhD thesis (University of Michigan, 2013).

34. Harris, L., Beasley, J. K. & Loeb, A. L. Reflection and transmission of radiation by metal films and the influence of nonabsorbing backings. *JOSA* **41,** 604–610 (1951).

35. Lai, H.-Y. & Huang, P.-H. Atomistic simulations of spallation dynamics in multilayer thin-film interface excited by femtosecond laser. *Computational Materials Science* **41,** 498–507 (Feb. 2008).

36. Golightly, J. S. & Castleman, A. W. Analysis of titanium nanoparticles created by laser irradiation under liquid environments. *Journal of Physical Chemistry B* **110,** 19979–19984 (Oct. 12, 2006).

37. Hopkins, P. E. & Norris, P. M. Contribution of Ballistic Electron Transport to Energy Transfer During Electron-Phonon Nonequilibrium in Thin Metal Films. *Journal of Heat Transfer* **131,** 043208 (2009).

38. Hoche, T., Ruthe, D. & Petsch, T. Low-fluence femtosecond-laser interaction with a Mo/Si multilayer stack. *Applied Physics A* **79** (Sept. 2004).

39. Picard, Y. N., Adams, D. P. & Yalisove, S. M. Femtosecond laser interactions with Co/Al multilayer films. *MRS Proceedings* **MM 1.9,** 1.9.1–1.9.7 (Jan. 2004).

40. Picard, Y. N., Adams, D. P., Palmer, J. A. & Yalisove, S. M. Pulsed laser ignition of reactive multilayer films. *Applied Physics Letters* **88,** 144102 (Apr. 3, 2006).

41. Thomas, D. A., Lin, Z., Zhigilei, L. V., Gurevich, E. L., Kittel, S. & Hergenröder, R. Atomistic modeling of femtosecond laser-induced melting and atomic mixing in Au film – Cu substrate system. *Applied Surface Science* **255,** 9605–9612 (Sept. 2009).

42. Gurevich, E. L., Kittel, S. & Hergenröder, R. Experimental and numerical study of surface alloying by femtosecond laser radiation. *Applied Surface Science* **258,** 2576–2579 (Jan. 15, 2012).

43. Shank, C., Yen, R. & Hirlimann, C. Time-Resolved Reflectivity Measurements of Femtosecond-Optical-Pulse-Induced Phase Transitions in Silicon. *Physical Review Letters* **50,** 454–457 (Feb. 1983).

44. Downer, M. C., Fork, R. L. & Shank, C. V. Femtosecond imaging of melting and evaporation at a photoexcited silicon surface. *JOSA B* **2,** 595–599 (1985).

45. Von der Linde, D., Sokolowski-Tinten, K. & Bialkowski, J. Laser–solid interaction in the femtosecond time regime. *Applied Surface Science* **109–110,** 1–10 (Feb. 1, 1997).

46. Sokolowski-Tinten, K., Bialkowski, J., Cavalleri, A., Von der Linde, D., Oparin, A., Meyer-ter-Vehn, J. & Anisimov, S. I. Transient states of matter during short pulse laser ablation. *Physical Review Letters* **81,** 224–227 (1998).

47. Bonse, J., Bachelier, G., Siegel, J. & Solis, J. Time- and space-resolved dynamics of melting, ablation, and solidification phenomena induced by femtosecond laser pulses in germanium. *Physical Review B* **74,** 134106 (Oct. 6, 2006).

48. Bonse, J., Bachelier, G., Siegel, J., Solis, J. & Sturm, H. Time- and space-resolved dynamics of ablation and optical breakdown induced by femtosecond laser pulses in indium phosphide. *Journal of Applied Physics* **103,** 054910 (Mar. 1, 2008).

49. Ionin, A. A., Kudryashov, S. I., Seleznev, L. V. & Sinitsyn, D. V. Dynamics of the spallative ablation of a GaAs surface irradiated by femtosecond laser pulses. *JETP Letters* **94,** 753–758 (Jan. 2012).

50. Newton, I. *Opticks, Or, A Treatise of the Reflections, Refractions, Inflections & Colours of Light* 546 pp. (Courier Corporation, 1979).

51. Agranat, M. B., Anisimov, S. I., Ashitkov, S. I., Zhakhovskii, V. V., Inogamov, N. A., Nishihara, K. & Petrov, Y. V. Nanospallation induced by a femtosecond laser pulse. *Proceedings of SPIE* (eds Exarhos, G. J., Guenther, A. H., Lewis, K. L., Ristau, D., Soileau, M. J. & Stolz, C. J.) 672002 (Oct. 10, 2007).

52. McDonald, J. P., Nees, J. A. & Yalisove, S. M. Pump-probe imaging of femtosecond pulsed laser ablation of silicon with thermally grown oxide films. *Journal of Applied Physics* **102,** 063109 (2007).

53. Rapp, S., Domke, M., Schmidt, M. & Huber, H. Physical Mechanisms during fs Laser Ablation of Thin SiO2 Films. *Physics Procedia* **41,** 734–740 (Jan. 2013).

54. Bartl, D., Michalowski, A., Hafner, M., Letsch, A., Nolte, S. & Tünnermann, A. Time-resolved study of back side ablated molybdenum thin films by ultrashort laser pulses. *Applied Physics A* **110,** 227–233 (Aug. 31, 2012).

55. Domke, M., Rapp, S., Schmidt, M. & Huber, H. P. Ultra-fast movies of thin-film laser ablation. *Applied Physics A* **109,** 409–420 (July 31, 2012).

56. Gleiter, H. Nanocrystalline materials. *Progress in Materials Science* **33,** 223–315 (Jan. 1, 1989).

57. Meyers, M. A., Mishra, A. & Benson, D. J. Mechanical properties of nanocrystalline materials. *Progress in Materials Science* **51,** 427–556 (May 2006).

58. Birringer, R. Nanocrystalline materials. *Materials Science and Engineering: A* **117,** 33–43 (Sept. 1, 1989).

59. Bringa, E. M., Caro, A., Wang, Y., Victoria, M., McNaney, J. M., Remington, B. A., Smith, R. F., Torralva, B. R. & Swygenhoven, H. V. Ultrahigh Strength in Nanocrystalline Materials Under Shock Loading. *Science* **309,** 1838–1841 (Sept. 16, 2005).

60. Andrievski, R. A. & Khatchoyan, A. V. in *Nanomaterials in Extreme Environments Springer Series in Materials Science* 230, 79–102 (Springer International Publishing, 2016).

61. Liu, L., Li, Y. & Wang, F. Electrochemical corrosion behavior of nanocrystalline materials—a review. *Journal of Materials Science & Technology* **26,** 1–14 (2010).

62. Herzer, G. Grain-Size Dependence of Coercivity and Permeability in Nanocrystalline Ferromagnets. *Ieee Transactions on Magnetics* **26,** 1397–1402 (Sept. 1990).

63. Gertsman, V. Y. & Birringer, R. On the room-temperature grain growth in nanocrystalline copper. *Scripta Metallurgica et Materialia* **30,** 577–581 (1994).

64. Gunther, B., Kumpmann, A. & Kunze, H.-D. Secondary recrystallization effects in nanostructured elemental metals. *Scripta Metallurgica et Materialia* **27,** 833–838 (1992).

65. Malow, T. & Koch, C. C. Thermal Stability of Nanocrystalline Materials. *Materials Science Forum* **225-227,** 595–604 (1996).

66. Natter, H., Schmelzer, M. & Hempelmann, R. Nanocrystalline nickel and nickel-copper alloys: Synthesis, characterization, and thermal stability. *Journal of Materials Research* **13,** 1186–1197 (May 1998).

67. Weissmüller, J. Alloy effects in nanostructures. *Nanostructured Materials. Proceedings of the First International Conference on Nanostructured Materials* **3,** 261–272 (Jan. 1, 1993).

68. Yamasaki, T., SchloBmacher, P., Ehrlich, K. & Ogino, Y. Formation of amorphous electrodeposited Ni-W alloys and their nanocrystallization. *Nanostructured Materials. Selected Papers from the NATO Advanced Study Institute (ASI) on Nanostructured Materials* **10,** 375–388 (Apr. 1998).

69. Schuh, C. A., Nieh, T. G. & Iwasaki, H. The effect of solid solution W additions on the mechanical properties of nanocrystalline Ni. *Acta Materialia* **51,** 431–443 (Jan. 22, 2003).

70. Chookajorn, T., Murdoch, H. A. & Schuh, C. A. Design of Stable Nanocrystalline Alloys. *Science* **337,** 951–954 (Aug. 24, 2012).

71. Detor, A. & Schuh, C. Tailoring and patterning the grain size of nanocrystalline alloys. *Acta Materialia* **55,** 371–379 (Jan. 2007).

72. Detor, A. J., Miller, M. K. & Schuh, C. A. Solute distribution in nanocrystalline Ni-W alloys examined through atom probe tomography. *Philosophical Magazine* **86,** 4459–4475 (Oct. 1, 2006).

73. Duff, W. H. & Zhigilei, L. V. Computational study of cooling rates and recrystallization kinetics in short pulse laser quenching of metal targets. *Journal of Physics: Conference Series* **59,** 413–417 (Apr. 1, 2007).

74. Lin, C. .-.-J. & Spaepen, F. Nickel-niobium alloys obtained by picosecond pulsed laser quenching. *Acta Metallurgica* **34,** 1367–1375 (July 1, 1986).

75. Wu, C., Christensen, M. S., Savolainen, J.-M., Balling, P. & Zhigilei, L. V. Generation of subsurface voids and a nanocrystalline surface layer in femtosecond laser irradiation of a single-crystal Ag target. *Physical Review B* **91** (Jan. 12, 2015).

76. Shugaev, M. V., Wu, C., Armbruster, O., Naghilou, A., Brouwer, N., Ivanov, D. S., Derrien, T. J.-Y., Bulgakova, N. M., Kautek, W., Rethfeld, B. & Zhigilei, L. V. Fundamentals of ultrafast laser–material interaction. *MRS Bulletin* **41,** 960–968 (Dec. 2016).

77. Sedao, X., Shugaev, M. V., Wu, C., Douillard, T., Esnouf, C., Maurice, C., Reynaud, S., Pigeon, F., Garrelie, F., Zhigilei, L. V. & Colombier, J.-P. Growth Twinning and Generation of High-Frequency Surface Nanostructures in Ultrafast Laser-Induced Transient Melting and Resolidification. *ACS Nano* **10,** 6995–7007 (July 26, 2016).

78. Szabó, A., Perri, C., Csató, A., Giordano, G., Vuono, D. & Nagy, J. B. Synthesis Methods of Carbon Nanotubes and Related Materials. *Materials* **3,** 3092–3140 (May 7, 2010).

79. Prasek, J., Drbohlavova, J., Chomoucka, J., Hubalek, J., Jasek, O., Adam, V. & Kizek, R. Methods for carbon nanotubes synthesis—review. *Journal of Materials Chemistry* **21,** 15872–15884 (2011).

80. Shi, Z., Lian, Y., Zhou, X., Gu, Z., Zhang, Y., Iijima, S., Zhou, L., Yue, K. T. & Zhang, S. Mass-production of single-wall carbon nanotubes by arc discharge method. *Carbon* **37,** 1449–1453 (1999).

81. Yudasaka, M., Komatsu, T., Ichihashi, T. & Iijima, S. Single-wall carbon nanotube formation by laser ablation using double-targets of carbon and metal. *Chemical Physics Letters* **278,** 102–106 (Oct. 24, 1997).

82. Thess, A., Lee, R., Nikolaev, P., Dai, H., Petit, P., Robert, J., Xu, C., Lee, Y. H., Kim, S. G., Rinzler, A. G., Colbert, D. T., Scuseria, G. E., Tománek, D., Fischer, J. E. & Smalley, R. E. Crystalline Ropes of Metallic Carbon Nanotubes. *Science* **273,** 483–487 (1996).

83. Eklund, P. C., Pradhan, B. K., Kim, U. J., Xiong, Q., Fischer, J. E., Friedman, A. D., Holloway, B. C., Jordan, K. & Smith, M. W. Large-Scale Production of Single-Walled Carbon Nanotubes Using Ultrafast Pulses from a Free Electron Laser. *Nano Letters* **2,** 561–566 (June 1, 2002).

84. Kumar, M. & Ando, Y. Chemical Vapor Deposition of Carbon Nanotubes: A Review on Growth Mechanism and Mass Production. *Journal of Nanoscience and Nanotechnology* **10,** 3739–3758 (June 1, 2010).

85. Dupuis, A.-C. The catalyst in the CCVD of carbon nanotubes—a review. *Progress in Materials Science* **50,** 929–961 (Nov. 2005).

86. Puretzky, A. A., Schittenhelm, H., Fan, X., Lance, M. J., Allard, L. F. & Geohegan, D. B. Investigations of single-wall carbon nanotube growth by time-restricted laser vaporization. *Physical Review B* **65** (June 24, 2002).

87. Guo, T., Nikolaev, P., Thess, A., Colbert, D. T. & Smalley, R. E. Catalytic growth of single-walled manotubes by laser vaporization. *Chemical Physics Letters* **243,** 49–54 (Sept. 8, 1995).

88. Hofmann, S., Sharma, R., Ducati, C., Du, G., Mattevi, C., Cepek, C., Cantoro, M., Pisana, S., Parvez, A., Cervantes-Sodi, F., Ferrari, A. C., Dunin-Borkowski, R., Lizzit, S., Petaccia, L., Goldoni, A. & Robertson, J. In situ Observations of Catalyst Dynamics during Surface-Bound Carbon Nanotube Nucleation. *Nano Letters* **7,** 602–608 (Mar. 2007).

89. Chen, Y. & Zhang, J. Diameter controlled growth of single-walled carbon nanotubes from SiO2 nanoparticles. *Carbon* **49,** 3316–3324 (Aug. 2011).

90. Huang, S., Cai, Q., Chen, J., Qian, Y. & Zhang, L. Metal-Catalyst-Free Growth of Single-Walled Carbon Nanotubes on Substrates. *Journal of the American Chemical Society* **131,** 2094–2095 (Feb. 18, 2009).

91. Takagi, D., Hibino, H., Suzuki, S., Kobayashi, Y. & Homma, Y. Carbon Nanotube Growth from Semiconductor Nanoparticles. *Nano Letters* **7,** 2272–2275 (Aug. 2007).

92. Liu, H., Takagi, D., Chiashi, S. & Homma, Y. The growth of single-walled carbon nanotubes on a silica substrate without using a metal catalyst. *Carbon* **48,** 114–122 (Jan. 2010).

93. Bedewy, M., Viswanath, B., Meshot, E. R., Zakharov, D. N., Stach, E. A. & Hart, A. J. Measurement of the Dewetting, Nucleation, and Deactivation Kinetics of Carbon Nanotube Population Growth by Environmental Transmission Electron Microscopy. *Chemistry of Materials* **28,** 3804–3813 (June 14, 2016).

94. Liu, K., Liu, P., Jiang, K. & Fan, S. Effect of carbon deposits on the reactor wall during the growth of multi-walled carbon nanotube arrays. *Carbon* **45,** 2379–2387 (Oct. 2007).

95. Bedewy, M., Meshot, E. R., Guo, H., Verploegen, E. A., Lu, W. & Hart, A. J. Collective Mechanism for the Evolution and Self-Termination of Vertically Aligned Carbon Nanotube Growth. *Journal of Physical Chemistry C* **113,** 20576–20582 (Dec. 3, 2009).

96. Bennett, R. D., Hart, A. J. & Cohen, R. E. Controlling the Morphology of Carbon Nanotube Films by Varying the Areal Density of Catalyst Nanoclusters Using Block-Copolymer Micellar Thin Films. *Advanced Materials* **18,** 2274–2279 (Sept. 5, 2006).

97. Bedewy, M., Meshot, E. R., Reinker, M. J. & Hart, A. J. Population Growth Dynamics of Carbon Nanotubes. *ACS Nano* **5,** 8974–8989 (Nov. 22, 2011).

98. Kim, S., Pint, C., Amama, P., Zakharov, D., Hauge, R., Maruyama, B. & Stach, E. Evolution in catalyst morphology leads to carbon nanotube growth termination. *The Journal of Physical Chemistry Letters* **1,** 918–922 (2010).

99. Stadermann, M., Sherlock, S. P., In, J.-B., Fornasiero, F., Park, H. G., Artyukhin, A. B., Wang, Y., De Yoreo, J. J., Grigoropoulos, C. P., Bakajin, O., Chernov, A. A. & Noy, A. Mechanism and Kinetics of Growth Termination in Controlled Chemical Vapor Deposition Growth of Multiwall Carbon Nanotube Arrays. *Nano Letters* **9,** 738–744 (Feb. 11, 2009).

100. Park, J. B., Jeong, S. H., Jeong, M. S., Lim, S. C., Lee, I. H. & Lee, Y. H. The rapid growth of vertically aligned carbon nanotubes using laser heating. *Nanotechnology* **20,** 185604 (May 6, 2009).

101. Park, J. B., Jeong, S. H. & Jeong, M. S. Position-controlled synthesis of single-walled carbon nanotubes on a transparent substrate by laser-induced chemical vapor deposition. *Applied Surface Science* **257,** 641–649 (Nov. 2010).

102. Haluska, M., Bellouard, Y. & Dietzel, A. Time dependent growth of vertically aligned carbon nanotube forest using a laser activated catalytical CVD method RID B-6920-2008. *Physica Status Solidi B-Basic Solid State Physics* **245,** 1927–1930 (Oct. 2008).

103. Chiashi, S., Kohno, M., Takata, Y. & Maruyama, S. in *Cola'05: 8th International Conference on Laser Ablation* (eds Hess, W., Herman, P., Bauerle, D. & Koinuma, H.) 155–158 (IoP Publishing Ltd, Bristol, 2007).

104. Shi, J., Lu, Y. F., Yi, K. J., Lin, Y. S., Liou, S. H., Hou, J. B. & Wang, X. W. Direct synthesis of single-walled carbon nanotubes bridging metal electrodes by laser-assisted chemical vapor deposition. *Applied Physics Letters* **89** (Aug. 21, 2006).

105. Asai, Y., Fujiwara, Y., Ohno, Y., Maehashi, K., Inoue, K. & Matsumoto, K. in *Proceedings of the International Conference on Nanoscience and Technology* (eds Meyer, E., Hegner, M., Gerber, C. & Guntherodt, H.) 46–50 (Iop Publishing Ltd, Bristol, 2007).

106. Michaelis, F. B., Weatherup, R. S., Bayer, B. C., Bock, M. C. D., Sugime, H., Caneva, S., Robertson, J., Baumberg, J. J. & Hofmann, S. Co-catalytic Absorption Layers for Controlled Laser-Induced Chemical Vapor Deposition of Carbon Nanotubes. *ACS Applied Materials & Interfaces* **6,** 4025–4032 (Mar. 26, 2014).

107. Fujiwara, Y., Maehashi, K., Ohno, Y., Inoue, K. & Matsumoto, K. Position-Controlled Growth of Single-Walled Carbon Nanotubes by Laser-Irradiated Chemical Vapor Deposition. *Japanese Journal of Applied Physics* **44,** 1581–1584 (Apr. 8, 2005).

108. Bock, M. C. D., Denk, R., Wirth, C. T., Goldberg-Oppenheimer, P., Hofmann, S. & Baumberg, J. J. Optical feedback mechanisms in laser induced growth of carbon nanotube forests. *Applied Physics Letters* **100** (Jan. 2, 2012).

109. Liu, Z., Styers-Barnett, D. J., Puretzky, A. A., Rouleau, C. M., Yuan, D., Ivanov, I. N., Xiao, K., Liu, J. & Geohegan, D. B. Pulsed laser CVD investigations of single-wall carbon nanotube growth dynamics. *Applied Physics A* **93,** 987–993 (Dec. 2008).

110. Rouleau, C. M., Eres, G., Cui, H., Christen, H. M., Puretzky, A. A. & Geohegan, D. B. Altering the catalytic activity of thin metal catalyst films for controlled growth of chemical vapor deposited vertically aligned carbon nanotube arrays. *Applied Physics A* **93,** 1005–1009 (July 3, 2008).

111. Aïssa, B., Therriault, D. & El Khakani, M. On-substrate growth of single-walled carbon nanotube networks by an \all-laser" processing route. *Carbon* **49,** 2795–2808 (July 2011).

112. Kaplan, A., Lenner, M., Huchon, C. & Palmer, R. E. Nonlinearity and time-resolved studies of ion emission in ultrafast laser ablation of graphite. *Applied Physics A* **92,** 999–1004 (Sept. 2008).

113. Reitze, D. H., Ahn, H. & Downer, M. C. Optical properties of liquid carbon measured by femtosecond spectroscopy. *Physical Review B* **45,** 2677–2693 (1992).

114. Lenner, M., Kaplan, A., Huchon, C. & Palmer, R. Ultrafast laser ablation of graphite. *Physical Review B* **79,** 184105 (May 2009).

115. Reininghaus, M., Wortmann, D., Finger, J., Faley, O., Poprawe, R. & Stampfer, C. Laser induced non-thermal deposition of ultrathin graphite. *Applied Physics Letters* **100,** 151606 (2012).

116. Miyamoto, Y., Zhang, H. & Tomanek, D. Photoexfoliation of Graphene from Graphite An Ab Initio Study. *Physical Review Letters* **104** (May 2010).

117. Jeschke, H., Garcia, M. & Bennemann, K. Theory for the Ultrafast Ablation of Graphite Films. *Physical Review Letters* **87,** 015003 (June 2001).

118. Amoruso, S., Ausanio, G., Vitiello, M. & Wang, X. Infrared femtosecond laser ablation of graphite in high vacuum probed by optical emission spectroscopy. *Applied Physics A* **81,** 981–986 (Oct. 2005).

119. Dumitrică, T., Garcia, M. E., Jeschke, H. O. & Yakobson, B. I. Breathing coherent phonons and caps fragmentation in carbon nanotubes following ultrafast laser pulses. *Physical Review B* **74,** 193406 (Nov. 10, 2006).

120. Jeschke, H. O., Romero, A. H., Garcia, M. E. & Rubio, A. Microscopic investigation of laser-induced structural changes in single-wall carbon nanotubes. *Physical Review B* **75,** 125412 (Mar. 12, 2007).

121. Romero, A., Jeschke, H., Rubio, A. & Garcia, M. Atomistic simulation of the laser induced damage in single wall carbon nanotubes: Diameter and chirality dependence. *Applied Physics A* **79,** 899–901 (Sept. 2004).

122. Hong, N. T., Baek, I. H., Rotermund, F., Koh, K. H. & Lee, S. Femtosecond laser machining: A new technique to fabricate carbon nanotube based emitters. *Journal of Vacuum Science & Technology B: Microelectronics and Nanometer Structures* **28,** C2B38 (2010).

123. Guo, S. X. & Ben-Yakar, A. Femtosecond laser nanoablation of glass in the near-field of single wall carbon nanotube bundles. *Journal of Physics D: Applied Physics* **41,** 185306 (2008).

124. Kichambare, P., Chen, L., Wang, C., Ma, K., Wu, C. & Chen, K. Laser irradiation of carbon nanotubes. *Materials Chemistry and Physics* **72,** 218–222 (Nov. 1, 2001).

125. Puretzky, A. A., Eres, G., Rouleau, C. M., Ivanov, I. N. & Geohegan, D. B. Real-time imaging of vertically aligned carbon nanotube array growth kinetics. *Nanotechnology* **19,** 055605 (Feb. 6, 2008).

126. Cheong, F. C., Lim, K. Y., Sow, C. H., Lin, J. & Ong, C. K. Large area patterned arrays of aligned carbon nanotubes via laser trimming. *Nanotechnology* **14,** 433–437 (2003).

127. Elmer, J., Yaglioglu, O., Schaeffer, R., Kardos, G. & Derkach, O. Direct patterning of vertically aligned carbon nanotube arrays to 20 um pitch using focused laser beam micromachining. *Carbon* **50,** 4114–4122 (Sept. 2012).

CHAPTER 3

Experimental Details

3.1 Irradiation of Materials

Experiments were performed using a Clark MXR CPA 2001 that produced 1 mJ laser pulses at a pulse repetition rate of 1 kHz. Pulses had a 780 nm center wavelength with a bandwidth of 10 nm, linear polarization, and a Gaussian spatial profile. The $1/e^2$ diameter of the unfocused beam was 7mm. The maximum variation in the energy of laser pulses was 2% of the average energy. Before each experiment, a rudimentary auto correlation was used to minimize the pulse length and to verify that the pulses were near 150 fs in duration. All experiments were performed at the laser focus, using a single pulse. All experiments in this work were performed by irradiating pristine material; no experiment in this work was performed with multiple pulses. The sample is maneuvered in the beam path using three Newport ILS100CC servo linear stage with a single step accuracy of 1 μm and an XPS C-8 stage controller.

For most experiments a single plano-convex lens with a 20 cm focal length was used to focus the laser beam. The sample was placed at the focus by irradiating pristine material at various positions along the beam direction without varying the pulse energy. As the sample approaches the focal point of the laser, the diameter of the ablation crater increases. At focus, the diameter of the crater reaches a maximum. The damage craters were measured in-situ using a tabletop Infinitube microscope with a Mitutoyo SLWD 50X objective that

was oriented parallel to the beam path. Once the sample is at the focus the beam power is reduced using Neutral Density (ND) filters and a $1/2$ waveplate/polarizer pair until ablation craters are formed for only 50% of pulses. The 2% noise in the pulse intensity causes half of the pulses to rise above the threshold fluence for damage and half to fall below, but the average peak fluence is centered at the threshold for damage. To determine the fluence the pulse energy and beam radius must be measured. The pulse energy is determined by dividing the power of the beam at threshold, P_{th}, by the repetition rate of the laser, v. The beam power is measured using an Ophir Electronics thermopile detector. The beam radius was measured using a WinCamD-12 beam profiling camera by Dataray Incorporated. The factory calibrated scale of the profiling camera, 0.14 μm/pixel, was verified by translating the camera using a Newport ILS100CC servo linear stage with a single step accuracy of 1 μm, then measuring the displacement of the beam in pixels. The area of the beam with an intensity greater than 1/e^2 of the maximum was measured, and the effective 1/e^2 beam radius, w_0, was calculated. The threshold fluence for damage is determined using Equation 3.1. In Equation 3.1 w_0 is the 1/e^2 radius, v is the pulse repetition rate of the laser, and P_{th} is the threshold power for damage.

$$F_{th} = \frac{2P_{th}}{vw_0} \tag{3.1}$$

The liquid spallation threshold of silicon was used as the standard measurement for alignment and as the "canary in the coal mine," a qualitative indicator that laser conditions were acceptable and consistent day to day. Significant variations in the pulse duration, contrast between the seeded femtosecond pulse and the Amplified Spontaneous Emission, or large pre-pulses and post-pulses would change the measured threshold fluence and the morphology of the ablation crater.

The threshold fluence for liquid spallation of silicon has been widely measured and is generally consistent across many groups[1–4]. A Si threshold between 0.29 and 0.34 J/cm^2

was deemed acceptable for experiments in this dissertation. The variation is believed to be the result of small variations in the contrast of the femtosecond pulse and the Amplified Spontaneous Emission (ASE) since every other variable could be directly measured.

3.1.1 Finding Threshold From Damage Radius vs. Fluence

In some experiments, it was impossible to directly measure the beam profile. In those cases, the threshold of silicon was measured before moving into the experimental setup, to verify the consistent Si threshold. In the experimental setup, the beam radius and Si threshold were measured in-situ. The sample was irradiated with multiple pulse energies and the area of the ablation spots was measured for each pulse energy. The beam profile and threshold were determined by fitting the measured damage area vs. the laser energy using the method of Liu et. al.[5]. An example of this method is shown in Figure 3.1. A silicon sample was irradiated with a range of peak fluences. The area of 10 damage spots were measured for each peak fluence. The data in Figure 3.1 show the average effective radius and error bars show the standard deviation for each peak fluence. The laser irradiated spots were more than 5 beam radii apart so the target area was not modified by a previous pulse.

3.2 Sample Preparation

Glass substrates for thin metal films were prepared by the procedure in table 3.1 adapted from the University of California-Irvine Integrated Nanosystems Research Facility[6].

3.2.1 Depositing Thin Metal Films

Thin films of pure Ni or multilayer films of Ni and W were sputter deposited using a Denton Vacuum DC Magnetron sputter head operated at a constant power of 200 W and Argon working pressure of 2 mTorr. The sputtering targets were 4 inches in diameter and

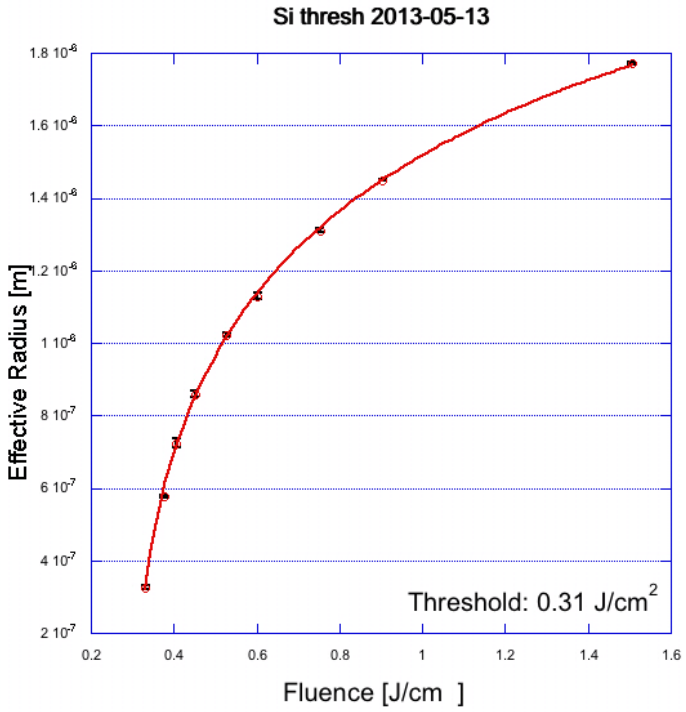

Figure 3.1: Method of finding threshold by fitting damage radius vs single pulse energy. An example using a two parameter fit of damage radius vs fluence to determine the damage threshold fluence of Si is shown.

Table 3.1: Procedure to clean glass substrates before deposition of thin metal films

STEP	DESCRIPTION	TIME (MINUTES)
1	Scrub with 10% Triton (aq)	NA
2	rinse with DI H_2O	NA
3	Soak in Acetone, 60 °C	10
4	Sonicate in Acetone	8
5	Sonicate in Methanol	8
6	Sonicate in Ethanol	8
7	Soak in 4M HCl (aq)	30
8	Rinse with DI H_2O	NA

substrates were less than 1 inch in diameter. The samples were placed on a platen rotating at 160 rpm so that they passed directly under the sputter target during each rotation. The sputter rates of Ni and W were 1.66 and 1.41 Å/s respectively. The deposition rates of each material were calibrated with Rutherford Backscattering Spectrometry using a 2 MeV helium ion beam in the Michigan Ion Beam Laboratory operated by Fabian Naab.

Multilayer films of Ni and Ag were deposited in the Lurie Nanofabrication Facility using a Kurt J. Lesker Lab18 sputter system operated at a constant power of 50 W and Argon working pressure of 2.4 mTorr. The sputter rates of Ni and Ag were 1.4 and 4 Å/s respectively. The deposition rates were calibrated using a Woollam M-2000 Ellipsometer to measure the thickness of metal thin films deposited with a target thickness of 20 nm on a Si wafer with 300 nm thermal oxide.

3.3 Chemical Vapor Deposition of Carbon Nanotubes

3.3.1 Preparing Catalyst for Chemical Vapor Deposition of Carbon Nanotubes

In this work, a well known and highly active catalyst system, Iron on an alumina substrate, is used[7–9]. Catalyst films of 2/10 nm of Fe/Al_2O_3 were deposited using Kurt J. Lesker Lab 18 RF sputtering tool. At a constant power of 200 W and Argon working pressure of 2.4 mTorr, the sputter rate of Al_2O_3 was 0.04 Å/s. Using a constant power of 50 W and Argon working pressure of 2.4 mTorr, the sputter rate of Fe was 0.3 Å/s. The substrate was a 500 μm thick Si wafer with 300 nm of thermal oxide.

3.3.2 Modified Sabre Furnace

A modified Absolute Nano Sabre cold-walled, atmospheric pressure CVD reactor was used to grow and irradiate CNTs. The smooth reactor tube was replaced with a cross that had

added quartz viewports above and below the catalyst as shown in Figure 3.2.

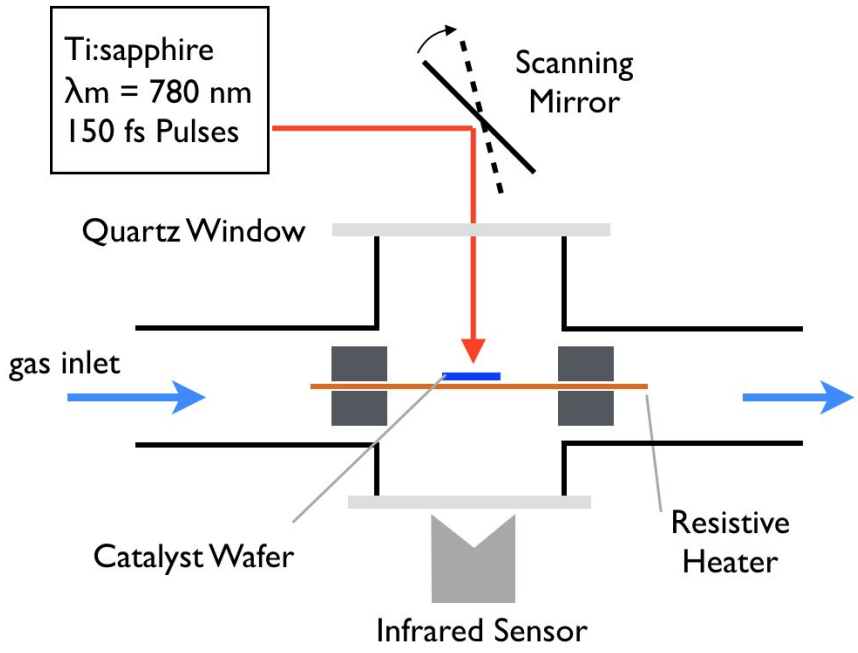

Figure 3.2: Diagram of setup for laser irradiation of CNT catalyst during growth. The laser is directed to the catalyst through a quartz window in the cross-shaped CVD reactor. The reactor is mounted on a translation stage so the location of the laser beam can be controlled in one direction. The location of the beam is controlled in a second direction, orthogonal to the direction of the motor, using a galvanometer mirror.

The catalyst was supported by a silicon wafer 500 μm thick, 1 cm wide, and 5 cm long suspended between tungsten clamps. The Si wafer was resistively heated using a power supply that requires a thermocouple input. During operation the temperature was instead monitored using an infrared detector through the bottom viewport. The infrared detector output voltage vs. temperature was calibrated using a thermocouple gauge then passed into a Labview program. The Labview script determines the output voltage expected by the power supply which is generated by an National Instruments 6211 DAQ. Gas flow rates were controlled using either a manual rotometer from MKS instruments or using computer controlled mass flow controllers from Brooks Instruments. Images were captured during growth using an Imitech 1200FT CCD attached to a telephoto lens. A single Labview

program was used to handle the infrared detector output and power supply input voltages , gas flow rates, and capture in-situ images of the catalyst at set times relative to the start of CNT growth defined by the introduction of acetylene.

3.3.3 Chemical Vapor Deposition recipe

The efficiency of CNT growth varied between batches of catalyst, when gas bottles were replaced, or if the system was not used for a long period of time. To minimize variation between CVD growth runs, catalyst was produced in large batches, and a 10 Standard Cubic Centimeter per Minute (sccm) flow of helium was maintained in the system while not in use. Bleeding helium into the reactor prevents adsorption of water by the chamber walls or silicon heater and assembly; water vapor has a significant impact on CNT growth and would cause variation. Because the furnace had to be opened between each growth run to exchange the catalyst, the furnace was purged with 200 sccm He for 20 minutes when resealed. During the annealing and growth steps, 10 sccm of Helium was passed through a gas washing beaker to add a controlled amount of water vapor to the reactor that was higher than the contamination from opening the chamber.

In this work CVD growth was performed with separate annealing and growth steps with the general parameters shown in Figure 3.3. The Fe/Al_2O_3 catalyst was annealed at 750 °C for 10 min with flow rates of 200 sccm helium and 200 sccm hydrogen. The annealing gases were added 5 minutes before the catalyst was heated. The Fe catalyst oxidizes when removed from vacuum after sputter deposition. Annealing reduces the Fe-oxide and causes the film to partially dewet, forming nanoparticles that serve as the catalyst for CVD growth of CNTs. After annealing the flow rate of helium was reduced to 190 sccm and 10 sccm acetylene was added to initiate CNT growth. The temperature is maintained at 750 °C for the growth step. The Root Mean Square (RMS) deviation in the setpoint temperature was 0.7 °C. In these experiments CNT growth was observed only at temperatures above 700 °C. The most efficient temperature for CNT growth was determined to be 750 °C by

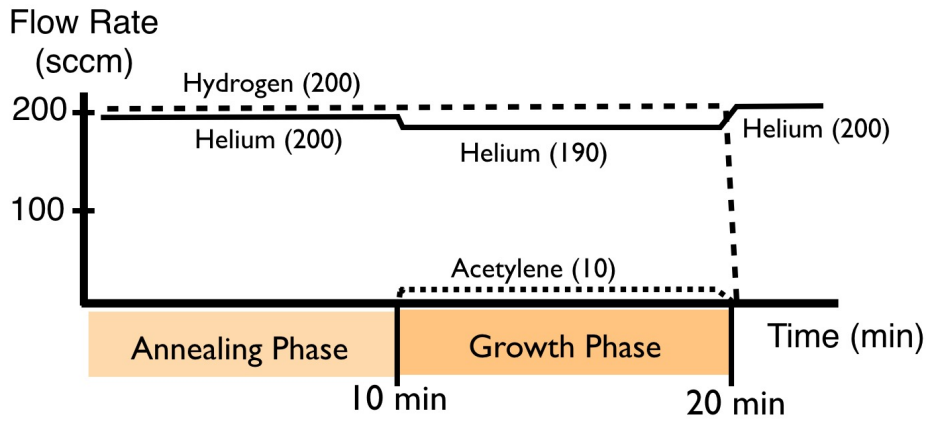

Figure 3.3: Parameters for CVD growth of CNTs. Before CVD the Sabre furnace is purged with helium for 20 minutes at room temperature. Catalyst was annealed at 750 °C for 10 min with helium and hydrogen. To initiate CNT growth acetylene is added and the helium flow rate is reduced to maintain a uniform overall flow rate. After a 10 minute growth stage the catalyst heater is turned off, acetylene and hydrogen flow is stopped, and the chamber is purged with helium.

a parametric study where CVD growth was performed using growth temperatures between 600 and 800 °C in 50 °C increments. Femtosecond laser enhanced CVD growth, discussed in Chapter 7, also yielded the tallest aligned forests of CNTs using a growth temperature of 750 °C.

At the end of the growth step the catalyst heater is turned off, acetylene and hydrogen flow is stopped, and the chamber is purged with helium to stop growth. The temperatures for growth were are relatively low in the range for growth of multiwalled tubes[10]. The annealing step is also relatively long, producing catalyst with large diameter that will typically result in growth of multiwalled nanotubes.

3.3.4 Irradiation of Catalyst During CVD Growth

For in-situ irradiation of catalyst during growth, the laser was directed through the top viewport and was incident on the catalyst surface, as shown in Figure 3.2. The laser was focused using a lens with a 40 cm focal length placed upstream of the Galvonometer. The

laser was focused onto the catalyst surface by the same procedure as in Section 3.1, but instead of changing the sample position through the laser focus, the lens was mounted on a manual micrometer stage and translated relative to the catalyst.

The position of the laser spot on the catalyst wafer was controlled in two dimensions by mounting the whole furnace on a mechanical stage to control the position in the x direction, and using a galvanometer mirror to position the laser in the y direction.

After growth an array of irradiated spots was observed on the sample in the form of stalks or areas with dense CNTs. In order to know the delay for irradiation of a given sample area, fiducial marks were made where the laser would land at the start of the growth step and at the end of growth. During the experiment, the laser spot was moved at a constant speed between the fiducial marks while pulses were delivered at a constant repetition rate, making it possible to accurately determine the time for irradiation by measuring the distance between the fiducial mark and the area of interest.

3.3.5 In-situ Microscopy of CNT Growth

A video camera equipped with a telephoto lens was used to record the the catalyst surface at a 80 degree angle of incidence during growth. The Sony ICX274AL CCD used is sensitive to wavelengths between 350 nm to 800 nm, the peak of the quantum efficiency curve is at a wavelength of 500 nm. It has been shown that emission in this wavelength range increases with CNT coverage during CVD growth [11].

3.4 Experimental Setup for Pump-Probe Optical Microscopy

For pump-probe microscopy, single pulses were split using a pellicle beam splitter into a pump and probe pulse. The pump pulse was focused onto the film at normal incidence with a $1/e^2$ area of 10500 ± 400 μm^2, measured with a DataRay WinCamD-14 beam profiling camera. The probe pulse was delayed 0-12 ns using a mechanical stage, frequency doubled

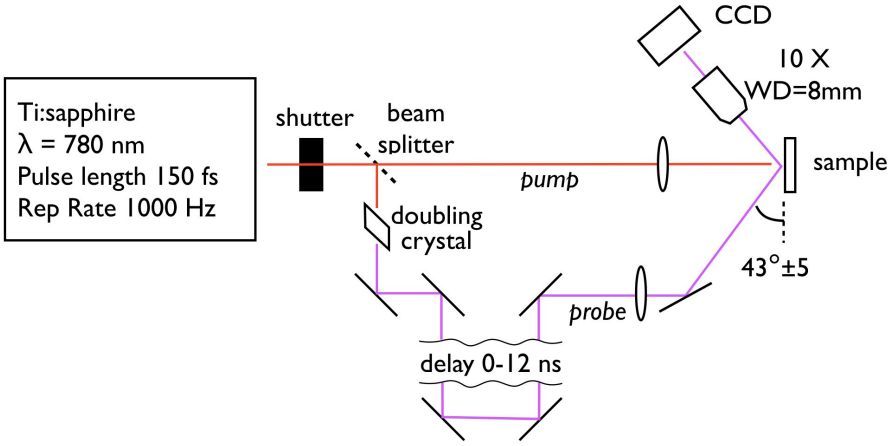

Figure 3.4: Experimental setup for the observation of Newton's rings in reflection geometry. For pump-probe measurement of Newton's rings images were captured in a reflection geometry. Single pulses were split into a pump and probe pulse. The pump pulse was focused onto the film at normal incidence. The probe pulse was delayed 0-12 ns using a mechanical stage, frequency doubled to 390 nm, focused on the sample at a 45 $\pm$ 2° angle of incidence with p polarization, and collected with a tabletop microscope.

to 390 nm, focused on the sample at a 45 $\pm$ 2° angle of incidence with p polarization, and collected with a tabletop microscope. An aperture 1 mm in diameter was placed in the probe line to reduce the beam waist before the lens that focuses the probe on the sample. Adding the aperture increases the diameter of the probe pulse at focus to evenly illuminate the sample over an area much larger than the pump spot. The setup is shown in Figure 3.4.

The x and y scale bars of the image were calibrated by taking an image of a copper Transmission Electron Microscopy (TEM) grid with square holes that were 62 μm from center to center. Zero probe delay was determined within 5 ps by observing the rapid increase in reflectivity in a Si sample due to the onset of carrier excitation and melting[12–14]. A single labview program was used to move the sample to a pristine area, set the probe delay, trigger the pump and probe pulses, and capture the images. Since the labview program automatically moves to pristine locations on the sample surface, the sample could not be manually repositioned to the common focus of the pump beam, probe beam, and microscope objective after each irradiation. To ensure the sample remains at the focus, it

was essential that the plane of the sample surface was exactly parallel to the translation axes of the stage. A goniometer was mounted between the sample and the stage and the sample was aligned using a micrometer, placed to measure the position of the surface perpendicular to the two scan directions. The goniometer was adjusted until the reading of the micrometer gauge did not change as the sample was translated.

References

1. Bonse, J., Baudach, S., Kruger, J., Kautek, W. & Lenzner, M. Femtosecond laser ablation of silicon-modification thresholds and morphology. *Applied Physics A* **74,** 19–25 (Jan. 2002).
2. Von der Linde, D., Sokolowski-Tinten, K. & Bialkowski, J. Laser–solid interaction in the femtosecond time regime. *Applied Surface Science* **109–110,** 1–10 (Feb. 1, 1997).
3. Bonse, J., Brzezinka, K. W. & Meixner, A. J. Modifying single-crystalline silicon by femtosecond laser pulses: an analysis by micro Raman spectroscopy, scanning laser microscopy and atomic force microscopy. *Applied Surface Science* **221,** 215–230 (Jan. 15, 2004).
4. Borowiec, A., MacKenzie, M., Weatherly, G. & Haugen, H. Transmission and scanning electron microscopy studies of single femtosecond- laser-pulse ablation of silicon. *Applied Physics A* **76,** 201–207 (Feb. 1, 2003).
5. Liu, J. M. Simple technique for measurements of pulsed Gaussian-beam spot sizes. *Optics Letters* **7,** 196–198 (May 1, 1982).
6. *Cleaning procedures for glass substrates* Standard Operating Procedure (University of California, Irvine, Integrated Systems Research Facility, May 2017).
7. Ansaldo, A., Haluska, M., Cech, J., Meyer, J. C., Ricci, D., Gatti, F., Di Zitti, E., Cincotti, S. & Roth, S. A study of the effect of different catalysts for the efficient CVD growth of carbon nanotubes on silicon substrates RID A-2506-2009. *Physica E-Low-Dimensional Systems & Nanostructures* **37,** 6–10 (Mar. 2007).
8. Moisala, A., Nasibulin, A. G. & Kauppinen, E. I. The role of metal nanoparticles in the catalytic production of single-walled carbon nanotubes—a review. *Journal of Physics: condensed matter* **15,** S3011–S3035 (2003).
9. Nagaraju, N., Fonseca, A., Konya, Z. & Nagy, J. B. Alumina and silica supported metal catalysts for the production of carbon nanotubes. *Journal of Molecular Catalysis a-Chemical* **181,** 57–62 (Mar. 25, 2002).
10. Cui, H., Eres, G., Howe, J., Puretkzy, A., Varela, M., Geohegan, D. & Lowndes, D. Growth behavior of carbon nanotubes on multilayered metal catalyst film in chemical vapor deposition. *Chemical Physics Letters* **374,** 222–228 (June 11, 2003).
11. Haluska, M., Bellouard, Y., van de Burgt, Y. & Dietzel, A. In situ monitoring of single-wall carbon nanotube laser assisted growth RID B-6920-2008. *Nanotechnology* **21** (Feb. 19, 2010).

12. Shank, C., Yen, R. & Hirlimann, C. Time-Resolved Reflectivity Measurements of Femtosecond-Optical-Pulse-Induced Phase Transitions in Silicon. *Physical Review Letters* **50,** 454–457 (Feb. 1983).

13. Downer, M. C., Fork, R. L. & Shank, C. V. Femtosecond imaging of melting and evaporation at a photoexcited silicon surface. *JOSA B* **2,** 595–599 (1985).

14. Sokolowski-Tinten, K., Bialkowski, J. & von der Linde, D. Ultrafast laser-induced order-disorder transitions in semiconductors. *Physical Review B* **51,** 14186–14198 (May 1995).

CHAPTER 4

Separation of Interfaces Via Laser Driven Extreme States

Published: Schrider, K. J., Torralva, B. & Yalisove, S. M. The dynamics of femtosecond pulsed laser removal of 20 nm Ni films from an interface. Applied Physics Letters 107, 124101 (Sept. 21, 2015).

Previous experiments by this research group indicated that removal of ultrathin Ni films on glass substrates occurs by two distinct mechanisms called intrafilm and interface removal[1, 2]. Intrafilm removal, where less than half the thickness of the Ni film is removed, was shown to occur by liquid spallation, similar to ablation of bulk metals and semiconductors. It was shown that ablation at an interface occurs due to heterogeneous nucleation of vapor. However the precise mechanism for interface removal was not well understood; it was believed that interface removal occurred where the melt front propagated to the interface, and so would occur as the film thickness was reduced or the local fluence was increased. Further consideration showed that ultrathin Ni films are heated uniformly, and at the melt threshold, the interface will melt without causing removal. This chapter studies the removal dynamics of 20 nm, ultrathin Ni films on glass substrates using pump-probe microscopy to clarify the mechanism for interface removal. Experimental results in this chapter show that removal occurs earlier after irradiation and the ejected layer accelerates more rapidly than was predicted by recent molecular dynamics models[3]. It is shown that the formation of vapor at the interface depends on the extreme non-equilibrium states that

are encountered as the film relaxes after heating with an ultrashort pulse.

The two removal mechanisms observed for 20 nm Ni films on glass substrates are also observed in ultrathin Ni-based two-component films studied in later chapters. The fluence threshold for interface removal and the dynamics of material relaxation involving the vapor dome are used as a reference to explore the effect of femtosecond laser irradiation on two-component ultrathin films.

4.1 Femtosecond Laser Removal of 20 nm Ni films on Glass Substrates

In previous studies by this group the threshold for damage and the depth of the removal crater were measured for bulk Ni, and for films ranging from 140 nm thick to 2 nm thick[1, 2]. The threshold for liquid spallation in bulk Ni is 0.32 J/cm^2. For Ni films 70 to 20 nm thick, the threshold fluence for liquid spallation and depth of removal fell smoothly with decreasing film thickness. For Ni films 70 to 20 nm thick, removal also occurred at the Ni-substrate interface. The threshold for removal at the Ni-substrate interface is higher than the liquid spallation threshold. Only interface removal was observed for Ni films less than 20 nm thick. The roughness in the interface and intrafilm removal regions was measured using Atomic Force Microscopy (AFM)[1]. The RMS roughness was 3.06 nm after interface removal, and 1.27 nm after intrafilm removal. The smooth intrafilm removal region is consistent with homogeneous nucleation of voids during liquid spallation. If the bonding at the Ni-glass interface was weak and interface removal occurred by liquid spallation, the roughness in the interface and intrafilm removal regions should be the same. It was also observed in previous work that interface removal could occur in the intrafilm removal region forming "pinholes" 1-3 μm wide that penetrated to the Ni glass interface. The location of pinholes was apparently random. It is not reasonable that the tensile strength of the liquid layer or the intensity of the tensile wave varied locally leading to the pinholes.

The pinholes were attributed to heterogeneous nucleation at sites on the Ni glass interface. The observations of random round pinholes, reminiscent of vapor nucleation by surface defects, and of high surface roughness at the exposed Ni-glass interface, inconsistent with homogenous nucleation of voids as in liquid spallation, indicated that interface removal occurs by heterogeneous nucleation of vapor[1, 2].

In this work, the state and temperature of the Ni film was estimated using a simplified thermodynamic model. The absorbance of the 20 nm Ni film was calculated using solutions for the Frensel equation for the case of an absorbing film on a non-absorbing substrate[4]. It was assumed that the absorbed energy was evenly distributed through the Ni film because the 20 nm thick Ni film is thinner than the mean free path of ballistic and hot electrons after irradiation[5–7]. The energy density per mol was compared with the NIST-JANAF thermochemical tables[8]. According to the data, the Ni film would begin to vaporize at 30% of the interface removal threshold and completely vaporize at 110%. Ni vapor would be most stable along the Ni-glass interface; in that position, the vapor bubbles would break the Ni-glass interface and the Ni vapor pressure would exert a force propelling the interface removal layer away from the substrate. The dynamics of interface removal via vapor formation are examined in the next section. It should be noted that the NIST-JANAF data was calculated for quasi-static heating at ambient pressure, and does not exactly reflect the temperature or transformations after femtosecond laser irradiation. First, the metal initially heats at constant volume: for most solids the heat capacity at constant volume is slightly lower at elevated temperatures. Second, the work of expansion will reduce the peak temperature of the film. Later, hydrodynamic simulations [9] and previous MD simulations [3] are considered; the simulations more accurately show the response of ultrathin metal films after irradiation.

4.2 Pump-Probe Microscopy of 20 nm Ni Films

For 20 nm Ni films, the threshold fluences for interface and intrafilm removal are 0.16 and 0.36 J/cm^2 respectively. Figure 4.1 shows a post-mortem AFM image of a 20 nm thick Ni film irradiated with 0.4 J/cm^2. Because the pulse has a Gaussian intensity profile, a two-stepped crater is formed as shown in Figure 4.1. Interface removal occurs within the central region, above the interface removal threshold, and intrafilm removal occurs in the surrounding region, below the interface removal threshold.

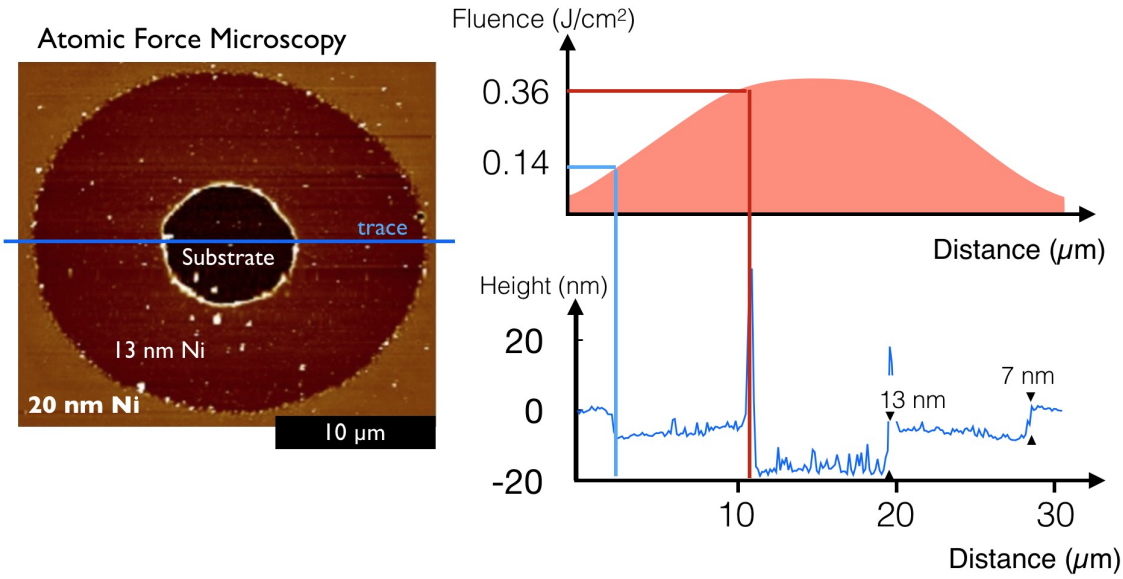

Figure 4.1: Femtosecond laser removal crater of 20 nm Ni films on glass. Removal of ultrathin Ni films occurs by two mechanisms, intrafilm and interface removal. Intrafilm removal occurs via liquid spallation removing less than half of the film above a threshold fluence of 0.16 J/cm^2. Interface removal occurs above a threshold fluence of 0.36 J/cm^2. Irradiation with a gaussian laser pulse creates a two-stepped removal crater. AFM shows the extent and depth of removal in each region.

Pump-probe microscopy was selected to study removal of 20 nm Ni films because it is possible to observe the configuration of the Ni film during removal, measure the speed of the removed layers, and determine the time that they separate from the substrate.

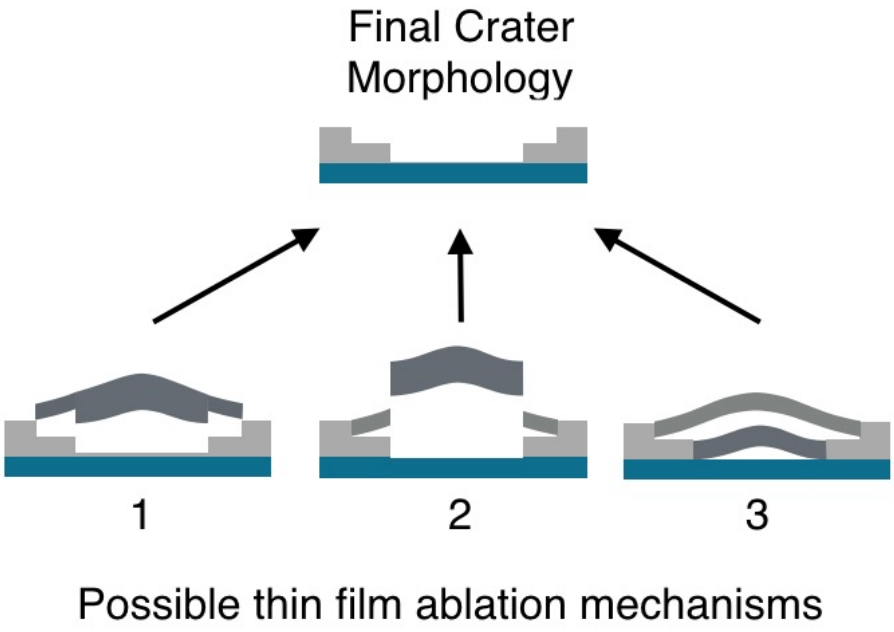

Figure 4.2: Possible configurations for removal of 20 nm Ni thin films after irradiation. Several configurations of the Ni during removal would consistent with the two stepped crater formed after irradiation above the interface removal threshold. Each configuration would indicate different mechanisms for removal in the interface region.

The configuration of the Ni film refers to the number and thickness of layers removed at a given fluence. We speculated that several possible configurations of the removed material were consistent with the stepped crater morphology, shown in Figure 4.2. Material could be ejected as a single liquid layer with the same profile as the crater, as a central disk and surrounding ring, or in two continuous layers. Each configuration had implications about the mechanisms for removal. For example, configuration 1, where removal in each region separates at the same time and travels at the same speed, could indicate interface removal occurs by liquid spallation at the weak Ni-glass interface. The sequences of pump-probe images in Figures 4.3, 4.4, and 4.5 show that removal occurs with configuration 3 from Figure 4.2 indicating the top and bottom layers are removed by different mechanism.

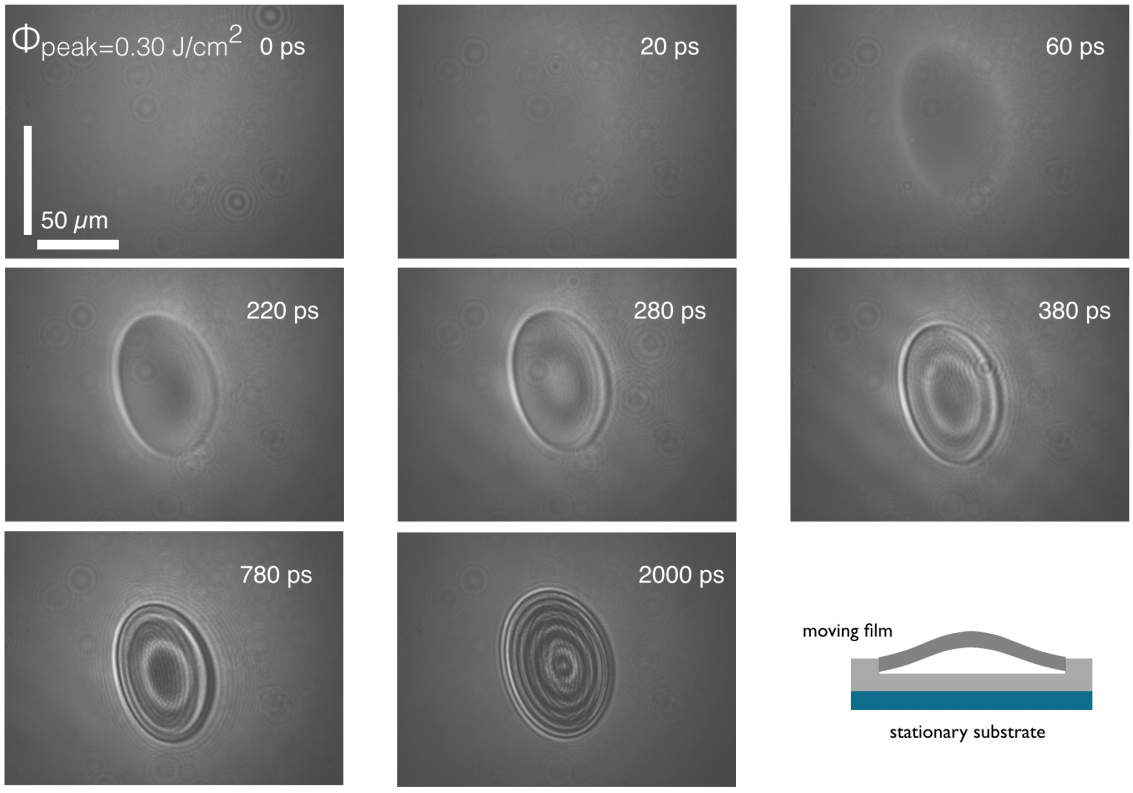

Figure 4.3: Pump-Probe images of 20 nm Ni films on glass after irradiation from the free surface with a peak fluence below the threshold for interface removal. A single Newton's rings pattern is observed within the intrafilm removal region indicating a single moving layer.

Figure 4.3 shows a sequence of pump-probe images captured at different delays for a 20 nm Ni film irradiated with a peak fluence of 0.3 J/cm^2. In this case, below the threshold for interface removal, only intrafilm removal is observed post-mortem, resulting in a uniform crater 7 nm deep. In Figure 4.3, a single family of Newton's rings is observed to develop inside the intrafilm region. Each dark or bright ring represents a interference extrema that occurs when the removed film reaches a fixed displacement away from the stationary substrate. The Newton's rings originate at the middle of the removal crater, corresponding to the peak fluence, and develop outward because the speed of the removed film is proportional to the local fluence. After irradiation with a Gaussian pulse the center of the film is moving the fastest. The speed elsewhere drops as a Gaussian function of distance to the center so that at any given time the moving layer is in the shape of a dome. The center of the dome reaches the fixed displacement for an interference extrema first. Then the slower moving areas just outside the peak of the dome reach the interference extrema, and so on such that the contrast moves outward in all directions forming the Newton's ring, as in Figure 4.3. A schematic cross section diagram of the Ni film during removal is shown in the lower-right of Figure 4.3. The origin of the fine fringes around the circumference of the Newton's rings pattern is not known, but they could be caused by Fresnel diffraction from the edge of the removal crater.

Figure 4.4 shows a sequence of pump-probe images after irradiation at 0.6 J/cm^2, above the interface removal threshold so a two-stepped crater is observed post-mortem similar to Figure 4.1. From 0 to 2000 ps after irradiation, a family of Newton's rings is observed to develop inside the intrafilm region. Between 2000 and 3000 ps the first family of Newton's rings distorts–initially narrowing along the minor axis of the Newton's rings pattern, as seen in Figure 4.4 2100 ps after irradiation, forming an "hourglass" shape. Eventually the distortion of the Newton's rings pattern leads to the formation of a diamond-shaped set of fringes, as seen in Figure 4.4 3500 ps after irradiation. The distortion of the first family of Newton's rings resembles an extreme comatic aberration of a beam through a lens: coma

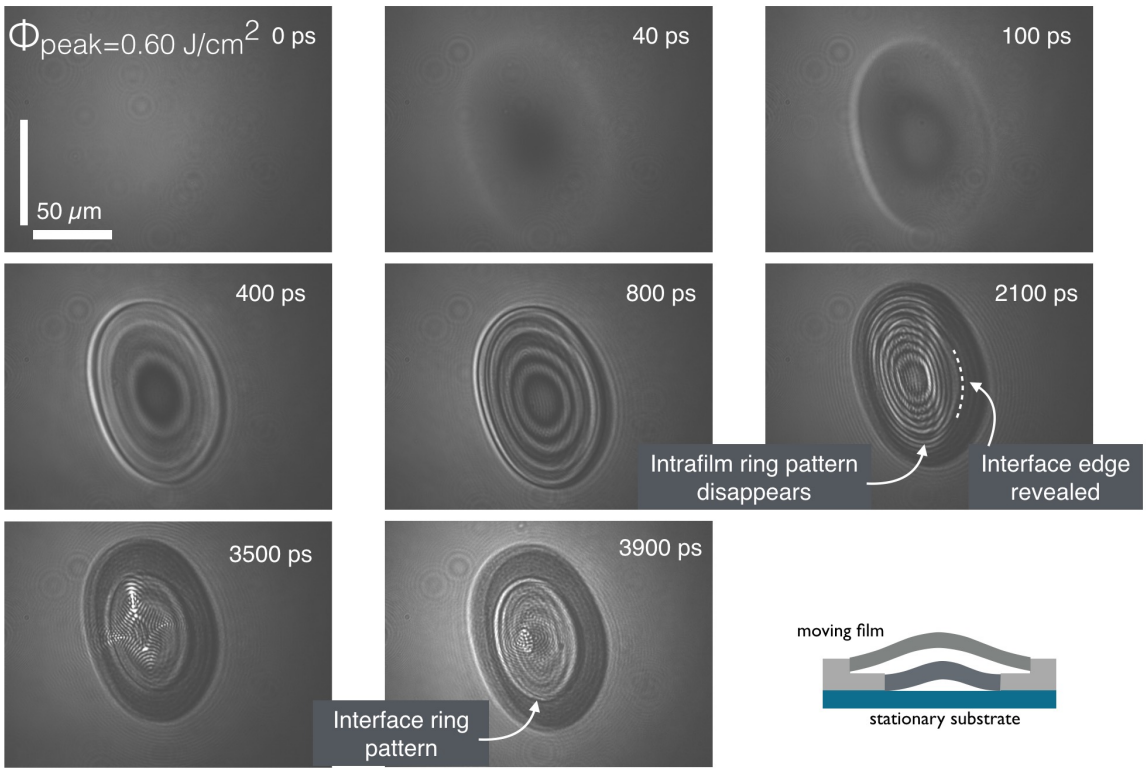

Figure 4.4: Pump-Probe images of 20 nm Ni films on glass after irradiation from the free surface with a peak fluence above the threshold for interface removal. Two Newton's rings patterns are observed within the intrafilm and interface removal regions respectively indicating two separate moving layers. The interface removal pattern is revealed after 2000 ps.

occurs when a beam passes through a lens at an angle. In this case, the dome formed by the moving film acts as a lens. With increasing delay the film travels and the curvature of the dome increases and so does its focussing power; eventually the comatic aberration is so significant that the image of intrafilm removal rings is eliminated.

After the intrafilm removal rings disappear, a second family of Newton's rings is observed in the interface removal region. The existence of two families of Newton's rings, corresponding to the intrafilm and interface removal regions respectively, indicates that above the interface removal threshold the film is removed in two distinct layers. The intrafilm layer is 7 nm thick and is removed as a disk corresponding to the area of the intrafilm removal region; the interface layer is 13 nm thick and is removed as a disk from the interface removal region. A schematic cross section diagram of the Ni film configuration during removal is shown in the lower-right of Figure 4.4.

The technique of pump-probe microscopy is typically performed using a microscope at normal incidence to the sample surface; the probe pulse replaces the lamp for illumination and the pump pulse is introduced at an angle[10–20]. This is simply because when a microscope views a surface at an angle only a narrow band of the image is at focus. When 20 nm Ni ablation was viewed at normal incidence, the Newton's rings from intrafilm removal region never disappeared. Using the pump probe setup in Figure 3.4, it is possible to observe Newton's rings from multiple ejected layers provided they have different velocities. Comatic aberration eliminates interference contrast caused by the faster moving layer as the curvature of the ejected layer increases. This is the only pump probe method where Newton's rings from multiple ejected layers can be observed separately and is a single pump probe experiment.

As the probe delay increases, Newton's rings progress outward and eventually pass out of the removal region; this occurs because the velocity at the removal threshold is not zero. In Figure 4.4 it is impossible to know how many interface removal rings have progressed out of the interface removal region before the pattern is revealed 3500 ps after irradiation.

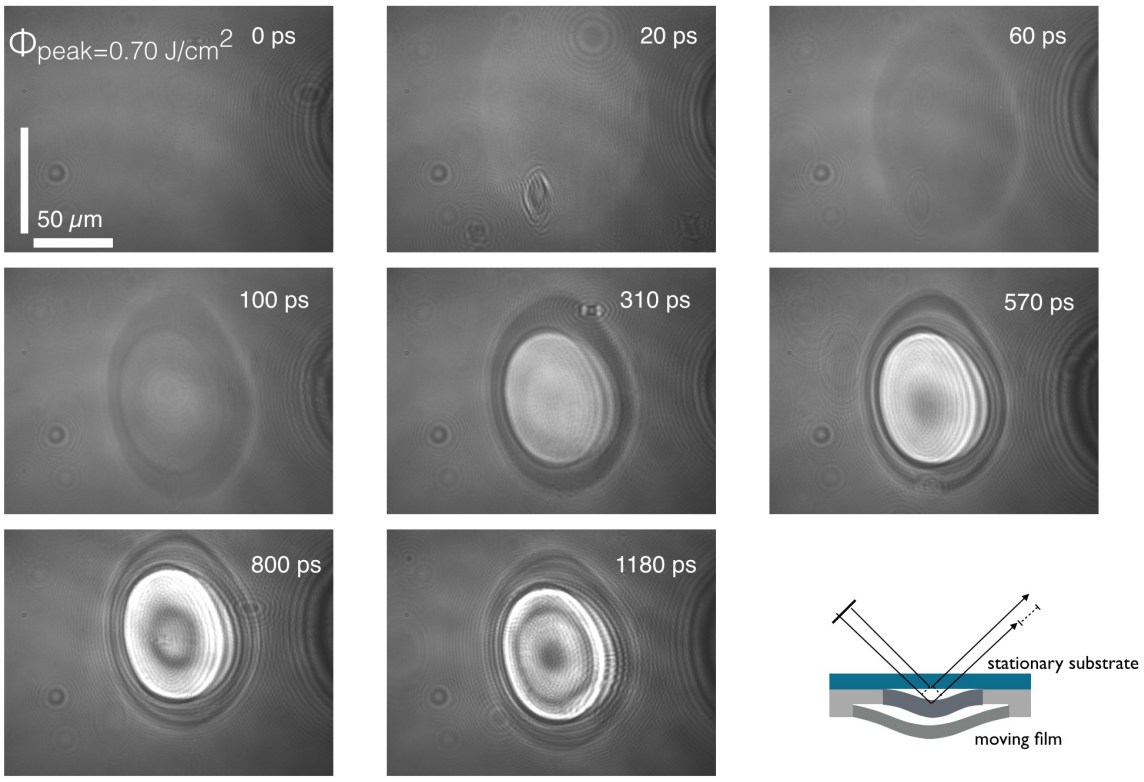

Figure 4.5: Pump-Probe images of 20 nm Ni films on glass after irradiation through the glass substrate with a peak fluence above the threshold for interface removal. Images were collected through the glass substrate. The interface removal Newton's rings pattern is viewed directly and is not obscured by reflections from the intrafilm removal layer.

It is therefore impossible to know the interference order of the extrema or determine the displacement of the film. To measure the Newton's rings formed by the interface removal layer without looking through the intrafilm removal layer, the sample was flipped over and the Ni-substrate interface was viewed through the glass as shown in the schematic cross section view shown in the lower-right of Figure 4.5.

Figure 4.5 shows a sequence of pump-probe images after irradiation at 0.7 J/cm^2 where the sample was irradiated and viewed through the glass substrate. While the intrafilm removal region can be seen clearly after 60 ps, no Newton's rings are observed. Only the Newton's rings in the interface removal region are observed, and they form well before 3500 ps.

The back-side intrafilm and interface removal thresholds are 0.11 $\pm$ 0.02 J/cm^2 and 0.20 $\pm$ 0.02 J/cm^2 respectively. The decreased thresholds are consistent with an increase in the optical absorbance of the Ni film to 0.52 for irradiation through the glass, compared with 0.35 for irradiation from the Ni free surface. The absorbance was calculated using a model for absorbing films on nonabsorbing substrates[4], and the optical constants of Ni[21] and glass[22].

4.3 Interpreting Newton's Rings

In previous studies, displacement vs. time of the moving layers was measured by visually determining when each Newton's ring appeared at the center of the pump spot[18, 20, 23] or by measuring the number of rings in each image. These methods are adequate to interpret the extent and the velocity of a single moving layer, but will lead to a significant error in the measured displacement.

1. The visual reversal in the bright/dark contrast at the center is well before the true minimum or maximum interference occurs, the displacement will be overestimated by $\sim 1/4\lambda$.

2. Image artifacts in the removal crater at early time can resemble a Newton's ring and lead to a systematic error of order in the measured interference extrema.

3. Counting the Newton's rings in the pattern will underestimate the interference order at the center at long delays after Newton's rings have progressed out of the removal area.

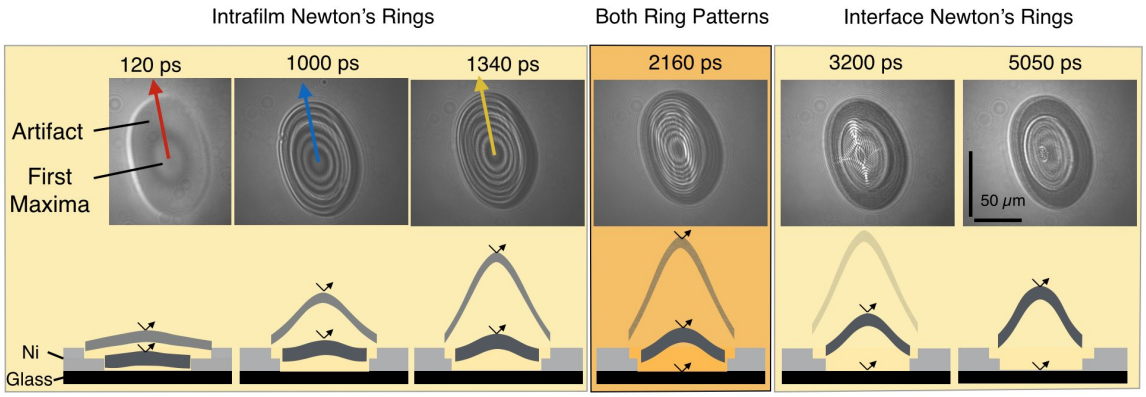

Figure 4.6: Pump-probe images showing the appearance of separate Newton's ring patterns distinct to interface and intrafilm removal. Using a front-side probe and a peak pump fluence of 0.60 J/cm^2, two Newton's ring patterns indicate removal in two distinct layers. Note, intrafilm removal occurs at a lower fluence and thus a wider area than interface removal. Schematics of the moving layers are shown at each delay (not to scale). The reflections forming Newtons rings are indicated by angled arrows. At 120 ps delay two rings are marked, one ring will be identified as an imaging artifact.

For this work, where the dynamics of two moving layers must be distinguished and the displacement must be measured accurately, images were created that track the radial expansion of the Newtons rings with increasing delay. Radial intensity profiles were measured along the long axis of the Newtons rings pattern, as shown with the arrows in Figure 4.6. The width of the line profile was 3 μm. The corresponding intensity profiles are shown in Figure 4.7a. The radial intensity profiles measured at each delay were arranged with respect to time, forming the plot in Figure 4.7b. The location of the profiles from Figure 4.6 are shown with analogous arrows. In Figure 4.7b, the y axis corresponds to radial position in the pump spot, the x axis corresponds to time, and the reflected intensity is represented

in greyscale at each coordinate. This image is referred to here as a composite plot of the Newton's rings.

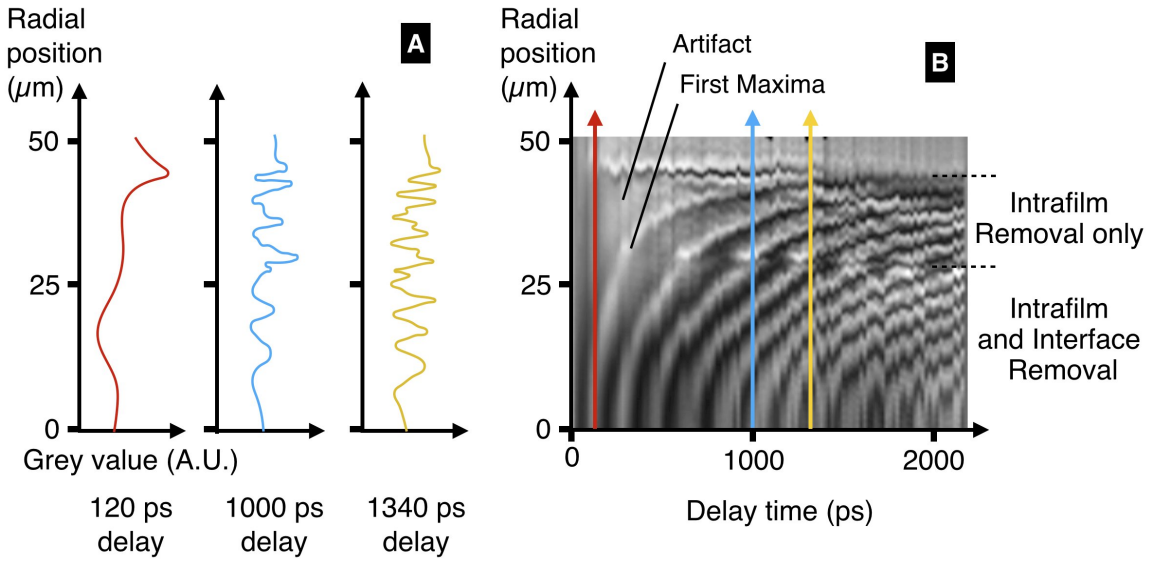

Figure 4.7: Plot showing evolution of Newton's rings in pump-probe microscopy on Ni films a) Newton's rings profiles were taken from each pump-probe image along arrows in Figure 4.6. The scale is the same for all 3 profile plots. b) Profiles were arranged according to their delay time forming a new composite plot. Newtons rings appear at the peak fluence and expand radially. This plot shows the artifact at 120 ps in Figure 4.6 does not evolve over time and is not a Newtons ring. The expansion of Newtons rings with time is discontinuous at the interface crater edge. The interface layer is ejected with a minimum velocity at the crater edge and is stationary below the removal threshold. The rings in the interface removal region show the relative velocity of the intrafilm and interface layers.

The radial progression of the Newton's rings in the composite plot follow a characteristic curve because the velocity falls with increasing radial position according to the Gaussian distribution of local fluence. In Figure 4.7b a discontinuity in the curves of the Newton's rings is visible at the edge of the interface removal region, indicating a discontinuity in the velocity. It appears that the velocity of the intrafilm removal layer is slightly faster just outside the interface removal region. Consider the schematic images of the Ni film for each time in Figure 4.6. The displacement and velocity of the intrafilm removal layer is continuous at the interface removal threshold, but the interface layer goes from moving with some minimum speed to not moving and fixed on the substrate. There, the relative displacement

of the Ni layers suddenly increases causing the discontinuity in the radial expansion of Newton's rings seen in Figure 4.7b. For a peak fluence above the removal threshold, as in Figure 4.7b, the displacement measured at the center of the pump spot is the intrafilm layer displacement minus the interface layer displacement.

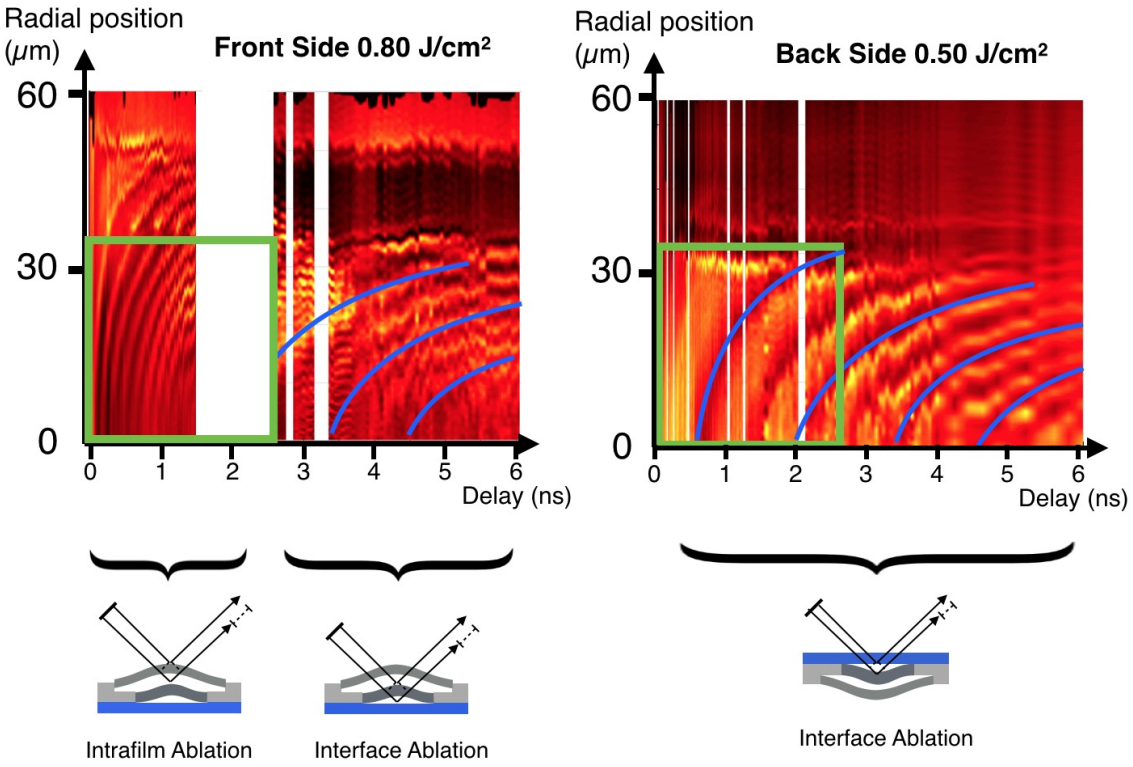

Figure 4.8: Plots comparing the evolution of Newton's rings viewed from the free surface and through the glass substrate. The composite plots for pump-probe of the Ni free surface and through the glass substrate are shown for the same absorbed fluence. Backside pump-probe includes the interface removal Newton's ring pattern at early time. For probe delays longer than 2500 ps the progression of Newton's rings from interface removal are identical.

Figure 4.8 shows the composite plot created for front side and back side pump probe after irradiation with a peak absorbed fluence of 0.28 J/cm^2, corresponding to peak pulse fluences of 0.8 and 0.5 J/cm^2 for front side and back side respectively. Because of the different absorbance for irradiation from each side, the absorbed fluence is the same. Comparison of the two images shows that the radial progression of interface Newton's rings is the same from 2700 to 6000 ps after irradiation. The maxima are marked in the front-side

plot and the minima are marked in the back-side plot. The sign of interference extrema at the same displacement of the film are opposite because in the case of interface removal viewed from the back-side, there is a 180 phase change on reflection at the interface of the glass and the gap because the light is reflecting at the surface where the index of refraction drops. In all other cases, reflection occurs at an interface where the index of refraction rises. As a result, the first interference extrema of the interface removal layer is constructive viewed from the front side and destructive viewed from the backside.

4.4 Measuring Displacement Using Newton's Rings

Displacement vs. time of moving layers was measured by the appearance of extrema at the center of the pump spot, fundamentally similar to previous studies using ring counting, but visual bias was eliminated by using temporal profiles of reflected intensity and referencing the composite plot to determine the interference order.

Temporal profiles of reflected intensity were measured directly from the composite plot by taking a line profile corresponding to the box in Figure 4.9a. The measured intensity in the temporal profile corresponds to a 3x4 μm rectangle at the center of the pump spot. The intensity at the center was normalized to the probe intensity by placing a second monitor region 150 microns away from the pump spot. The normalized data were smoothed with a 3rd order Savitzky-Golay filter spanning nominally one half of the period between extrema, the period is the time from maxima to maxima or vice versa. Finally the smoothed data were fit with a variable knot 10th order spline. The spline fit consists of a piecewise 10th order polynomial function. Knots in the piecewise function connect polynomial segments. The spline was produced with the Matlab® Curve Fitting Toolbox which determines the coefficients of the polynomials and distributes the knots along the polynomial to achieve the best fit. Figure 4.9b shows the raw reflected intensity data, (x), the smoothed data, (o), and the spline fit. The delay for extrema were measured from the maxima and minima in

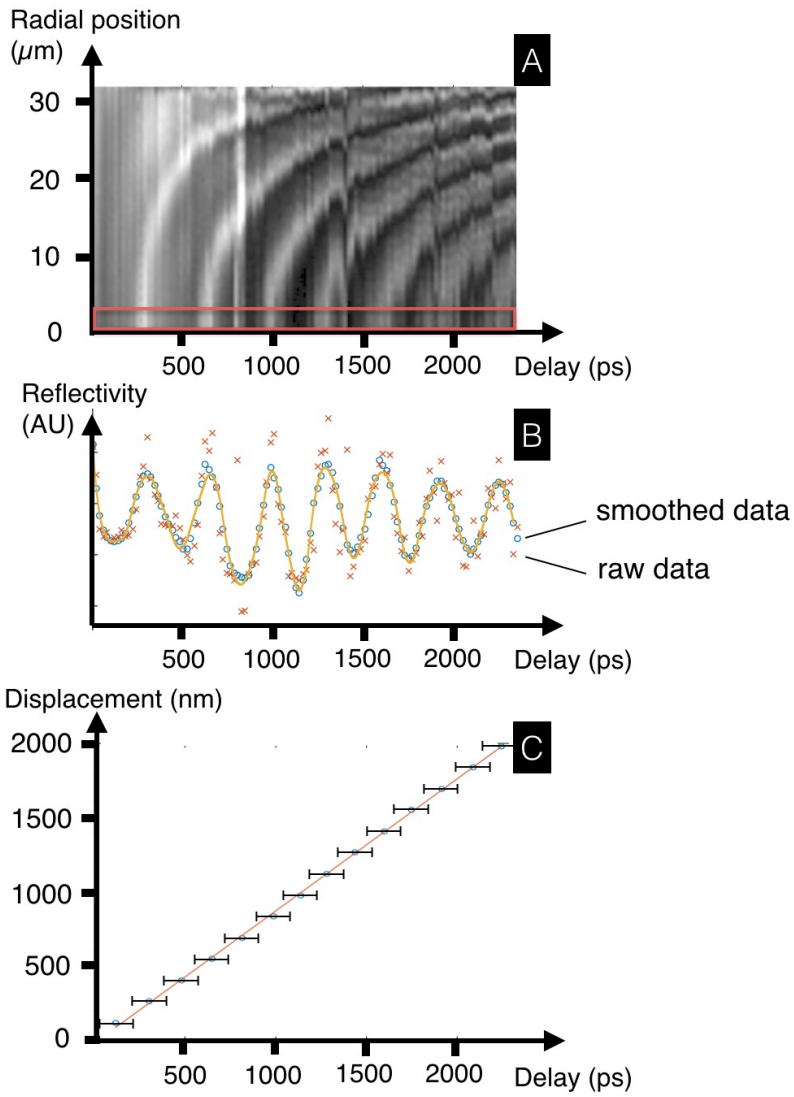

Figure 4.9: Determining the displacement of Ni films vs. time by measuring the reflected intensity in pump-probe microscopy images. The displacement of the ejected layers was measured using Newton's rings by a) creating the composite Newton's rings plot, here for irradiation with a peak fluence of 0.3 J/cm^2. A profile of reflectance vs. time is taken from the composite plot near the peak fluence. b) The raw data is smoothed, then fit with a spline function to measure the delay for each interference extremum. c) The displacement of the film calculated for each interference extremum is plotted at each measured time. The error bars correspond to 1/2 of the period between interference extrema.

the fit with an uncertainty of one half of the period. Data collection ended when the image of the Newton's rings pattern distorted due to comatic aberration, as shown in Figure 4.3 at a delay of 2100 ps.

The order of extrema is clear from images like that in Figure 4.9a, because Newton's rings exhibit the characteristic curve in their radial progression. This image also eliminates the possibility of a systematic error in displacement caused by mistaking an artifact, like that shown at 120 ps in Figures 4.4 and 4.6, for a Newtons ring. The artifact appears to be an interference maximum, in a single image, but shown in Figure 4.7 clearly does not correspond to a Newton's ring. In previous studies the displacement of the removed layers was overestimated, making it appear that the film started moving before irradiation. In that work, the order of the extrema was determined by simply counting rings, and due to the artifact, they erroneously added one more.

Figure 4.9c shows the displacement of the intrafilm layer at a peak fluence of 0.3 J/cm^2 measured using the temporal profile in Figure 4.9b. The displacement was calculated in terms of the relative phase shift, ϕ, of the reflections using Equation 4.1 adapted from Ref [4]. Constructive and destructive interference correspond to relative phase shifts of $n\pi$ or $(n + \frac{1}{2})\pi$ respectively, where n is the interference order. h_{Ni} is the thickness of Ni at the first reflecting surface. The refractive index of Ni, n_{Ni}, was taken as 2.53 + i4.4 [21]. At this time the effect of temperature on the refractive index was not considered. θ_0 is the probe angle of incidence. The angle of refraction in the metal film, θ_{Ni}, angle of refraction in the gap, θ_{gap}, and the phase change on reflection from each surface, ϕ_{R1} and ϕ_{R2}, were calculated using References [24–27].

The refractive index of the space between the ejected layers and the substrate, n_{gap}, was assumed to be 1. However, previous studies have shown n_{gap} to be 0.9 after ablation of Si tamped by SiO_2[23]. Uncertainty in n_{gap} of $\pm$ 0.1 would correspond to 22% uncertainty in any absolute measurement of displacement or velocity. The uncertainty in n_{gap} does not affect relative measurements of displacement or velocity, the conclusions in this chapter

are drawn from those relative measurements.

$$d(\phi) = \frac{\phi + \phi_{R1} - \phi_{R2} - (\frac{4\pi n_{Ni}}{\lambda_0 \cos\theta_{Ni}} + \frac{4\pi n_0 \sin?\theta_0}{\lambda_0} \tan?\theta_{Ni})h_{Ni}}{(\frac{4\pi n_{gap}}{\lambda_0 \cos\theta_{gap}} + \frac{4\pi n_0 \sin?\theta_0}{\lambda_0} \tan?\theta_{gap})} \tag{4.1}$$

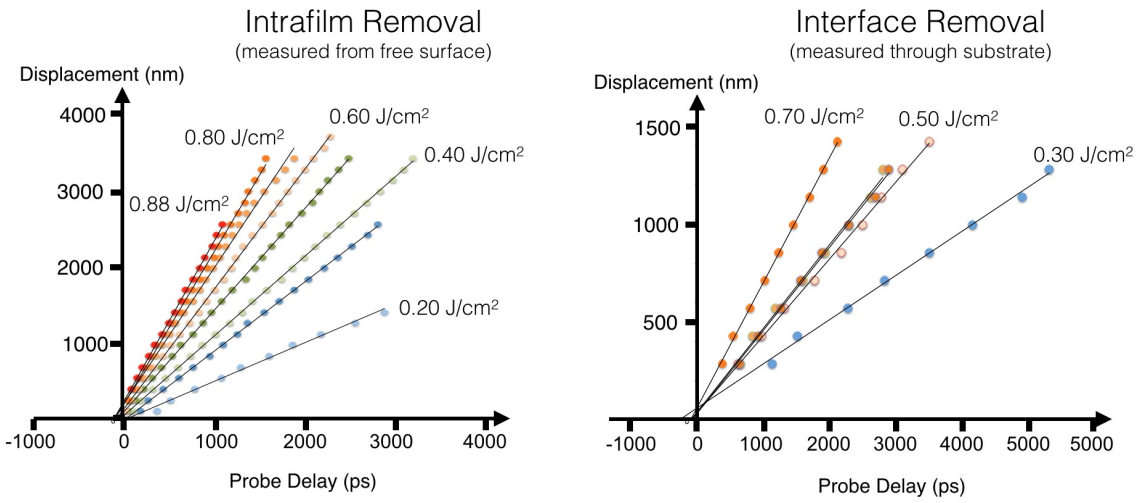

Figure 4.10: Displacement vs. time of intrafilm and interface removal layers after irradiation of 20 nm Ni films with selected fluences. The displacement of intrafilm and interface removal layers was measured using pump-probe. Each plot shows linear behavior, indicating the films are moving at constant velocity, and the intercepts of the fits are distributed around a delay of 0 ps, indicating the film rapidly separate and accelerate.

The displacement vs. delay of the intrafilm and interface removal layers were measured at a range of fluences, shown in Figure 4.10. In each case the a linear fit closely matches the data indicating the films move at a constant velocity after removal. The x-intercepts of the linear fits are distributed around the origin indicating the films reached constant velocity early after irradiation. The average and standard deviation of all the calculated x-intercepts for intrafilm and interface removal are 0 $\pm$ 50 ps and -10 $\pm$ 50 ps respectively.

Figure 4.11 shows the displacement measured from intrafilm and interface rings at an absorbed fluence of 0.25$\pm$0.02 J/cm^2, measured from the composite plots shown in Figure 4.8. The velocity of the intrafilm removal layer, ejected via liquid spallation, is five times faster that in interface removal layer. Recent MD simulation of a 20 nm Pt film on a

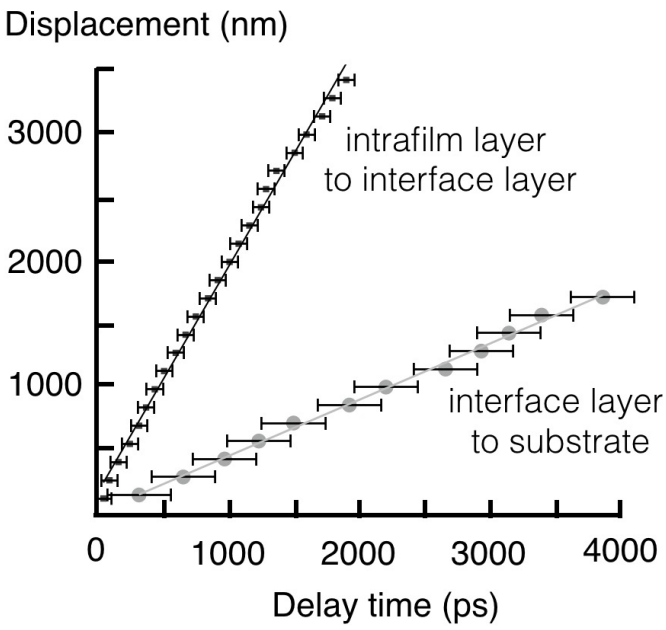

Figure 4.11: Measured displacement vs. time of intrafilm and interface removal layers after irradiation of 20 nm Ni films with the same absorbed fluence viewed from the free surface and through the glass substrate respectively. The absorbed fluence in the film was 0.25 $\pm$ 0.02 J/cm^2. Both films quickly reach constant velocity and the time intercepts of linear fits are near zero delay.

non-absorbing silica substrate irradiated with an ultrashort pulse exhibited intrafilm and interface removal[3]. The final velocity of the intrafilm layer was 300% faster than the interface removal layer, similar to our experimental results. The mechanism for interface removal was determined to be the heterogeneous nucleation and expansion of vapor at the Pt-substrate interface.

Figure 4.12 shows the speed of the intrafilm and interface removal layers at a range of fluences calculated from the linear fits shown in Figure 4.10. Error bars in Figure 4.12 represent the uncertainty introduced by the temporal error in Figure 4.11. The fluence axis has separate scales to account for the higher absorbance in the Ni for irradiation through the glass substrate. The velocity of the interface removal layer was measured from both the Ni free surface and through the glass substrate, for the same absorbed fluence the velocity is the same.

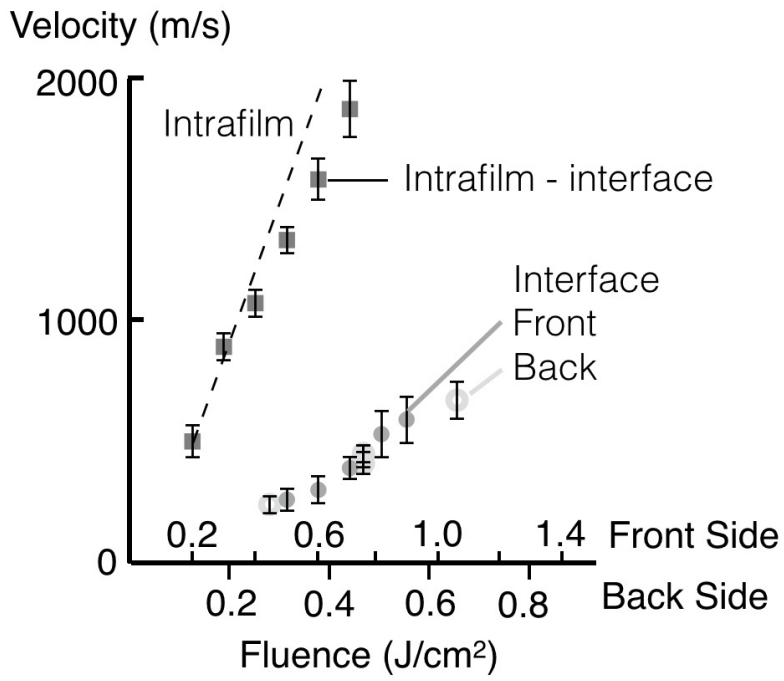

Figure 4.12: Velocity vs. fluence of intrafilm and interface removal layers after irradiation of 20 nm Ni films on glass substrates. The speed of the interface layer and the speed of the intrafilm layer minus the interface layer are plotted for several fluences. The dotted line approximates the speed of the intrafilm layer. Front and back side fluence axes are scaled to account for the relative absorbance, the direction of irradiation does not effect the speed of the interface removal layer. At the same absorbed fluence the intrafilm removal layer is moving 500% faster than the interface removal layer.

Post mortem and time-resolved measurements show that the direction of the pump pulse affects the absorption but not the removal mechanics. The depth of removal craters was identical, the removal thresholds scale by the absorption, and the speed of the interface layer is the same, as shown in Figure 4.12. Since no differences are observed in the mechanisms for removal between a front or back side pump, it is reasonable to conclude that the 20 nm Ni film was uniformly heated after irradiation and only the relaxation of the high temperature and high pressure of the film drives removal.

The actual speed of the intrafilm layer is indicated with the dashed line in Figure 4.12. The actual speed of the interface layer is determined by adding the speed measured using the interface and intrafilm Newton's rings, corresponding to the substrate-interface layer

distance and the interface-intrafilm layer distance respectively. The speed measured using Newtons rings from the intrafilm layer at fluences below the interface removal threshold fall on the dashed line because the lower 13 nm of Ni remains attached to the substrate.

Though the final velocities of the layers in our experiment and in MD simulation of 20 nm Pt films [3] are similar, the simulation shows that the intrafilm and interface layers accelerate for 1 ns and 3 ns due to the vapor pressure of Ni in the gap and the interface layer does not separate from the substrate until >100 ps. Our results indicate the interface layer separates and accelerates much faster.

It was found that linear fits of displacement for interface removal intercept the delay axis at -10 $\pm$ 50 ps. The 50 ps error corresponds to the average intercept and the standard deviation of all the x intercepts. That the linear fits of interface displacement data intercept near zero delay indicates the Ni film separates from the substrate and accelerates to its final velocity before the first interference extrema appears. Since lower acceleration would shift the intercept of the linear fit to later time, the early intercept shows the interface layer in fact reached constant velocity well before the first extrema was observed.

The displacement of moving layers at early times, before the first interference extrema, can be inferred from relative changes in reflected intensity. Figure 4.13a shows the temporal profile of reflected intensity for 0.70 $\pm$ 0.02 J/cm^2 viewed from the back and Figure 4.13b shows 0.30 $\pm$ 0.02 J/cm^2 viewed from the front, corresponding to interface and intrafilm removal respectively. The average intensity over the time range is shown with a horizontal line to guide the eye. The slopes of each profile are initially of opposite sign because in the case of interface removal viewed from the back-side, the phase difference is π (174°) upon separation. For interface removal, the uncertainty of the smoothed profile is taken as $\pm$1/6 of the amplitude, corresponding to the scatter of the raw data. The interface removal profile increases by 1/3 of the amplitude, two times the uncertainty, within 50 ps, corresponding to a displacement of 30 $\pm$15 nm according to Equation 4.1. The raw and smoothed intrafilm removal profiles decrease within 20 ps indicating separation of the intrafilm layer on a

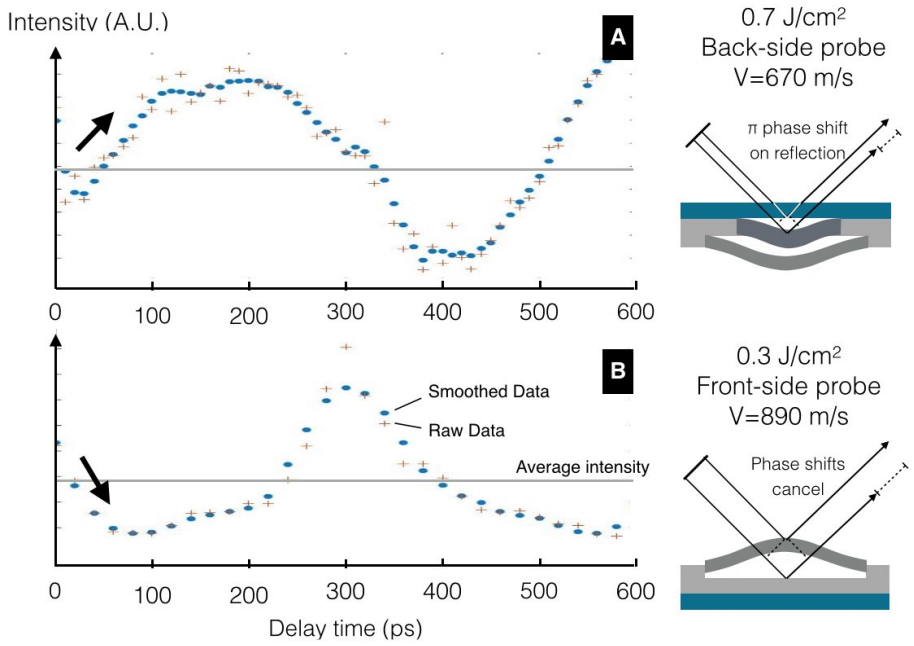

Figure 4.13: Pump-probe reflectivity showing that both the intrafilm and interface removal layers separate from the substrate within 50 ps. Temporal profiles of a) interface removal at 0.70 ± 0.02 J/cm^2 viewed from the back and b) intrafilm removal at 0.30 ± 0.02 J/cm^2 viewed from the front. Relative changes in reflected intensity before the first interference extrema can be used to determine an upper limit in the time for separation of each layer. Interface separation occurs within 50 ps and intrafilm separation occurs within 20 ps.

timescale consistent with liquid spallation.

In summary, after irradiation with an ultrashort pulse the 20 nm Ni film is uniformly heated but the intrafilm layer is ejected with a final speed 500% faster than the interface layer. The velocities of the intrafilm and interface removal layers were 500 to 2000 m/s and 300 to 700 m/s respectively in the fluence ranges studied. Several factors indicate interface removal occurs due to the nucleation and growth of vapor at the Ni-glass interface. The relative velocity of the intrafilm and interface removal layers are consistent with recent MD simulations where the driving force for interface removal is expansion of vapor between the layers and the interface. The interface removal region exhibits relatively high roughness in AFM, inconsistent with liquid spallation. And a simplified thermodynamic calculation using the absorbed energy and the thermochemical data of Ni at constant pressure shows that the majority of the Ni film will vaporize at the interface removal threshold. By refining the technique of measuring Newtons rings using pump-probe microscopy, it was shown that the Ni-glass interface breaks within 50 ps and the interface layer reaches constant velocity well before the first interference extrema. The rapid separation and acceleration of the interface removal layer conflict with previous models of diffusion-limited nucleation and growth.

4.5 The Role of the Vapor Dome in Interface Removal

The results of pump-probe microscopy indicate that interface removal involves rapid vaporization at the interface on a timescale similar to mechanical relaxation. To better understand the dynamics of ultrathin films irradiated with a femtosecond pulse, hydrodynamic simulations were performed of 20 nm thick Ni films on glass substrates for irradiation conditions consistent with pump-probe results[9]. Those simulations used the 1D hydrodynamic code HYADES[28] and the SESAME equation of state for nickel. Within 50 picoseconds, the time for separation and acceleration of the Ni film by the formation of vapor, the state of

the film enters and then exits the vapor dome, a region in the T-ρ phase diagram where the liquid and vapor phases coexist.

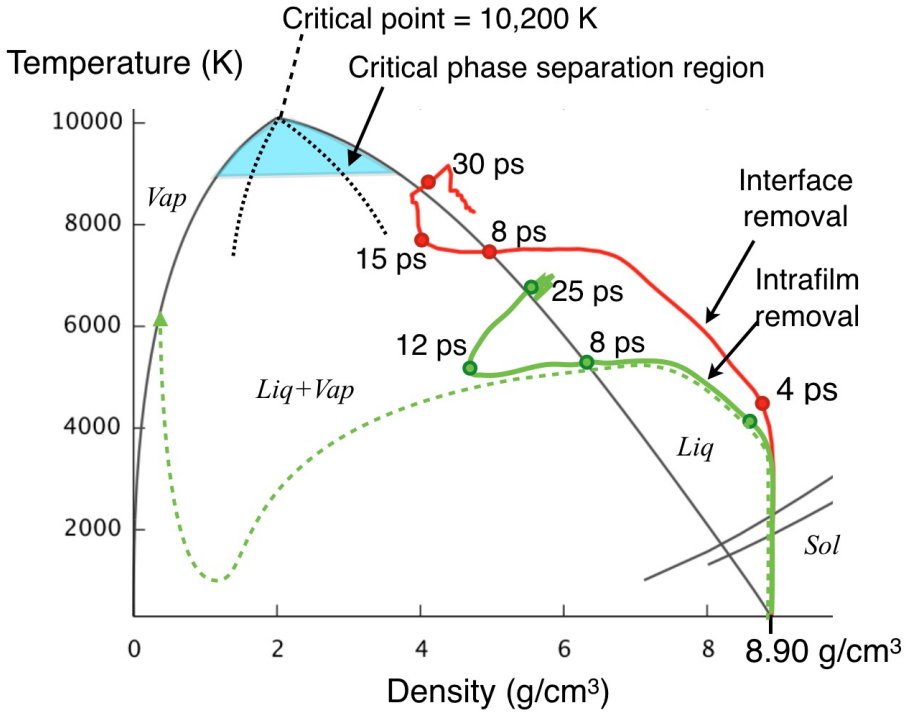

Figure 4.14: Hydrodynamic simulations of ultrathin Ni films corresponding to conditions of intrafilm and interface removal of 20 nm Ni films. The relaxation dynamics of 20 nm Ni films in the temperature-density phase diagrams were modeled using a 1-D HYADES hydrodynamic code. With increasing fluence the state enters the vapor dome at higher temperature, or kinetic energy, and remains there for a longer period of time. Previous simulations show that material driven into the critical phase separation region is unstable and will decompose into vapor and liquid via spinodal-like homogeneous nucleation of vapor. Reprinted with the permission of Ben Torralva.

Figure 4.14 shows the dynamic relaxation path Ni film through the density-temperature phase diagram in two cases. Each path was created by monitoring the state of a layer of Ni in the simulation. The lower path corresponds to Ni in the intrafilm removal layer at the threshold for liquid spallation. Initially the lattice increases in temperature at solid density and melts. The hot liquid then expands, reducing in density, and passes into the vapor dome. The state of the metal exits the vapor dome and cools along the liquid line, increasing in density, until it returns to its original point on the phase diagram. On exiting

the vapor dome it is observed that the density fluctuates before settling on the liquid line. The dotted line indicates the approximate path of the layer where liquid spallation occurs; this layer traverses the vapor dome due to cavitation and transforms to vapor, breaking the liquid film at a depth of 7 nm.

The upper path corresponds to Ni in the interface layer at the measured interface removal threshold. As before, the Ni layer increases in temperature at solid density and melts, but now reaches higher temperature due to the higher laser fluence. The liquid nickel expands and the density falls, driving into the vapor dome, and then exiting the vapor dome to the liquid line. Again, the density fluctuates before settling on the liquid line. In this case, the Ni remains inside the vapor dome longer and at higher temperature. The path approaches the critical phase separation region but does not enter it.

Previous simulations of bulk materials irradiated with much higher fluence show that material that enters the vapor dome within 10% of the critical temperature, called the critical phase separation region, is thermodynamically unstable[29, 30]. In this regime there is no kinetic or energetic barrier to the formation of vapor, and the metal decomposes into liquid and vapor within picoseconds via spinodal-like homogeneous nucleation of vapor. However, the trajectory of metal through the temperature-density phase diagram is similar after irradiation with lower fluences and spinodal-like variations in density still occur when the material enters the vapor dome outside the critical point phase separation region. However outside the critical point phase separation region the spinodal-like instability does not result in the formation of stable homogeneous nuclei and the material simply returns to the liquid state. In the case of the ultrathin Ni film, the metal-substrate interface can stabilize vapor nuclei that form at lower temperatures, leading to heterogeneous nucleation at the Ni-glass interface breaking the interface within tens of picoseconds as seen in time resolved experiments[31].

Entering the vapor dome at moderate fluence, as in this mechanism, requires the high temperature, high pressure non-equilibrium and the unloading rarefaction wave decreasing

the density of the liquid, that are unique to femtosecond laser irradiation. The same relaxation path is not available using longer pulses where heating and hydrodynamic expansion occur concurrently. In that case, the state of the target material follows the equilibrium lines through the phase diagram[32]. With a longer excitation pulse, entering the vapor dome would take a comparatively high fluence. Non-equilibrium conditions would occur early during the laser pulse, but then the remainder of the pulse energy would be deposited driving excessive removal. Material that entered the vapor dome does not remain on the surface.

The method of irradiating ultrathin films makes it possible to retain Ni that was excited to high temperatures in the vapor dome by reducing the depth of material removed by liquid spallation. In the case of bulk Ni irradiated at 0.36 J/cm^2 liquid spallation occurs to a depth of 20 nm. For the 20 nm film irradiated at the same fluence, the depth of liquid spallation layer is just 7 nm.

In summary, the removal dynamics of 20 nm Ni films from glass substrates were observed using time-resolved pump-probe microscopy. It was found that the 20 nm film is removed in two distinct layers corresponding to the area and depth of the intrafilm and interface removal regions of the damage crater. The velocity of the interface removal layer is approximately 20% of the velocity of the intrafilm removal layer, in agreement with previous MD simulations where interface removal is driven by the formation of vapor at the Ni glass interface. However, the separation and acceleration of the layers was much faster than in the MD simulation. Both the intrafilm and interface removal layers separated within 50 ps and both layers reached their maximum velocity within 50 ps of irradiation, the resolution limit of pump-probe using Newton's rings.

Hydrodynamic simulations of 20 nm Ni film removal show that Ni enters the vapor dome in the Ni density vs. temperature phase diagram for a short time after laser excitation and adiabatic expansion. In the vapor dome liquid and vapor are in equilibrium and vapor forms homogeneously similar to spinodal decomposition, without kinetically lim-

ited nucleation. Homogeneous vapor nuclei form and are stable if the liquid is driven into the critical phase separation region, defined as within 10% of the temperature at the critical point. The fluence for interface removal drives Ni close to, but not inside, the critical phase separation region, so stable vapor nuclei cannot form homogeneously. The Ni-glass interface provides a stable location for vapor nuclei that form inside the vapor dome, and separation of the interface can occur on the observed timescale of 50 ps.

References

1. Murphy, R. D., Torralva, B. & Yalisove, S. M. The role of an interface on Ni film removal and surface roughness after irradiation by femtosecond laser pulses. *Applied Physics Letters* **102,** 181602 (2013).
2. Murphy, R. D. *Femtosecond Laser Interactions at Interfaces and Their Applications.* PhD thesis (University of Michigan, 2013).
3. Rouleau, C. M., Shih, C.-Y., Wu, C., Zhigilei, L. V., Puretzky, A. A. & Geohegan, D. B. Nanoparticle generation and transport resulting from femtosecond laser ablation of ultrathin metal films: Time-resolved measurements and molecular dynamics simulations. *Applied Physics Letters* **104,** 193106 (May 12, 2014).
4. Harris, L., Beasley, J. K. & Loeb, A. L. Reflection and transmission of radiation by metal films and the influence of nonabsorbing backings. *JOSA* **41,** 604–610 (1951).
5. Ivanov, D. S., Lin, Z., Rethfeld, B., O′Connor, G. M., Glynn, T. J. & Zhigilei, L. V. Nanocrystalline structure of nanobump generated by localized photoexcitation of metal film. *Journal of Applied Physics* **107,** 013519 (2010).
6. Ivanov, D. S. & Zhigilei, L. V. Combined atomistic-continuum modeling of short-pulse laser melting and disintegration of metal films. *Physical Review B* **68,** 064114 (Aug. 28, 2003).
7. Wellershoff, S.-S., Hohlfeld, J., Güdde, J. & Matthias, E. The role of electron–phonon coupling in femtosecond laser damage of metals: *Applied Physics A* **69,** S99–S107 (S1 Dec. 1999).
8. Chase, Malcolm W. NIST-JANAF Thermochemcal Tables. *Journal of Physical and Chemical Reference Data* **Monograph No. 9,** 1–1951 (1998).
9. *Private Communication* in collab. with Torralva, B. 2016.
10. Von der Linde, D., Sokolowski-Tinten, K. & Bialkowski, J. Laser–solid interaction in the femtosecond time regime. *Applied Surface Science* **109–110,** 1–10 (Feb. 1, 1997).
11. Sokolowski-Tinten, K., Bialkowski, J., Cavalleri, A., Von der Linde, D., Oparin, A., Meyer-ter-Vehn, J. & Anisimov, S. I. Transient states of matter during short pulse laser ablation. *Physical Review Letters* **81,** 224–227 (1998).
12. Von der Linde, D. & Sokolowski-Tinten, K. The physical mechanisms of short-pulse laser ablation. *Applied Surface Science* **154,** 1–10 (2000).
13. Bonse, J., Bachelier, G., Siegel, J. & Solis, J. Time- and space-resolved dynamics of melting, ablation, and solidification phenomena induced by femtosecond laser pulses in germanium. *Physical Review B* **74,** 134106 (Oct. 6, 2006).

14. Bonse, J., Bachelier, G., Siegel, J., Solis, J. & Sturm, H. Time- and space-resolved dynamics of ablation and optical breakdown induced by femtosecond laser pulses in indium phosphide. *Journal of Applied Physics* **103,** 054910 (Mar. 1, 2008).

15. Ionin, A. A., Kudryashov, S. I., Seleznev, L. V. & Sinitsyn, D. V. Dynamics of the spallative ablation of a GaAs surface irradiated by femtosecond laser pulses. *JETP Letters* **94,** 753–758 (Jan. 2012).

16. Shank, C., Yen, R. & Hirlimann, C. Time-Resolved Reflectivity Measurements of Femtosecond-Optical-Pulse-Induced Phase Transitions in Silicon. *Physical Review Letters* **50,** 454–457 (Feb. 1983).

17. Downer, M. C., Fork, R. L. & Shank, C. V. Femtosecond imaging of melting and evaporation at a photoexcited silicon surface. *JOSA B* **2,** 595–599 (1985).

18. Rapp, S., Domke, M., Schmidt, M. & Huber, H. Physical Mechanisms during fs Laser Ablation of Thin SiO2 Films. *Physics Procedia* **41,** 734–740 (Jan. 2013).

19. Bartl, D., Michalowski, A., Hafner, M., Letsch, A., Nolte, S. & Tünnermann, A. Time-resolved study of back side ablated molybdenum thin films by ultrashort laser pulses. *Applied Physics A* **110,** 227–233 (Aug. 31, 2012).

20. Domke, M., Rapp, S., Schmidt, M. & Huber, H. P. Ultra-fast movies of thin-film laser ablation. *Applied Physics A* **109,** 409–420 (July 31, 2012).

21. Ordal, M. A., Bell, R. J., Alexander, J., Long, L. L. & Querry, M. R. Optical properties of fourteen metals in the infrared and far infrared: Al, Co, Cu, Au, Fe, Pb, Mo, Ni, Pd, Pt, Ag, Ti, V, and W. *Applied Optics* **24,** 4493–4499 (Dec. 15, 1985).

22. Malitson, I. H. Interspecimen comparison of the refractive index of fused silica. *JOSA* **55,** 1205–1208 (1965).

23. McDonald, J. P., Nees, J. A. & Yalisove, S. M. Pump-probe imaging of femtosecond pulsed laser ablation of silicon with thermally grown oxide films. *Journal of Applied Physics* **102,** 063109 (2007).

24. Doi, T., Toyoda, K. & Tanimura, Y. Effects of phase changes on reflection and their wavelength dependence in optical profilometry. *Applied optics* **36,** 7157–7161 (1997).

25. Bennett, J. Precise Method for Measuring Absolute Phase Change on Reflection. *Journal of the Optical Society of America* **54,** 612–624 (1964).

26. Dubois, A. Effects of phase change on reflection in phase-measuring interference microscopy. *Applied Optics* **43,** 1503–1507 (Mar. 1, 2004).

27. Born, M. & Wolf, E. *Principles of Optics: Electromagnetic Theory of Propagation, Interference and Diffraction of Light* 871 pp. (Elsevier, June 1, 2013).

28. Rubenchik, A. M., Feit, M. D., Perry, M. D. & Larsen, J. T. Numerical simulation of ultra-short laser pulse energy deposition and bulk transport for material processing. *Applied Surface Science* **127,** 193–198 (1998).

29. Povarnitsyn, M. E., Itina, T. E., Sentis, M., Khishchenko, K. V. & Levashov, P. R. Material decomposition mechanisms in femtosecond laser interactions with metals. *Physical Review B* **75,** 235414 (June 2007).

30. Vidal, F., Johnston, T. W., Laville, S., Barthélemy, O., Chaker, M., Le Drogoff, B., Margot, J. & Sabsabi, M. Critical-Point Phase Separation in Laser Ablation of Conductors. *Physical Review Letters* **86,** 2573–2576 (Mar. 19, 2001).

31. Schrider, K. J., Torralva, B. & Yalisove, S. M. The dynamics of femtosecond pulsed laser removal of 20 nm Ni films from an interface. *Applied Physics Letters* **107,** 124101 (Sept. 21, 2015).

32. Perez, D. & Lewis, L. Thermodynamic evolution of materials during laser ablation under pico and femtosecond pulses. *Applied Physics A* **79** (July 26, 2004).

CHAPTER 5

Femtosecond Laser Formation of Nanocrystalline Materials

Submitted for Publication: Schrider, K. J., Torralva, B. & Yalisove, S. M. Nano-crystalline Ni-W Alloy Formation via Femtosecond Laser Induced Extreme States. Applied Physics Letters (March 10, 2017).

Femtosecond laser driven heating and quenching of a thin surface layer drives cooling rates much greater than other methods sufficient to significantly undercool materials and form glassy or nanocrystalline phases. However, nano-crystalline or amorphous phases of pure metals are not thermally stable and are not typically observed experimentally at the surface of metals irradiated with a single femtosecond pulse[1]. Instead the surface layer regrows epitaxially with crystal grains in the bulk, either during solidification or possibly via coarsening after solidification. In some cases the rapidly resolidified material contains a large concentration of defects and twin boundaries[2, 3]. Recent molecular dynamics simulations of femtosecond laser irradiated bulk Ag and 20 nm Ni films suggest femtosecond laser melt and quench of monatomic metals results in a fine nano-crystalline microstructure within 300 ps via homogeneous nucleation[4, 5].

It has been shown previously that nano-crystalline materials can be stabilized by the addition of a solute species that has limited solubility. The solute preferentially segregates to grain boundaries, reduces the grain boundary free energy, and effectively "pins" the boundary preventing grain growth[6]. It was hypothesized that an analogous microstructure

could be created via femtosecond laser melting and quenching of multilayer metal thin films with suitable alloying species.

It has been demonstrated in previous studies that femtosecond laser irradiation can be used to mix metals at interfaces, either at a single interface or in multilayer materials. Previous investigations focussed on metals that mixed readily– those metal systems are not suitable for solute stabilization of grain boundaries. This chapter investigates femtosecond laser intermixing of metals that do not alloy readily. The Ni-W system was selected because solute stabilization of grain boundaries has been previously observed in electrodeposited films. W is soluble in Ni up to 12.4 at% but during electrodeposition W will preferentially segregate to sites on grain boundaries for compositions ranging from 5 to 30 at% without forming equilibrium ordered Ni-W phases[7, 8].

It is shown that femtosecond laser irradiation of ultrathin multilayer Ni-W films on Ni substrates results in a removal crater similar to pure Ni films on glass substrates. The multilayer Ni-W film exhibits a two-stepped removal crater. Intrafilm removal removes the top half of the multilayer Ni-W film and interface removal occurs at the interface of the Ni-W film and the Ni substrate. Cross section STEM shows that above a local fluence of 0.34 J/cm^2 the Ni-W in the intrafilm removal region that remains on the Ni substrate is uniformly mixed. NBED of the mixed Ni-W film is consistent with nanocrystalline metal.

The depth of material removal by liquid spallation is suppressed in ultrathin films. Material in the intrafilm removal region was driven to high temperatures and extreme, non-equilibrium states in the phase diagram after irradiation. After irradiation of a bulk sample, material excited with a similar energy density would be close to the surface and removed by liquid spallation. After irradiation of an ultrathin film, some material excited with the same energy density remains on the substrate in the intrafilm removal region. The results of the previous chapter and hydrodynamic simulations of the state of Ni during relaxation are used to gain insight into the evolution of the Ni-W film in the intrafilm removal region. The possible influence of the vapor dome on mixing the Ni and W layers is also considered.

The method of laser mixing of ultrathin multilayer films that is presented in this chapter could be applied to almost any system; it is only necessary that the materials can be deposited in a sufficiently thin film on the same substrate. This process is unique since materials are heated to temperatures close to or above the vaporization temperature. In the future this method could be used to study the microstructure of a uniform alloy formed with nearly any composition.

5.1 Femtosecond Laser Interaction with Ultrathin Multilayer Ni-W Films

Multilayer Ni-W films were prepared by depositing 12 alternating layers of 1.4 nm W and 2.5 nm Ni on a substrate. The composition of the film is 27 at% W. W composed the top layer, at the free surface. The substrate consists of 100 nm Ni, serving as a heat sink, 300 nm SiO_2 as a diffusion barrier to prevent Ni silicide formation, and a 500 μm thick Si support. Figure 5.1 shows Scanning Transmission Electron Microscopy (STEM) images of the as-deposited multilayer Ni-W film. The High Angle Annular Dark Field (HAADF) image, also called z-contrast, shows the alternating Ni and W layers. The bright layers in Figure 5.1 correspond to W (z=74) and the dark layers correspond to Ni (z=28). Areas of periodic contrast in HAADF images are caused by the lattice. The interplanar spacings were measured by taking an Fast Fourier Transform (FFT) of lattice contrast and indexing them like a diffraction pattern. On the right of Figure 5.1, pure grains of Ni and W were indexed to verify the composition of the layers. Multiple grains are visible in each as-deposited layer.

Multilayer Ni-W films exhibit two distinct thresholds for removal after irradiation with a single pulse, shown in Figure 5.2. At a fluence of 0.20 J/cm^2 the top half of the multilayer Ni-W film is removed. At a fluence of 0.47 J/cm^2 the entire Ni-W film is removed exposing the Ni substrate. As shown in Figure 5.2, intrafilm removal by liquid spallation occurs at

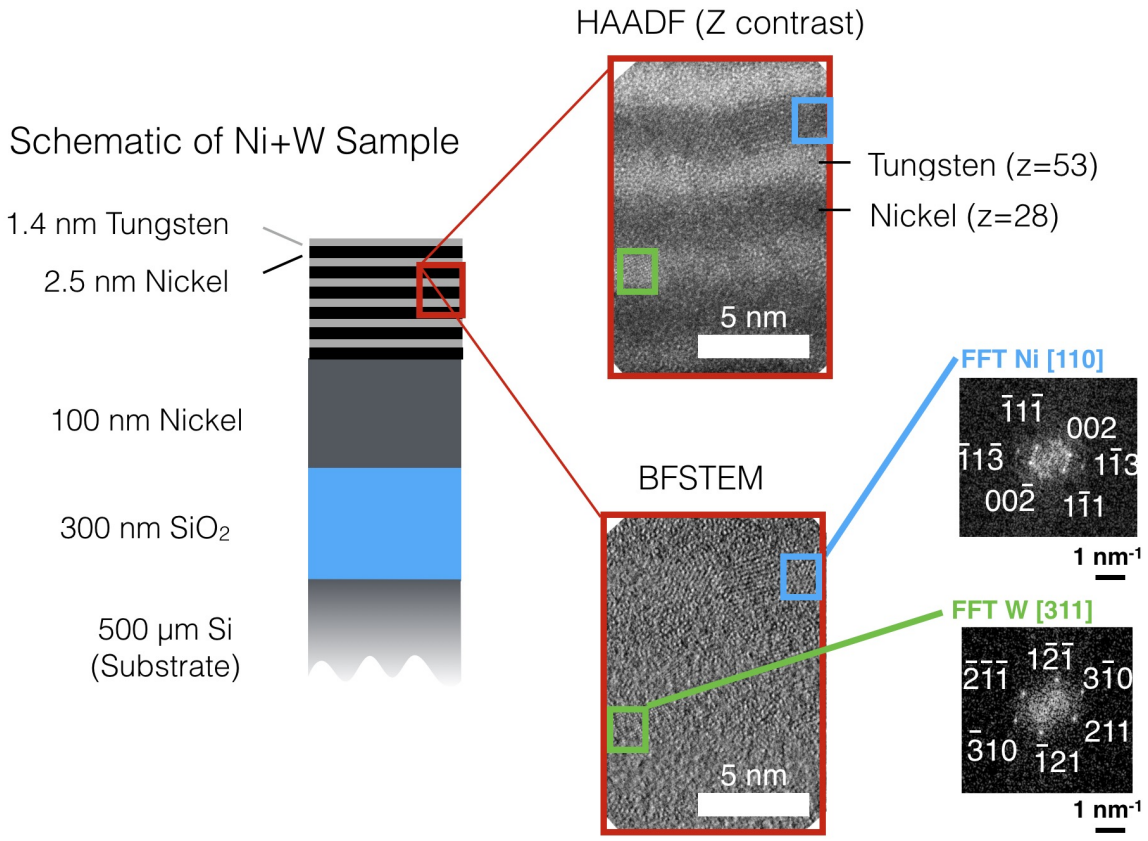

Figure 5.1: Schematic of the structure of as-deposited multilayer Ni-W films. Ni-W films were prepared by depositing of 12 alternating layers of 1.4 nm W and 2.5 nm Ni on a substrate consisting of 100 nm Ni, serving as a heat sink, 300 nm SiO_2 as a diffusion barrier to prevent Ni silicide formation, and a 500 μm Si wafer support. HAADF STEM of the as-deposited film shows distinct layers of polycrystalline BCC W and FCC Ni.

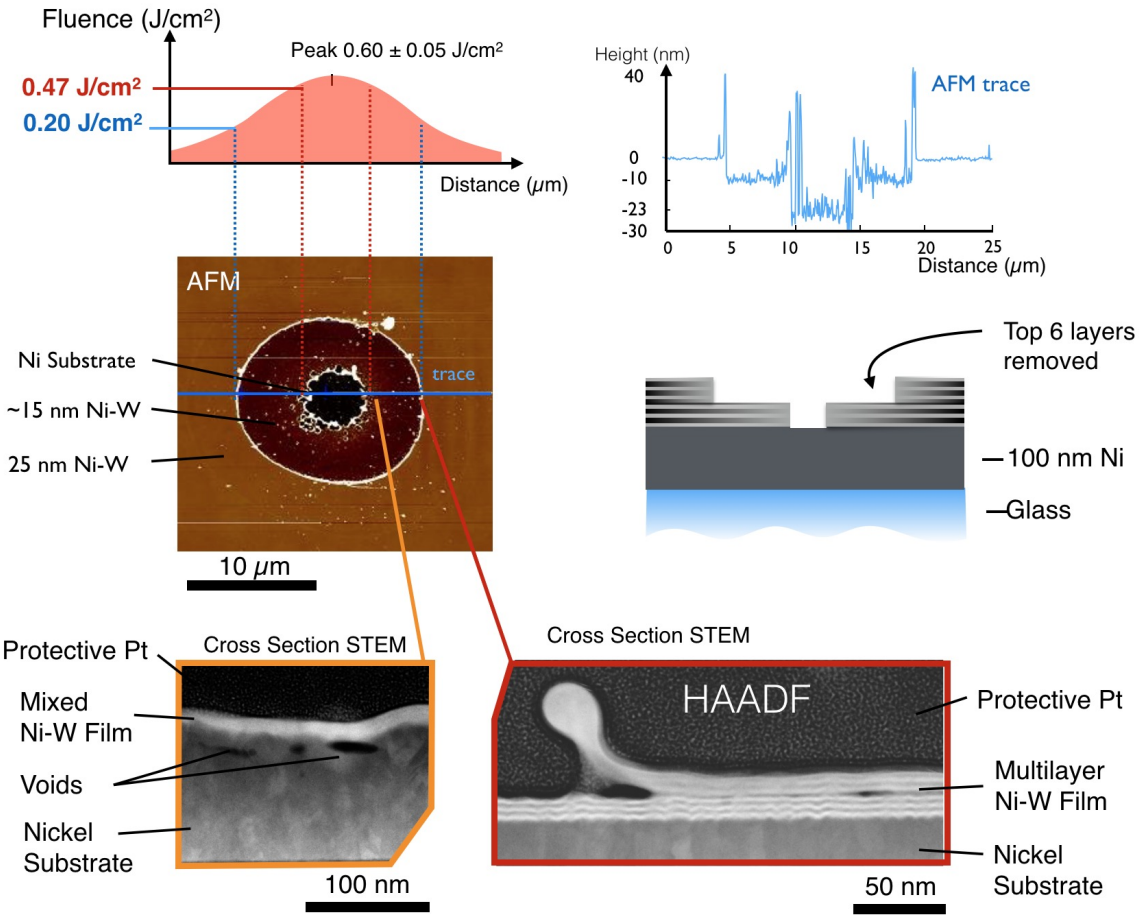

Figure 5.2: Damage craters after irradiation of multilayer Ni-W films on Ni substrates. Multilayer Ni-W films on Ni substrates exhibit intrafilm and interface removal, similar to pure ultrathin Ni films on glass. Intrafilm removal occurs at half the thickness of the Ni-W film, interface removal occurs at the thick Ni substrate.

the third Ni layer from the surface, removing the top three W layers. It is interesting to note that the ratio between the intrafilm and interface removal thresholds are the same as pure Ni on glass. As shown in Figure 5.2, irradiation with a peak fluence greater than 0.47 J/cm^2 results in a two stepped removal crater that is similar to ultrathin Ni films on glass.

Surrounding the removal craters, a ring of bright contrast was observed using Scanning Electron Microscopy (SEM) with a 5 kV accelerating voltage, shown in figure 5.2. The threshold of the ring was 0.15 J/cm^2. The local fluence to melt Ni and W in the multilayer Ni-W film was estimated to be 0.10 and 0.19 J/cm^2 respectively by determining the total fluence absorbed per mole by the Ni and W systems and comparing the enthalpy with the JANAF thermochemical tables[9]. The calculation assumed that the laser energy absorbed by the multilayer film was uniformly distributed before melting; this is a reasonable assumption since the entire Ni-W film is much less than the skin depth. This simplified calculation does not account reflections from interfaces in the multilayer film or electron transport out of the Ni-W film into the Ni substrate.

5.2 Femtosecond Laser Mixing of Ni-W

Cross section STEM was used to characterize the microstructure of the Ni-W film after irradiation with respect to the local fluence.

Figure 5.3a shows multilayer Ni-W films after irradiation with local fluences of 0.28 and 0.39 J/cm^2; Figure 5.3b shows another film after irradiation with local fluences of 0.25 and 0.34 J/cm^2. In Figure 5.3 the top 3 layers of Ni and W have been removed via liquid spallation. At 0.25 and 0.28 J/cm^2 distinct Ni and W layers are observed. At 0.34 and 0.39 J/cm^2 the layers of Ni and W are no longer distinguishable. The transition from distinct layers to an uniform mixed layer occurs over a narrow fluence range from 0.28 to 0.34 J/cm^2. The sharpness of layers of Ni and W decreases as the local fluence approaches the threshold fluence for mixing, this could be caused partial intermixing of the Ni and W

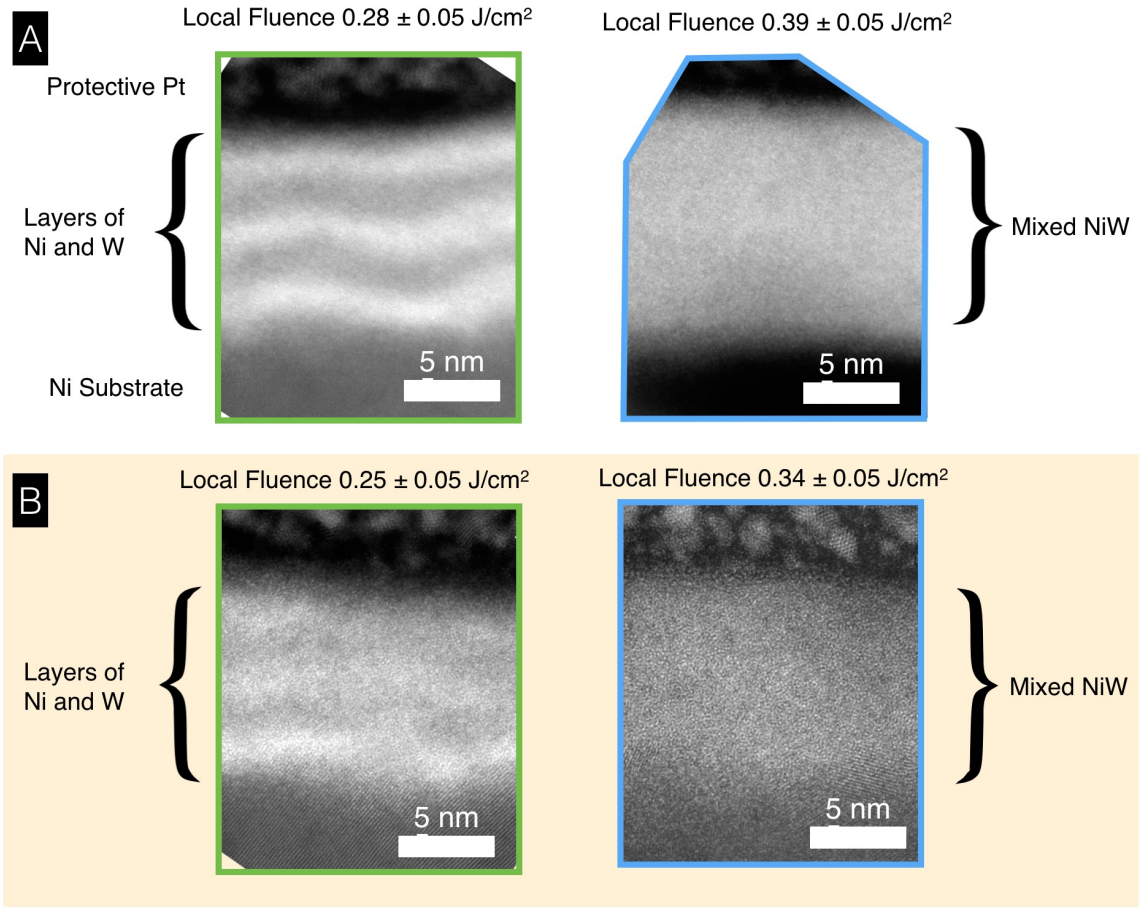

Figure 5.3: Cross section STEM of multilayer Ni-W films after irradiation above and below the threshold fluence for mixing. Ni and W layers in the intrafilm removal region transition from having distinct Ni and W layers to mixed over a local fluence range of 0.28 and 0.34 J/cm^2. a) and b) show HAADF images from two different experiments with similar parameters. Layers of Ni and W are observed below 0.28 J/cm^2 and a film of mixed Ni-W is observed above 0.34 J/cm^2.

layers. The edges of the Ni and W layers may also result from the STEM probe not being aligned parallel to the layers at higher fluences where the Ni substrate and multilayer Ni-W film exhibit increased roughness.

In Figure 5.2, cross section STEM of the multilayer Ni-W film near the interface removal threshold shows that large voids form in the Ni substrate at the interface with the mixed Ni-W film. It is probable that these voids are produced by melting and vaporization at the interface, but that vapor formation does not proceed far enough to drive removal.

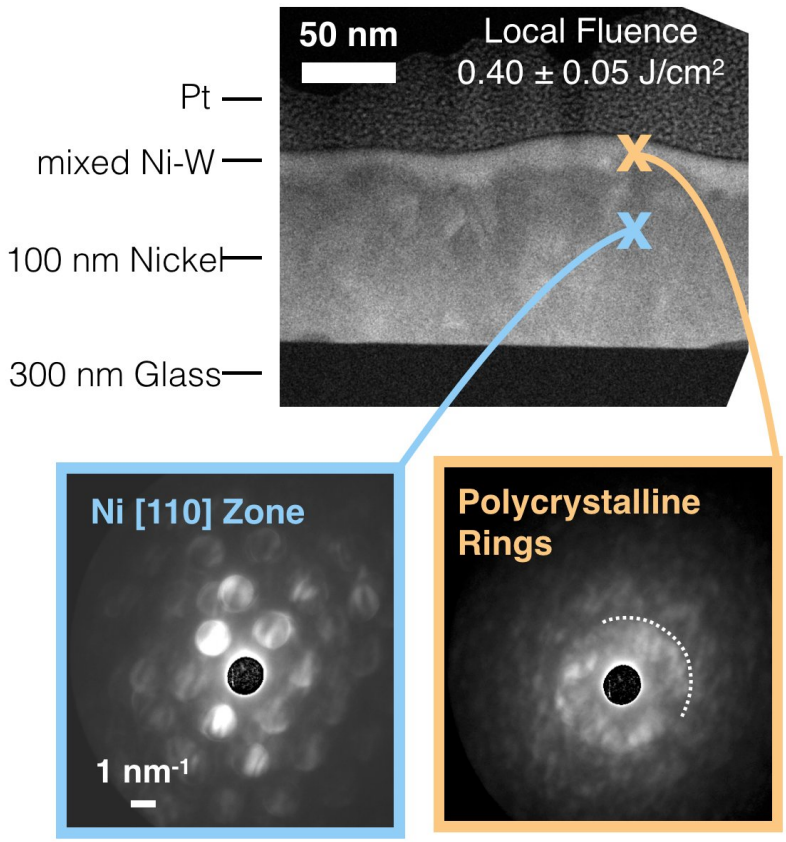

Figure 5.4: Cross section STEM and NBED of multilayer Ni-W films after femtosecond laser mixing. The top HAADF STEM image shows the Ni substrate with a mixed Ni-W film on its top surface. The mixed Ni-W film is brighter due to the higher average Z. A single crystal NBED pattern is observed over the Ni substrate. The multilayer Ni-W film irradiated with a local fluence between 0.30 and 0.47 J/cm^2 exhibits a distinct polycrystalline diffraction pattern consisting of many individual diffraction spots forming a ring. A dashed line is overlaid with the diffraction pattern to indicate the edge of the first polycrystalline ring.

Nano-beam Electron Diffraction (NBED) of the irradiated film was performed. NBED patterns contain disks instead of sharp spots because the beam is focused not parallel. The nano-beam was ~2 nm in diameter, making it possible to place the probe over the 10 nm thick mixed Ni-W film and exclude both the Ni substrate and the protective Pt coating. Nano-beam electron diffraction patterns of the Ni-W film and Ni substrate are shown in Figure 5.4. STEM shows the Ni substrate layer consists of grains approximately 20 nm in diameter. A single crystal diffraction pattern corresponding to the [110] zone axis is observed in the Ni substrate layer. The NBED pattern of the mixed Ni-W film shows many individual diffraction spots forming a ring indicating the Ni-W film is polycrystalline containing many randomly oriented grains. Lattice contrast was not observed in the irradiated film using HAADF or BF STEM implying that grains in the mixed material are very small relative to the film thickness, possibly approaching an amorphous microstructure.

The system examined in this work and the characterization methods used were similar to previous studies of short range order in annealed metallic glasses on a length scale of several nanometers[10–13]. In that work, short range order was not always clear in HRSTEM but was detectable using NBED appearing as a selection of NBED spots overlaid with the rings produced by scattering in the metallic glass. For Ni-W with an overall composition of 27%, as used in this chapter, electrodeposited films had a grain size of ~2 nm[14]. The NBED pattern of the mixed Ni-W film in Figure 5.4 is consistent with the anticipated microstructure consisting of small grains and a large volume fraction of grain boundaries.

5.3 Formation of Thermally Stable Nanocrystalline Microstructure

The nanocrystalline Ni-W microstructure is observed after the molten alloy rapidly quenches via thermal transport into the Ni substrate. The quench rates after femtosecond laser ir-

radiation can exceed 10^{11} K/s. However, glassy or nanocrystalline microstructure is not experimentally observed after irradiation of pure metal targets irradiated with a single femtosecond pulse. Instead the melt resolidifies epitaxially with the underlying solid material, or coarsening causes larger grains in the bulk to consume the thin nanocrystalline layer at the surface. Previous MD simulations of bulk Ag and Ni ultrathin films also show that during femtosecond laser driven melting and quenching, the solid phase nucleates homogeneously when the molten metal is undercooled to 60% of the melting temperature. The high concentration of nuclei with random orientation results in a nanocrystalline microstructure at the surface of the Ag target[4, 5].As discussed in Section 2.3.1, nanocrystalline phases of pure metals are thermally unstable and coarsen at a fraction of the melt temperature and in some cases at room temperature. In the case of Ni, coarsening has been observed to begin near 100 °C[15]. Additionally the nanocrystalline layer at the surface of metals would be very thin, less than the melt depth, making it possible for the nanocrystalline film to be removed by coarsening before it can be examined. It is possible that after irradiation of multilayer Ni-W films, the nanocrystalline microstructure formed during resolidification is stabalized by grain boundary segregation of W, similar to the structure of electrodeposited Ni-W films[7, 8]. The nanocrystalline film produced in this work was characterized several weeks after irradiation, indicating that the nanocrystalline material is thermally stable at room temperature.

It was observed that melting and quenching after irradiation is insufficient to mix the Ni and W layers. The calculated melt thresholds of Ni and W in the film are 0.10 and 0.19 J/cm^2 respectively and intrafilm removal by liquid spallation occurs above 0.20 J/cm^2. Also above 0.15 J/cm^2 a contrast change is observed in SEM indicating damage, but not removal. To mix, the layers must be irradiated between 0.28 and 0.32 J/cm^2. Mixing of the Ni and W layers does not occur until almost two times the melt threshold. It is also observed that the transition from unmixed layers to mixed layers occurs over a narrow fluence range. Unlike femtosecond laser melting and quenching in a bulk material, the material in the intrafilm

removal crater has been pushed in to conditions far from equilibrium. In bulk materials, liquid spallation occurs on the order of half the melt depth. In most situations material that enters the vapor dome near the critical point is near the surface and is removed by liquid spallation[16]. In this work, the ultrathin film was uniformly heated after irradiation but the depth of liquid spallation is limited to approximately half the thickness of the ultrathin film. Material that was excited to high temperature within the vapor dome, normally lost after irradiation of bulk materials, was retained in the intrafilm removal region. Both thermally driven diffusion and the non-equilibrium response of material after femtosecond laser irradiation are discussed here.

With increasing fluence the initial temperature of the film increases and the molten material takes longer to quench via heat transport into the substrate. As the delay for solidification increases the diffusion length of Ni and W atoms in the melt increases. It is possible that at sufficiently high fluence the diffusion length is greater than the thickness of the layers resulting in a homogeneous film. A simple calculation of the diffusion length, $L = \sqrt{D\tau}$, was performed using D, the diffusion coefficient of W in liquid Ni and τ, the time before resolidification of the intrafilm removal layer. Calculations performed in previous investigations of the melting and resolidification of a pure Ni target show that just above the threshold for surface melting, the melt depth is 20 nm and the resolidification is complete within 0.6 ns[17]. At higher fluences near the threshold for liquid spallation the melt depth is 80 nm and resolidification is complete after 3 ns. Above the threshold for liquid spallation, approximately half of the molten layer is removed and only the remaining half of the molten layer solidifies on the surface. Since the velocity of the solidification front is nearly constant in the simulation solidification of the remaining melted material will likely be complete within 1.5 ns. The diffusion coefficient of dilute W in Ni just above the melt temperature is $2.510^{-}9$ m^2/s[18], near the self diffusion coefficient of Ni at the melting point, $310^{-}9$ m^2/s[19]. The diffusion length defines the average distance that the diffusing species will travel. In a multilayer film, the species travel half the bilayer

thickness to become evenly distributed. Using the diffusion coefficients and the estimated cooling time of 1.5 ns, the diffusion length is 2.2 nm at the threshold for intrafilm removal, already slightly greater than half of the bilayer thickness.

Thermally driven diffusion causes very little intermixing in the fluence range near the intrafilm removal threshold of the multilayer Ni-W film, despite a sufficient estimated diffusion length. Taking into account the cooling behavior of the film after irradiation one would expect to observe more mixing just below the intrafilm removal threshold where a thicker heated film remains on the surface. In fact very little mixing occurs in the until the laser fluence is 50% higher than the intrafilm removal threshold. Additionally, the transition from the unmixed to mixed Ni-W occurs over a narrow fluence range. It is unlikely that the diffusion length of Ni and W increases so dramatically on the nanometer length scale with only a 10% change in local fluence. Because the fluence regime for mixing is far from the regime for melting and liquid spallation that would correlate with thermally driven diffusion, other aspects of the materials response to irradiation were considered.

The material in the intrafilm removal region that was examined in STEM has conditions far from equilibrium. In Figure 4.14 trajectories are shown that represent the evolution of the temperature and density of Ni thin films after irradiation with a femtosecond pulse. While not universal, the trajectories are similar to simulations of different materials and for the near surface after irradiation of bulk materials[16, 20], for example bulk Al as shown in Figure 2.1. In Figure 4.14 the trajectories represent the cases of intrafilm and interface removal of 20 nm Ni films, these simulations are used as a guide to interpret the response of 24 nm thick multilayer Ni-W films between the intrafilm and interface removal thresholds.

Figure 4.14 shows that after irradiation the temperature of the film increases and the film melts, but remains at solid density. As the molten film expands, the density decreases and the trajectory enters the vapor dome. With increasing local fluence, the irradiated material enters the vapor dome at higher temperatures and stays within the vapor dome for a longer time. As the density of the film recovers the trajectories exit the vapor dome and approach

the liquid line. The simulation shows that the trajectory exhibits fluctuations in density and temperature as it exits the vapor dome and approaches the liquid line. Fluctuations were also observed as the material cools along the liquid line. The fluctuations in density and temperature may indicate that the state of the material is not well defined and that the interatomic interactions remain weak for a time after the material exits the vapor dome. The difference between the interface and intrafilm removal paths in Figure 4.14 is a period of cooling along the liquid line from 9000 K to 7000 K. The time spent on this segment of the liquid may be on the order of a nanosecond making the characteristics of material on the liquid line of great interest for future work. As the fluence is increased, the time spent in this series of extreme thermodynamic states increases. The trajectories penetrate further into the vapor dome and remain within the vapor dome for a longer period of time. Also the trajectory settles on and cools along the liquid line for a longer period with the accompanying fluctuations of density and temperature. It is hypothesized that for material within the vapor dome at high temperature the combination of weak interatomic interaction and high kinetic energy could increase the diffusion length and favor mixing of the Ni and W layers.

The relative importance of the extreme conditions in the vapor dome vs thermally driven diffusion in femtosecond laser mixing the Ni and W layers remains unclear. By increasing the fluence the Ni-W remains hot longer, but also the metal spends more time in the vapor dome and on the liquid line. At this point the relaxation and the increased thermally driven diffusion correlate; the two effects are not easily decoupled. In future work, samples may be created where the relaxation path goes to high temperatures without approaching the vapor dome, to limit mixing of Ni and W to diffusion, or MD modeling may be developed that capture the behavior of materials within the vapor dome or on the liquid line. At this time, it is suggested that mixing of Ni and W requires much more energy than melting and heating to even to 5000 K, and that at the fluences for mixing, significantly more time is spent entering the vapor dome and cooling along the liquid line after irradiation. After

irradiation at high fluences, the relative impact of high temperatures vs. the instability of material within the vapor dome to the process of mixing remains an open question.

In summary, multilayer Ni-W films were irradiated with a single femtosecond laser pulse and the removal craters and microstructure of the films were examined after irradiation. Multilayer Ni-W films on Ni substrates exhibit two distinct thresholds for removal after irradiation with a single pulse, similar to pure ultrathin Ni films on glass. The intrafilm and interface removal thresholds are 0.20 and 0.47 J/cm^2 respectively. HAADF STEM shows that ultrathin multilayer Ni-W films irradiated between 0.30 and 0.47 J/cm^2 formed a uniformly mixed film on the Ni substrate after irradiation. The nanocrystalline film was observed using STEM several weeks after irradiation, showing that the nanocrystalline material is thermally stable at room temperature.

Removal of the ultrathin multilayer Ni-W film was similar to removal of ultrathin Ni films. In the intrafilm removal region, material on the surface was driven far from equilibrium, but remains on the surface because the depth of liquid spallation is suppressed. Similar to ultrathin films of pure Ni, the state of material in the intrafilm removal region enters the vapor dome at higher temperatures and for longer times with increasing fluence. It is possible that the high kinetic energy and weak interaction of atoms in the vapor dome could play a role in mixing of Ni and W.

It is suggested that the nanocrystalline microstructure of the Ni-W film in the intrafilm removal region at fluences greater than 0.30 J/cm^2 results from homogeneous nucleation of the solid phase during rapid resolidification of molten Ni-W. Previous MD simulations predict that nanocrystalline material may form via rapid solidification after femtosecond laser irradiation of metals, but nanocrystalline surface layers have not previously been observed. In pure metals the nanocrystalline material is thermally unstable, and after irradiation the melted and resolidified metal is epitaxial with the unmelted bulk material. It is well known from previous studies of electrodeposited Ni-W alloys that a thermally stable nanocrystalline microstructure is formed. By using multilayer Ni-W films in this work, it is possible

that nanocrystals formed by homogeneous nucleation during rapid cooling of the irradiated film were stabilized by grain boundary segregation of W. To my knowledge this would be the first experimental observation of a nanocrystalline phase at the surface of metal formed by rapid quenching after irradiation with a single femtosecond laser pulse, as predicted by MD simulation.

Nano-crystalline alloys exhibit extraordinary mechanical and chemical properties. This chapter demonstrates a new method to create thermally stable nanocrystalline coatings with a femtosecond laser. The method for femtosecond laser mixing of multilayer metal thin films is applicable to a wide range of alloy composition. This method is promising as a route to form alloys from the liquid phase that may be difficult to produce using other methods including conventional casting or methods for rapid solidification including splat quenching or melt spinning. It is possible this method could provide an alternative to create alloys that have only been created previously using sputtering or other deposition techniques. Also, the method of irradiation of ultrathin metal films also makes it possible to study material driven to extreme conditions after femtosecond laser irradiation. Reducing the thickness of the target film to limit the volume of material removed by liquid spallation is a simple method to study materials driven into extreme states using post mortem microscopy methods including cross section TEM.

References

1. Vincenc Oboňa, J., Ocelík, V., Rao, J., Skolski, J., Römer, G., Huis in 't Veld, A. & Hosson, J. T. M. D. Modification of Cu surface with picosecond laser pulses. *Applied Surface Science* **303,** 118–124 (June 2014).
2. Shugaev, M. V., Wu, C., Armbruster, O., Naghilou, A., Brouwer, N., Ivanov, D. S., Derrien, T. J.-Y., Bulgakova, N. M., Kautek, W., Rethfeld, B. & Zhigilei, L. V. Fundamentals of ultrafast laser–material interaction. *MRS Bulletin* **41,** 960–968 (Dec. 2016).
3. *Lasers in Materials Science* (eds Castillejo, M., Ossi, P. M. & Zhigilei, L.) (Springer International Publishing, Cham, 2014).
4. Wu, C., Christensen, M. S., Savolainen, J.-M., Balling, P. & Zhigilei, L. V. Generation of subsurface voids and a nanocrystalline surface layer in femtosecond laser irradiation of a single-crystal Ag target. *Physical Review B* **91** (Jan. 12, 2015).
5. Ivanov, D. S., Lin, Z., Rethfeld, B., O'Connor, G. M., Glynn, T. J. & Zhigilei, L. V. Nanocrystalline structure of nanobump generated by localized photoexcitation of metal film. *Journal of Applied Physics* **107,** 013519 (2010).
6. Weissmüller, J. Alloy effects in nanostructures. *Nanostructured Materials. Proceedings of the First International Conference on Nanostructured Materials* **3,** 261–272 (Jan. 1, 1993).
7. Detor, A. J., Miller, M. K. & Schuh, C. A. Solute distribution in nanocrystalline Ni-W alloys examined through atom probe tomography. *Philosophical Magazine* **86,** 4459–4475 (Oct. 1, 2006).
8. Chookajorn, T., Murdoch, H. A. & Schuh, C. A. Design of Stable Nanocrystalline Alloys. *Science* **337,** 951–954 (Aug. 24, 2012).
9. Chase, Malcolm W. NIST-JANAF Thermochemcal Tables. *Journal of Physical and Chemical Reference Data* **Monograph No. 9,** 1–1951 (1998).
10. Hirata, A., Morino, T., Hirotsu, Y., Itoh, K. & Fukunaga, T. Local atomic structure analysis of Zr-Ni and Zr-Cu metallic glasses using electron diffraction. *Materials transactions* **48,** 1299–1303 (2007).
11. Hirata, A., Hirotsu, Y., Ohkubo, T., Hanada, T. & Bengus, V. Z. Compositional dependence of local atomic structures in amorphous Fe 100 = x B x (x = 14 , 17 , 20) alloys studied by electron diffraction and high-resolution electron microscopy. *Physical Review B* **74,** 214206 (Dec. 29, 2006).
12. Hirata, A., Hirotsu, Y., Matsubara, E., Ohkubo, T. & Hono, K. Mechanism of nanocrystalline microstructure formation in amorphous Fe = Nb = B alloys. *Physical Review B* **74** (Nov. 15, 2006).

13. Hirotsu, Y., Uehara, M. & Ueno, M. Microcrystalline domains in amorphous Pd $_{77.5}$ Cu $_{6}$ Si $_{16.5}$ alloys studied by high-resolution electron microscopy. *Journal of Applied Physics* **59,** 3081–3086 (May 1986).

14. Detor, A. & Schuh, C. Tailoring and patterning the grain size of nanocrystalline alloys. *Acta Materialia* **55,** 371–379 (Jan. 2007).

15. Natter, H., Schmelzer, M. & Hempelmann, R. Nanocrystalline nickel and nickel-copper alloys: Synthesis, characterization, and thermal stability. *Journal of Materials Research* **13,** 1186–1197 (May 1998).

16. Povarnitsyn, M. E., Itina, T. E., Sentis, M., Khishchenko, K. V. & Levashov, P. R. Material decomposition mechanisms in femtosecond laser interactions with metals. *Physical Review B* **75,** 235414 (June 2007).

17. Sedao, X., Shugaev, M. V., Wu, C., Douillard, T., Esnouf, C., Maurice, C., Reynaud, S., Pigeon, F., Garrelie, F., Zhigilei, L. V. & Colombier, J.-P. Growth Twinning and Generation of High-Frequency Surface Nanostructures in Ultrafast Laser-Induced Transient Melting and Resolidification. *ACS Nano* **10,** 6995–7007 (July 26, 2016).

18. Leonard, J. P., Renk, T. J., Thompson, M. O. & Aziz, M. J. Solute diffusion in liquid nickel measured by pulsed ion beam melting. *Metallurgical and Materials Transactions A* **35,** 2803–2807 (2004).

19. Meyer, A. The measurement of self-diffusion coefficients in liquid metals with quasielastic neutron scattering. *EPJ Web of Conferences* **83** (eds Frick, B., Koza, M. M., Boehm, M. & Mutka, H.) 01002 (2015).

20. Lorazo, P., Lewis, L. & Meunier, M. Thermodynamic pathways to melting, ablation, and solidification in absorbing solids under pulsed laser irradiation. *Physical Review B* **73,** 134108 (Apr. 2006).

CHAPTER 6

Femtosecond Laser Mixing of Immiscible Alloys

The method of femtosecond laser mixing of multilayer materials was investigated in the previous chapter using the Ni-W system. It was shown that simply melting and quenching the multilayer Ni-W film was insufficient to mix the Ni and W layers. Hydrodynamic simulations of pure Ni films were used to gain insight into the effect of irradiation near the interface removal threshold of Ni-W films. After irradiation, the target material is melted and then driven into the vapor dome in the temperature-density single component phase diagram, as shown in Figure 4.14. With increasing fluence the liquid enters the vapor dome at higher temperatures and for longer periods of time. It was hypothesized that the weak interatomic interaction and high kinetic energy of atoms while inside and while exiting the vapor dome are favorable for mixing of strongly segregating alloys, possibly beyond their equilibrium solubility. This chapter extends that hypothesis to the immiscible Ni-Ag system.

Ni and Ag are immiscible at equilibrium in the solid and liquid phases for a broad range of compositions and temperatures[1]. The phase diagram includes a broad monotectic. Above the monotectic temperature there is a miscibility gap in the liquid phase, where the liquid separates forming Ni rich and Ag rich phases. In this chapter, multilayer Ni-Ag films with a composition of 50%Ag were irradiated. This composition was selected because it is near the peak of the miscibility gap and also the maximum enthalpy of mixing for liquid Ni and Ag[2, 3]. This composition represented the quintessential case of an immiscible alloy,

and the most difficult conditions for femtosecond laser driven mixing. The microstructure and composition of the layer were examined after irradiation using STEM.

6.1 Damage Thresholds of Multilayer Ni-Ag Films

Multilayer Ni-Ag films were prepared by depositing 12 alternating layers of 2.1 nm Ag and 1.4 nm Ni on a substrate. The composition of the film is 50 at% Ag. The top layer was Ag, at the free surface. The substrate consisted of 80 nm Ni, serving as a heat sink, 300 nm SiO_2 as a diffusion barrier to prevent Ni silicide formation, and a 500 μm thick Si support.

Multilayer Ni-Ag films were irradiated in air with a single pulse. Above a local fluence of 0.11 J/cm^2, pinholes are observed in the Ni-Ag film, penetrating to the surface of the Ni substrate. The original layers of Ni and Ag remain intact up to a local fluence of 0.15 J/cm^2. Removal at the interface occurs above a threshold fluence of 0.17 J/cm^2. AFM of the damage crater is shown in Figure 6.1. The edges of the interface removal region are not well defined, unlike the edge of the interface removal crater of multilayer Ni-W films in Figure 5.2. Near the edge of the interface removal crater the Ni-Ag film appears to be much thicker than the as-deposited film and also exhibits holes down to the Ni substrate surface. The structure Ni-Ag film close to the removal edge indicates the film melted and dewetted from the Ni substrate after irradiation. STEM images in Figure 6.1 of the NiAg film near the edge of the interface removal crater show that within the droplets the Ni and Ag are not mixed. The Ni substrate does not exhibit removal or significant damage near the threshold for removal of the multilayer Ni-Ag film.

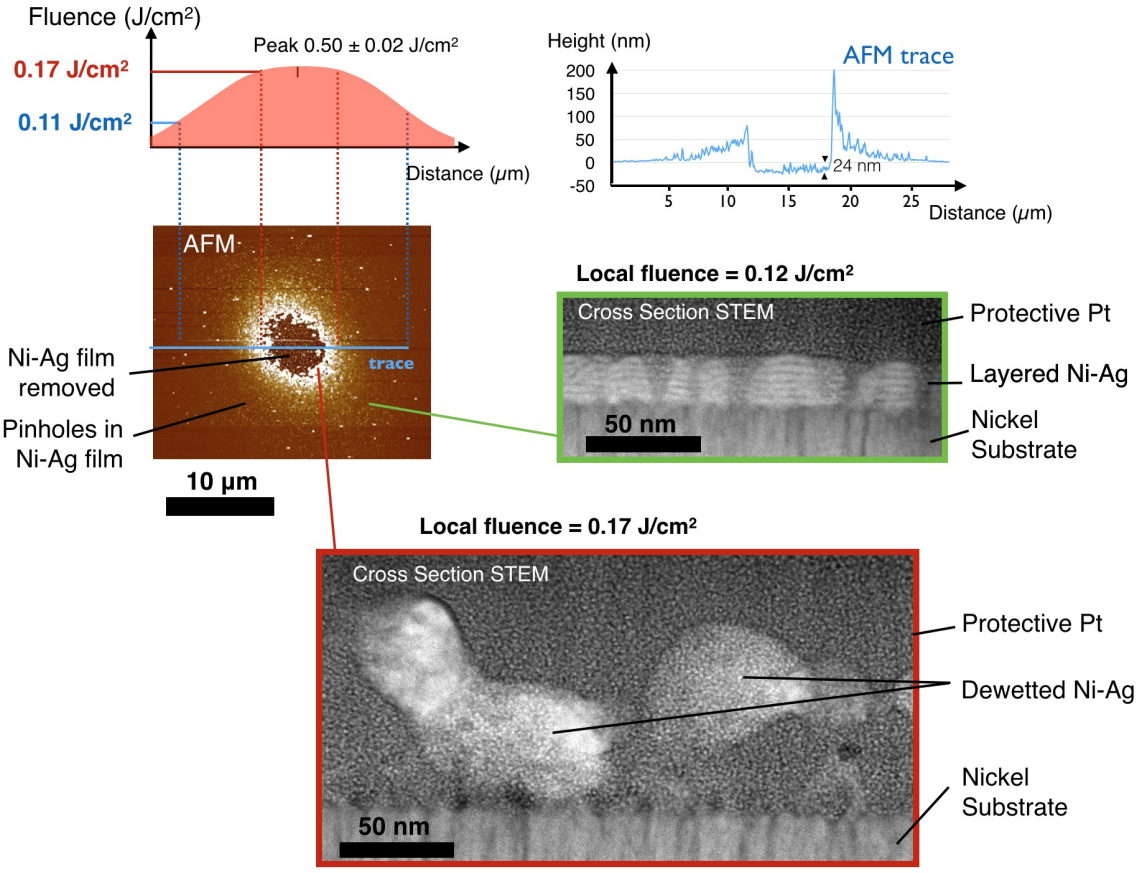

Figure 6.1: Removal crater and microstructure of 24 nm thick multilayer Ni-Ag film on Ni substrate after irradiation. Only interface removal is observed near the damage threshold of multilayer Ni-Ag films. Pinholes are formed in the Ni-Ag film at 0.12 J/cm^2, but the layered structure remains intact observed using HAADF STEM. At the edge of the interface removal crater the Ni-Ag film dewets forming droplets thicker than the original layer. Within the droplets, the as-deposited layered structure of Ni and Ag is not observed in HAADF STEM images. Bright and dark patches indicate separate regions of Ni and Ag.

6.2 Femtosecond Laser Mixing of Ni-Ag via Tamped Irradiation

Because the threshold fluence for removal at the interface between the multilayer Ni-Ag film and the Ni substrate was 0.17 J/cm^2, it was impossible to know the effect of irradiation on the multilayer Ni-Ag film at local fluences comparable to interface removal of pure Ni films or at the threshold for mixing multilayer Ni-W films. To ensure Ni-Ag films irradiated at higher fluences remained on the substrate surface for post mortem characterization, a tamping layer of SiO_2 glass 1.5 microns thick was deposited on the surface of the Ni-Ag film using Plasma Enhanced CVD.

After irradiation, the glass layer separated from the substrate above a local fluence of 0.20 J/cm^2, forming a blister. Figure 6.2a shows an SEM image of a blister formed after irradiation with a peak fluence of 0.4 J/cm^2. 50% of the blisters broke after irradiation with a peak fluence of 0.7 J/cm^2. Spots irradiated with a peak fluence of 0.4 J/cm^2 were examined in cross section STEM. Layers of Ni and Ag were distinguishable after irradiation with a local fluence of 0.15 J/cm^2, shown in Figure 6.2c. At a local fluence of 0.36 J/cm^2 the as-deposited layers of Ni and Ag are not observed. Figure 6.2d shows that the Ni-Ag film exhibits a single grain with multiple twin boundaries. The lattice parameter of the grain corresponds to Ag. In Figure 6.2d, the twin grains are viewed down the [110] zone axis, the black line marks (111) planes crossing twin boundaries sharing a (111) boundary plane with an angle of 70.5 degrees rotation around the [110] direction.

Energy-dispersive X-ray Spectroscopy (EDS) maps showing the distribution of Ni and Ag after irradiation with a local fluence of 0.17 J/cm^2 are shown in Figure 6.3. The EDS maps confirm that voids were created in the Ni substrate as previously shown in Figure 6.2. The voids that appear in the Ni substrate are believed to result from cavitation, identical to the voids that form during liquid spallation except that the tamping layer confines the top layer and prevents removal. The EDS maps also show that the Ag remains in a distinct

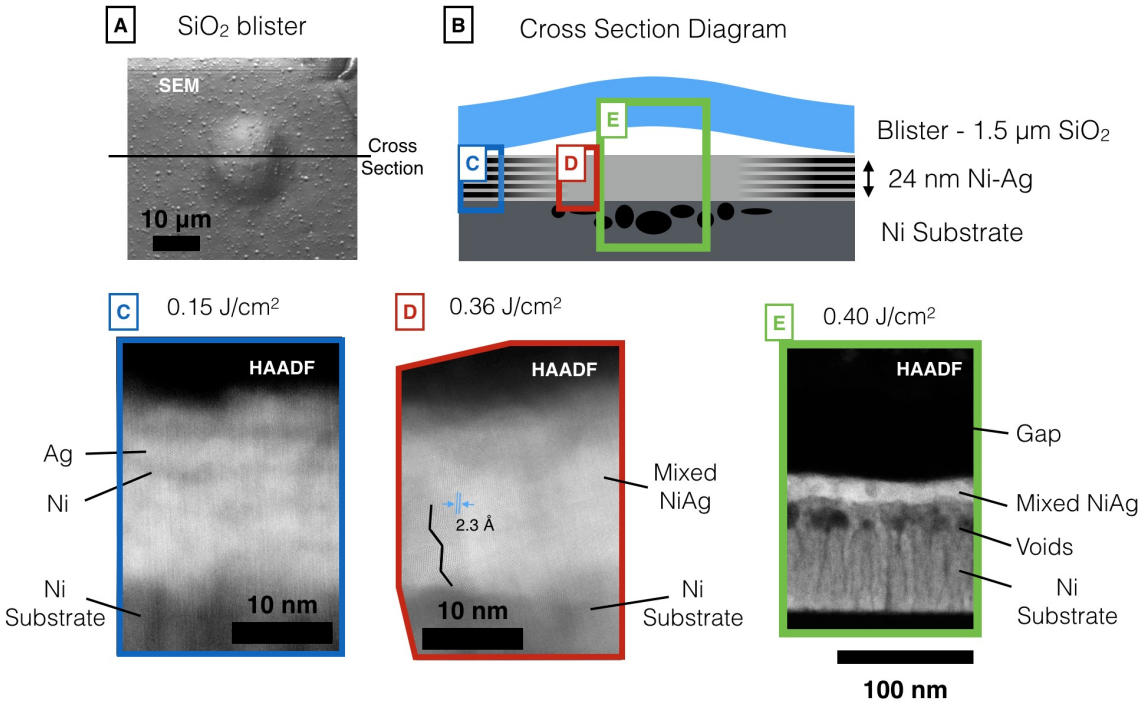

Figure 6.2: Cross section STEM of 24 nm thick multilayer Ni-Ag film after irradiated with an 1.5 μm thick glass tamping layer. A glass tamper was deposited on the multilayer Ni-Ag film. The multilayer Ni-Ag film was irradiated through the glass with a peak fluence of 0.4 J/cm^2. The SEM image shows the formation of a blister when the glass layer separated from the Ni-Ag film above a local fluence of 0.2 J/cm^2. At 0.15 J/cm^2 separate Ni and Ag layers are observed, although the images do not rule out the possibility that some mixing has occurred. At 0.36 J/cm^2 a single crystal with multiple twins and the lattice constant of silver is observed. At 0.40 J/cm^2 voids form in the Ni substrate 40 nm below the tamper.

layer at the surface of the substrate with the approximate thickness of the as-deposited multilayer Ni-Ag film. When comparing the maps of Ni and Ag it is possible to distinguish areas where the concentrations invert. The combination of distinct grains of Ni and Ag in HR STEM and phase separation in the EDS maps indicate that the Ni and Ag phase separate after irradiation.

After irradiation the glass tamping layer separates from the Ni-Ag film and voids form in the Ni substrate close to the Ni-Ag film; both factors severely limit heat transport out of the Ni-Ag film. Without rapid quenching the Ni-Ag remains hot longer, potentially allowing the phase separation of the Ni and Ag. In an ideal experiment the Ni-Ag film

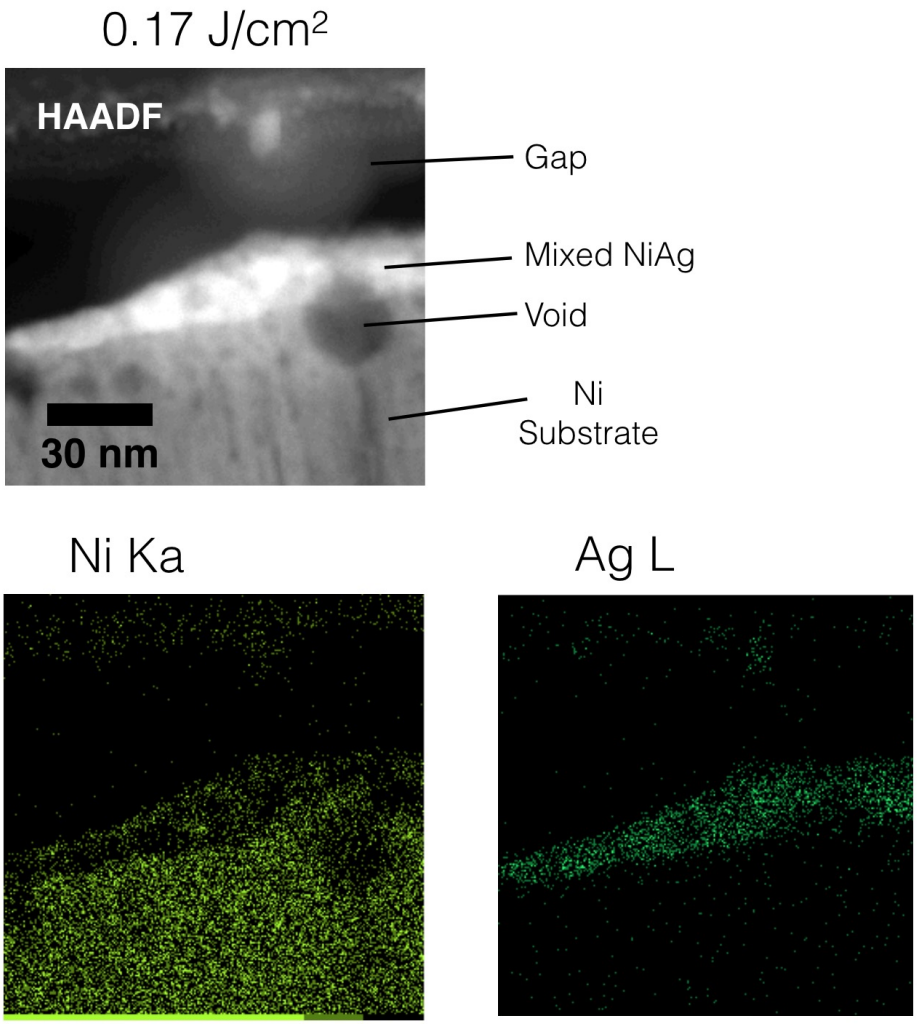

Figure 6.3: Cross section STEM and EDS element mapping after irradiation of 24 nm thick multilayer Ni-Ag films with an 1.5 μm glass tamping layer. EDS mapping confirms that the bright region near the surface of the Ni substrate corresponds to the Ni-Ag film. In some regions of the Ni-Ag film it is apparent that the Ni and Ag signal are inverted, indicating that the Ni and Ag phase separated.

would remain in thermal contact with the tamping layer and voids would not be formed. To achieve that, the deposited SiO_2 tamping layer was exchanged for a sapphire tamping layer because the acoustic impedance of sapphire is much closer to the impedance of Ni and Ag, compared with SiO_2. With a smaller impedance mismatch between the irradiated surface and the tamper, the high pressure in the irradiated material will be transmitted into the tamping layer. It was believed that if the compressive stress were allowed to dissipate into both the tamper and the substrate, the intensity of the unloading tensile wave would be reduced, preventing the formation of voids via cavitation.

Multilayer Ni-Ag films were sputter deposited in 12 alternating layers of 1.6 nm Ag and 1.1 nm Ni on the 500 μm thick sapphire wafer. The composition of the film was 50 at% Ag. Ag composed the layer at the sapphire interface. The 1.5 μm thick Ni substrate layer was sputtered on the multilayer Ni-A film. The multilayer Ni-Ag film was irradiated through the sapphire tamper. After irradiation, the sapphire did not exhibit any increased roughness, glass formation, or other signs of laser induced damage.

After irradiation the Ni-Ag film contains clearly distinguishable layers of Ni and Ag at a local fluence of 0.18 J/cm^2, shown in Figure 6.4. In the unmixed layer at 0.18 J/cm^2 individual grains of Ag are distinguishable, but grains of Ni were not positively identified. At a local fluence of 0.24 the as-deposited layers of Ni and Ag are no longer observed. At a local fluence of 0.32 J/cm^2, voids start forming in the Ni-Ag film. With increasing fluence the voids split the Ni-Ag film and the Ni substrate layer forms a blister. At the peak fluence of 0.41 J/cm^2 the Ni substrate and the sapphire tamper are separated by 200 nm.

The grains of the Ni substrate grew with the (111) plane normal to the film. In Figure 6.5 the FFT of a BF STEM image of the mixed layer irradiated with a local fluence of 0.32 indicate that there are individual domains of Ni and Ag aligned with one another and with the Ni substrate. An FFT of the BF STEM image was calculated using ImageJ and shows shows a [110] zone axis with the (111) planes oriented with the (111) plane of the Ni substrate. Separate signals exist for the Ni and Ag lattice parameters in the same

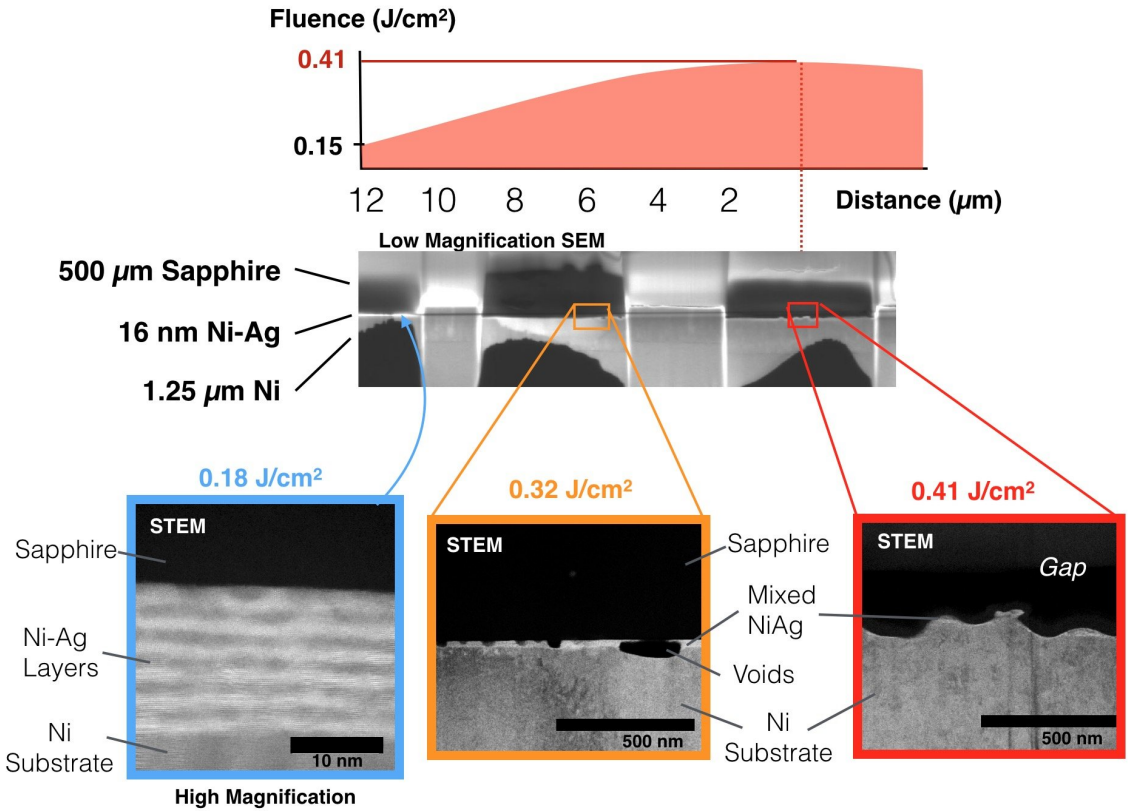

Figure 6.4: Cross section STEM of 16 nm thick multilayer Ni-Ag film after irradiated with an sapphire tamping layer. The Ni-Ag film was irradiated through a sapphire tamper. The as-deposited layers of Ni and Ag are not observed after irradiation above a local fluence of 0.24 J/cm^2. Voids form in the Ni-Ag film above a local fluence of 0.32 J/cm^2, with increasing fluence the voids grow larger splitting the Ni-Ag film and forming a 200 nm gap between the substrate and tamper.

orientation. The Ni and Ag domains are aligned epitaxially with each other and the Ni substrate. Fourier filters surrounding the Ni and Ag spots in the FFT were used to isolate the domains of each species highlighting the planes and columns of atoms in the BF STEM image corresponding to Ni and Ag respectively. The filtered images show the species phase separated. A Ni twin grain appears in the FFT and in the filtered Ni image.

Another multilayer Ni-Ag film was prepared consisting of 12 alternating layers of 5.7 nm Ag and 3.3 nm Ni on the 1.5 μm thick Ni substrate and with the sapphire tamper. This multilayer Ni-Ag film is significantly thicker. Figure 6.6 shows the multilayer Ni-Ag film after irradiation with a peak fluence of 0.47 J/cm^2. At a local fluence of 0.29 J/cm^2 the

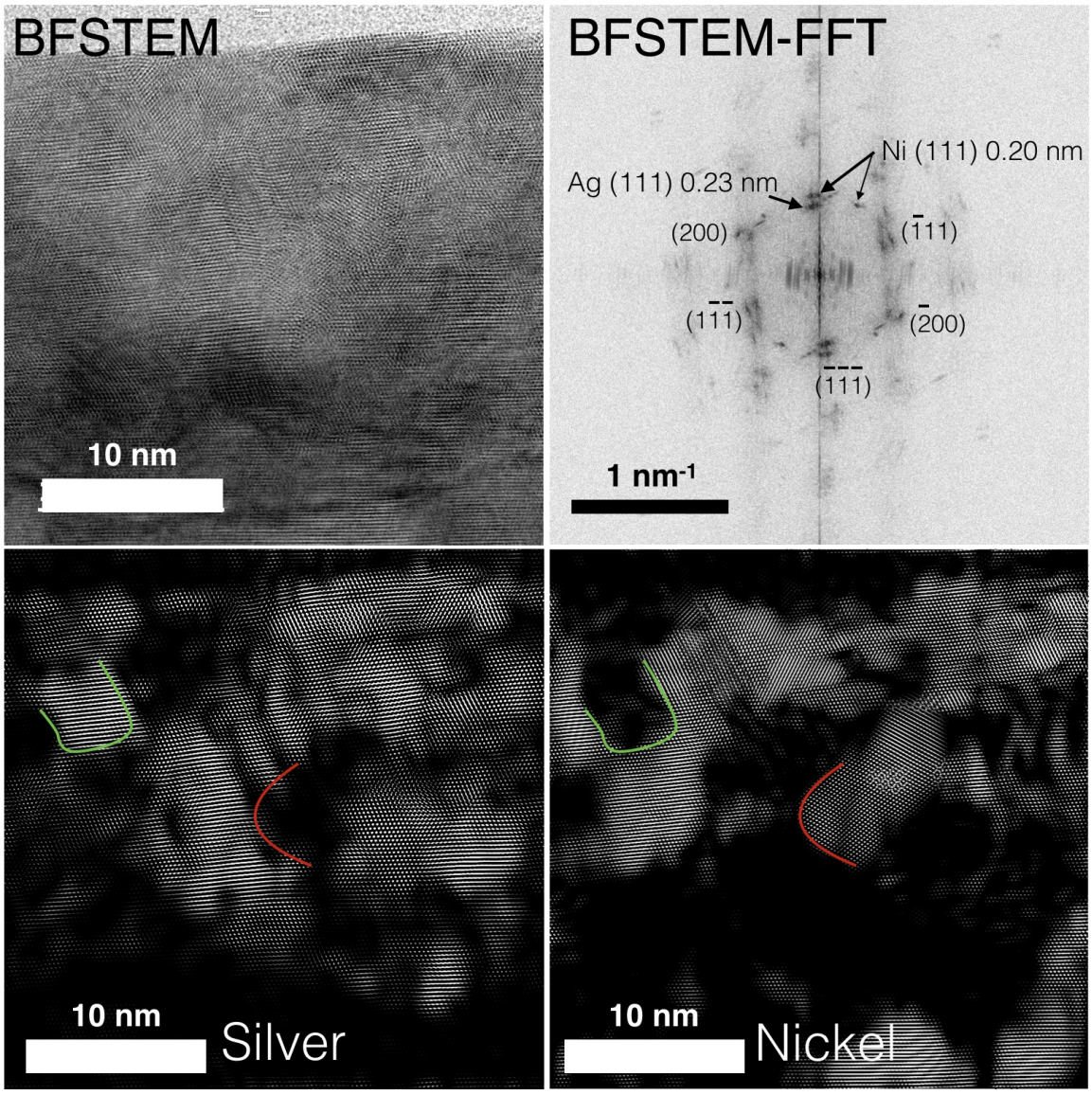

Figure 6.5: Cross section BFSTEM image of 16 nm thick multilayer Ni-Ag film after irradiation through sapphire tamping layer and FFT filtering to show separate domains of Ni and Ag. BF STEM shows that the as-deposited layers of Ni and Ag are not observed after irradiation with a local fluence of 0.32 J/cm^2. An FFT of the BF STEM image shows separate signals for the Ni and Ag lattice parameters. The FFT also shows that the Ni and Ag domains are aligned with each other and the Ni substrate. Fourier filters surrounding the Ni and Ag frequencies in the FFT were used to isolate the location of each species. Filtered images showing the lattice contrast corresponding to the Ni and Ag frequencies in the FFT are shown. The periodic contrast in each filtered image indicates the location of planes and columns of atoms. Lines are drawn at selected edges of the Ni and Ag regions showing the phase inverts.

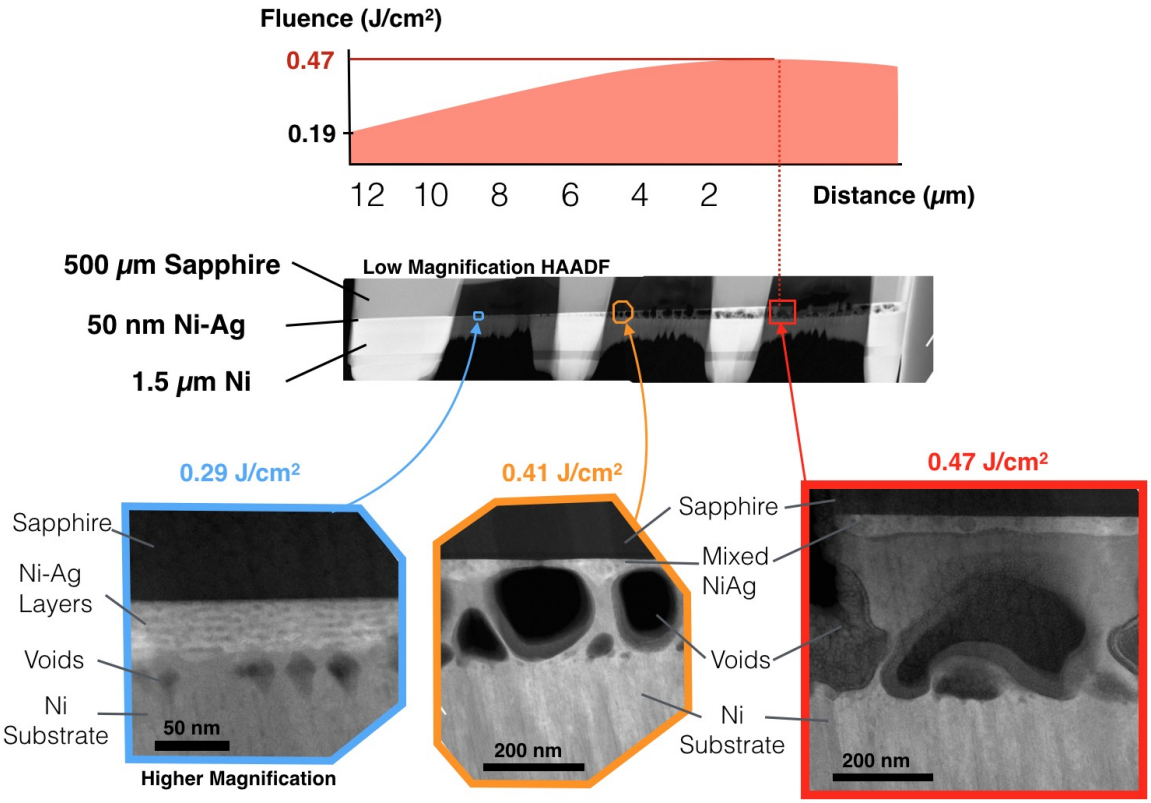

Figure 6.6: Cross section STEM image of 50 nm thick multilayer Ni-Ag film after irradiation with Sapphire tamper. The Ni-Ag film was irradiated through the sapphire tamper. The as-deposited layers of Ni and Ag are not distinguishable after irradiation above a local fluence of 0.35 J/cm^2. Voids form in the Ni substrate above a local fluence of 0.29 J/cm^2 indicating the Ni-Ag film and the top of the Ni substrate melted but the as-deposited layers of Ni and Ag did not mix and remain distinguishable. With increasing fluence the voids grow larger and form deeper in the substrate.

as-deposited layers of Ni and Ag remain distinguishable. Voids are observed in the Ni substrate close to the Ni-Ag film. The presence of voids indicates that the film melted well into the Ni substrate layer, that the tensile wave caused the formation of voids similar to liquid spallation but removal was prevented due to the tamper, and the film resolidified but maintained the layered structure of the original film. This could indicate that the film was liquid but for too short a time and/or at too low of temperature for diffusion to mix the Ni and Ag layers.

HAADF STEM in Figure 6.6 shows the as-deposited layers of Ni and Ag in the Ni-Ag

film are no longer observed after irradiation at a local fluence of 0.41 J/cm^2. However, the Ni-Ag film does not exhibit uniform contrast, suggesting the Ni and Ag phase separated similar to previous samples. With increasing fluence the voids increase in diameter and appear deeper in the Ni substrate. It is likely that with increasing fluence a greater thickness of the Ni substrate is melted and the maximum tensile stress develops at a greater depth. The Ni-Ag is not uniform in thickness after irradiation, but is drawn into the walls between the voids. It appears that as the voids expand material is drawn around them; the Ni-Ag is pulled into the walls between the voids as the liquid stretches between the substrate and tamper.

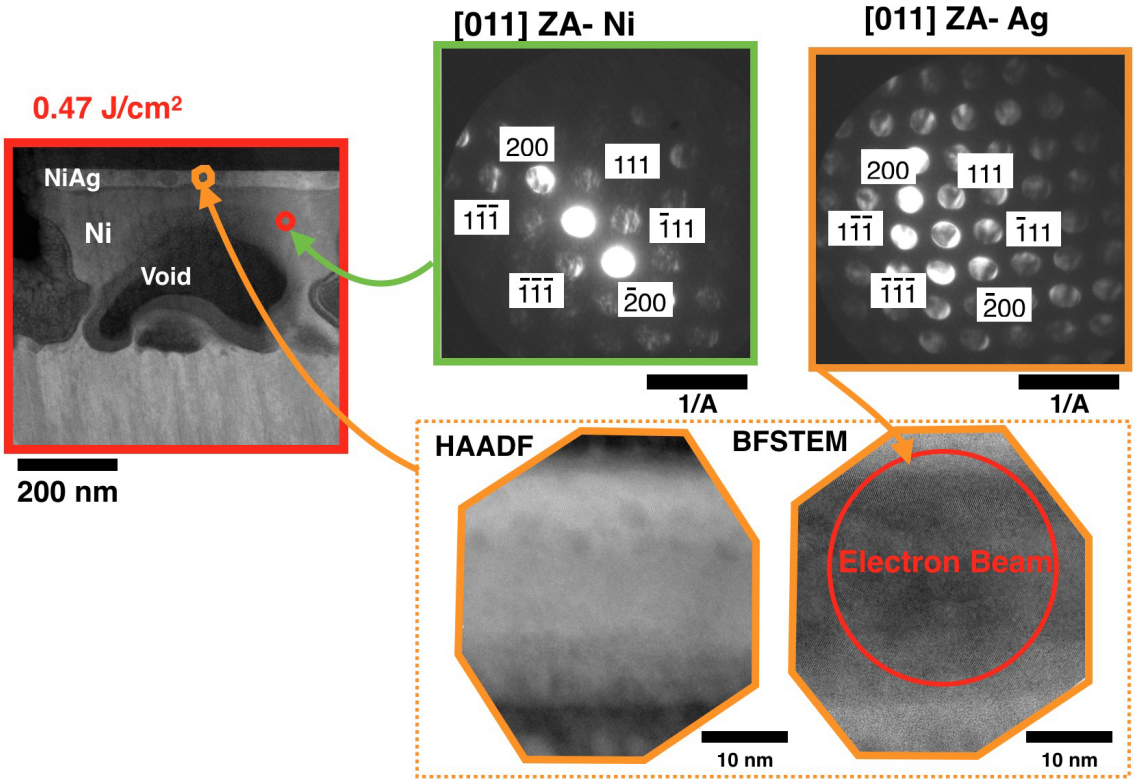

Figure 6.7: Cross section STEM and NBED of 50 nm thick multilayer Ni-Ag film after irradiation with sapphire tamper. NBED patterns of an 50 nm thick multilayer Ni-Ag film and the underlying Ni substrate were collected after irradiation with a local fluence of 0.47 J/cm^2. The Ni substrate and the Ni-Ag film resolidified epitaxially. The diffraction pattern in the Ni-Ag film corresponds to Ag. HAADF STEM shows some non-uniformity in the Ni-Ag film. BF STEM shows there is a large twinned grain that spans the Ni-Ag film.

Nano-beam Electron Diffraction (NBED) of the irradiated Ni-Ag film and the Ni substrate was performed after irradiation at a local fluence of 0.47 J/cm^2. In the Ni-Ag film a single crystal diffraction pattern with the lattice parameter of silver was gathered. It is apparent that the sample was melted well into the Ni substrate. A NBED pattern was collected from the resolidified Ni substrate above the voids. The silver grain in the Ni-Ag film is aligned with the Ni substrate with the (111) plane normal to the interface with the sapphire tamper.

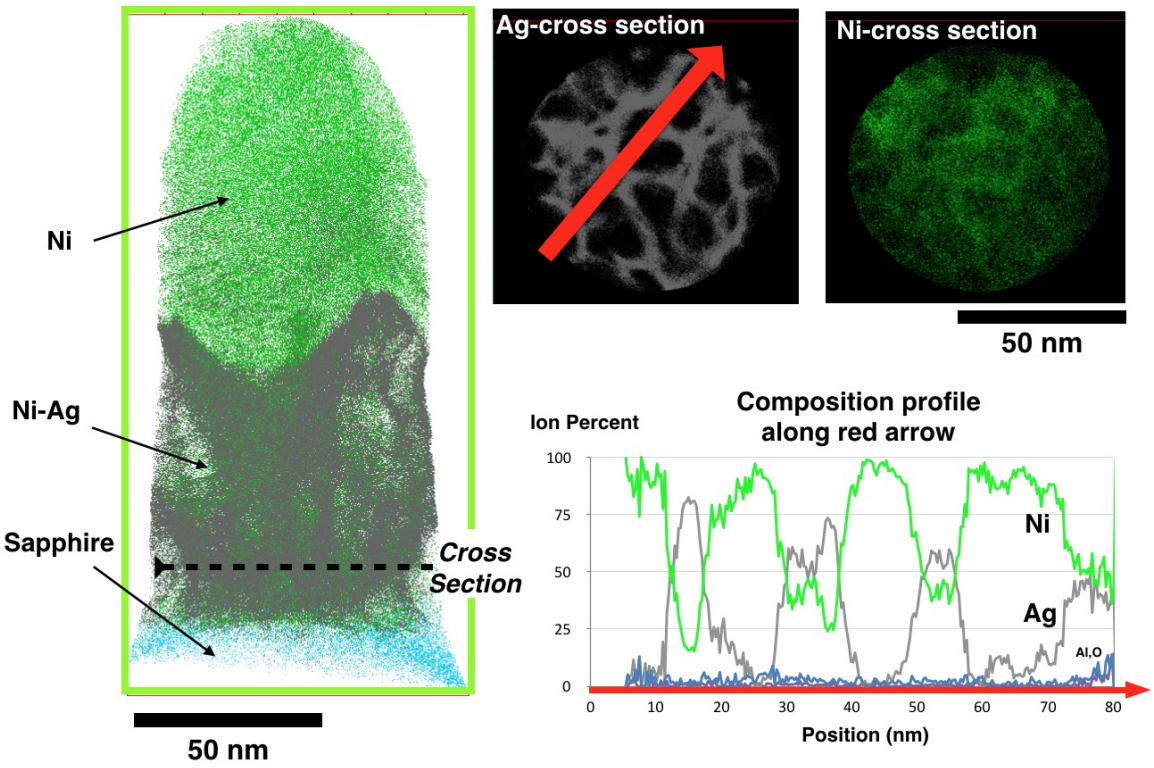

Figure 6.8: Atom Probe Tomography of 50 nm thick multilayer Ni-Ag film after irradiation with sapphire tamper. The Ni-Ag film was irradiated through the sapphire tamper with a local fluence of 0.40 J/cm^2. Atom probe at high fluence was possible in this sample because the voids formed deep in the Ni substrate. It is apparent that the Ag is collected in discrete regions.

Because the voids form deep in the Ni substrate after irradiation at high fluences it was possible to examine the Ni-Ag film using Atom Probe Tomography (APT). Figure 6.8 shows the APT reconstruction of a 50 nm thick multilayer Ni-Ag film after irradiation with

a local fluence of 0.40 J/cm^2. The tips for atom probe were prepared upside down; the Ni substrate was the top layer of the tip and the sapphire tamper was the bottom, as shown in Figure 6.8. Preliminary APT shows that the Ni and Ag are at least partially phase separated with distinct domains of Ni and Ag in the sample volume. The concentration profile of Ni and Ag show that the concentration of Ag switches between approximately 50% and 0%. The Ni trace follows the precise inverse. The ion counts are nearly three times higher in the silver domains. The Ni counts do not vary extremely along the path of the concentration profile in Figure 6.8. As the Ag counts increase in the profile the Ni counts do not change as drastically; the total number of counts goes up and the relative fraction of Ni counts goes down. The number of counts in the Ag region are anomalously high.

The diffuse distribution of Ni atoms and the sharp distribution of Ag atoms could result from the much lower evaporation field Ag relative to Ni. As the surface of the Ni-Ag film evaporates the Ag layer will erode much faster[4–6]. The faster evaporating Ag grain could form a crater in the Ni-Ag specimen surface and cause the trajectories of Ag ions to converge, making the Ag domain appear smaller on the detector. Conversely the slower evaporating Ni could form a bump on the specimen surface, causing the trajectories to diverge. As a result in the reconstructed sample the Ni appears to spread out uniformly and the Ag appears in unrealistically small domains with a density at least two times higher than its actual density. The results of APT show that the Ni and Ag are not uniformly mixed and exist in separate domains, corroborating the observations of HAADF STEM where Z contrast and Fourier filtered BF STEM images showed that the Ni and Ag were phase separated. The nonuniform distribution of density in the reconstruction also indicates that thought Ni and Ag is a model immiscible system, it is not a prudent choice for future work if APT will be used for post mortem characterization.

In summary, the method developed in Chapter 6 to mix multilayer Ni-W films was extended to the Ni-Ag system; Ni-Ag is a model system of immiscible metals with a large positive enthalpy of mixing. It was hypothesized that the conditions inside the vapor dome

after irradiation with sufficiently high fluence, where the atomic interactions are weak and the kinetic energy of atoms is high, would be favorable for mixing of strongly segregating alloys.

Intrafilm removal was not observed in multilayer Ni-Ag films on Ni substrates. The interface removal threshold of 24 nm thick Ni-Ag films is 0.17 J/cm^2. At the edge of the removal crater the Ni-Ag film partially dewets on the surface of the Ni substrate. The resolidified droplets at the interface removal threshold consist of separate nanoscale grains of Ni and Ag. To retain Ni-Ag irradiated at higher fluence, e.g. the fluence range for mixing of Ni-W, SiO_2 and Al_2O_3 tampers were added.

The as-deposited layers of Ni and Ag remain distinguishable after tamped irradiation of multilayer Ni-Ag films below a local fluence of 0.28 J/cm^2. The formation of voids shows that the irradiated film melted and resolidified. Tamped irradiation of multilayer Ni-Ag films above local fluence of 0.34 J/cm^2 results in the elimination of the as-deposited Ni and Ag layers. HR STEM and NBED show that the Ni-Ag film resolidifies epitaxially with the Ni substrate, oriented with the (111) plane normal to the tamping layer. EDS mapping, APT, and HR STEM indicate that Ni and Ag rich regions are formed after irradiation, not a uniform mixture.

Instead of a microstructure that is amorphous[7, 8] or an FCC solid solution[9], as seen in previous Ni-Ag alloys created using physical vapor deposition methods, the Ni-Ag film appears to be a mixture of epitaxially matched FCC Ni and FCC Ag domains, possibly making up a single crystal. In some HR STEM images the surface layer exhibits a single grain that crosses the Ni-Ag film with multiple twin boundaries. The epitaxial resolidification of a metal with a large concentration of twin boundaries has been previously observed in rapid solidification of single component metals irradiated with a femtosecond pulse. It is possible that the Ni-Ag film did not form randomly oriented nanoscale grains, as might occur in Ni-W films, or an amorphous microstructure because of the high enthalpy of mixing of Ni and Ag. If the Ni-Ag forms an uniform mixture after irradiation, the heat

of mixing will be rejected as the film cools and begins to phase separate[7]. The heat rejected by Ni and Ag segregation could slow the cooling rate enough to prevent freezing of the mixed microstructure. It is apparent that either a uniform melt of Ni-Ag was never formed, seemingly unlikely because of the extremely high temperature of the melt, or that resolidification was not fast enough to prevent phase separation of Ni and Ag. Future work should attempt to controlling the cooling rate of Ni-Ag alloys to achieve a uniform composition and experiments with other immiscible alloy compositions.

References

1. Singleton, M. & Nash, P. The Ag- Ni (Silver-Nickel) system. *Journal of Phase Equilibria* **8,** 119–121 (1987).
2. Liu, X. J., Gao, F., Wang, C. P. & Ishida, K. Thermodynamic Assessments of the Ag-Ni Binary and Ag-Cu-Ni Ternary Systems. *Journal of Electronic Materials* **37,** 210–217 (Feb. 2008).
3. Saeed, U., Flandorfer, H. & Ipser, H. Lead-free solders: Enthalpies of mixing of liquid alloys in the Ag–Ni and Ag–Ni–Sn systems. *Journal of Materials Research* **21,** 1294–1304 (May 2006).
4. Vurpillot, F. in *Atom Probe Tomography* 183–249 (Elsevier, 2016).
5. Marquis, E. A. & Hyde, J. M. Applications of atom-probe tomography to the characterisation of solute behaviours. *Materials Science and Engineering: R: Reports* **69,** 37–62 (July 20, 2010).
6. Larson, D., Gault, B., Geiser, B., De Geuser, F. & Vurpillot, F. Atom probe tomography spatial reconstruction: Status and directions. *Current Opinion in Solid State and Materials Science* **17,** 236–247 (Oct. 2013).
7. Ma, E. Alloys created between immiscible elements. *Progress in Materials Science* **50,** 413–509 (May 2005).
8. He, J. H., Sheng, H. W., Schilling, P. J., Chien, C.-L. & Ma, E. Amorphous Structures in the Immiscible Ag-Ni System. *Physical Review Letters* **86,** 2826–2829 (Mar. 26, 2001).
9. Van Ingen, R. P., Fastenau, R. H. J. & Mittemeijer, E. J. Formation of crystalline Ag x Ni 1- x solid solutions of unusually high supersaturation by laser ablation deposition. *Physical Review Letters* **72,** 3116–3119 (1994).

CHAPTER 7

Femtosecond Laser Enhanced Carbon Nanotube Growth

It is vital to many proposed applications of CNTs, for example fibers that have the exceptional strength and conductivity of individual CNTs, that a method is discovered to grow aligned forests of CNTs of indefinite length [1]. While CNTs up to half a meter long have been grown using floating catalyst [2], aligned CNT forests exhibit rapid termination on the order of centimeters[3–5]. Most research to increase the terminal length of CNT forests aims to extend the lifetime of the catalyst by optimizing static growth parameters such as: modifying the atmosphere, pressure, and temperature, changing the composition, size, and distribution of catalyst nanoparticles, changing the support material, or introducing a plasma[6, 7]. The objective of this chapter was to observe the effect of femtosecond laser irradiation on the nucleation and growth of CNTs, and determine the mechanisms for laser modification in terms of the dynamic process of nucleation and growth during CVD.

Irradiation of the carbon nanotube catalyst with a single femtosecond laser pulse during CVD growth increases the area density of CNTs. Increasing the area density can cause a transition from CNT growth in a disorganized mat to an aligned forest. Irradiation can also increase the terminal length of aligned forests by several orders of magnitude. Laser stimulated CNT growth depended on having carbon nanotubes present at the time of irradiation. In-situ optical microscopy and ex-situ SEM showed that some CNTs are removed after irradiation. The mechanism for laser stimulated nucleation of CNTs is not known, but it

is reasonable that irradiation heated the catalyst and, by breaking down carbon nanotubes, produced an atmosphere rich in carbon creating conditions ideal for nucleation. Because carbon nanotubes must be present on the surface at the time of irradiation, laser enhanced growth is dependent on the dynamics of nucleation and growth of nanotubes via CVD synthesis. The short lived effects of irradiation impact CVD growth of CNTs over a much longer period. This method is described as a combination of the CVD and PLV methods for carbon nanotube synthesis.

The growth conditions used in this work were not optimal: without irradiation CNTs ranged from an entangled mat that did not self-organize to an aligned forest no more than 25 μm in length. CNT nucleation and growth has a complicated dependence on many parameters[8] which could not be strictly controlled in these experiments. The result is that each time the reactor is run in a series of experiments, the growth of CNTs will vary slightly and two sets of experiments separated by a long period of time vary significantly, mostly causing variation in the yield of CNTs. The core results of femtosecond laser enhanced CVD, such as the threshold fluence for enhanced growth and the effect of delaying irradiation relative to the start of growth, are similar in each experiment.

7.1 Femtosecond laser irradiation alone does not drive CNT growth

In previous work an Nd:YAG laser system with a variable pulse width from 0.5 to 50 ms was used as the sole energy source for CVD [9]. Using the same catalyst and substrate as in this chapter, it was found that a single pulse or train of pulses must heat the catalyst above the growth temperature (in that work 900 °C) for at least 0.1 sec to allow for nucleation of CNTs. Femtosecond laser pulses heat materials for times on the order of tens of nanoseconds; with a maximum pulse repetition rate of 1000Hz the laser used in this work cannot be used to maintain the catalyst at high temperature for CVD growth.

It was found that femtosecond laser irradiation alone cannot be used to produce CNTs. Catalyst was annealed at 750 °C, identical to the standard recipe, then exposed to the carbon carrying gas acetylene and irradiated at 1000 Hz with peak fluences between 0.01 and 0.2 J/cm^2. No CNTs were observed after irradiation in SEM.

It was also found that ultrafast laser irradiation in combination with substrate heating could not promote CNT growth if the substrate temperature was below 700 °C, the minimum temperature for CVD growth in this system. Catalyst was annealed at 750 °C, identical to the standard recipe, then exposed to the carbon carrying gas acetylene at 600 °C, just below the minimum temperature for growth observed in this system. SEM showed no CNT growth occurred on pristine catalyst, after irradiation with a single pulse with a peak fluence of 0.3 J/cm^2, or after irradiation with multiple pulses including 50 pulses at 0.1 J/cm^2.

The following sections discuss the results of irradiation in combination with substrate heating in the normal operating range of the furnace. A single femtosecond pulse creates transient conditions that enhance thermal CVD and increase the yield of CNTs.

7.2 Increasing Coverage of Carbon Nanotubes in Growth Conditions with Low Yield

During CVD growth where yield of CNTs is low, irradiation with a single pulse increases the coverage of CNTs, shown in Figure 7.1. In regions that were not irradiated CNTs grew in widely separated clusters. The SEM image in Figure 7.1a shows a spot of catalyst irradiated with a single ultrashort pulse 3 minutes after the start of CVD growth. Near the middle of the laser spot the density of CNTs is greatly increased forming an entangled mat. This result was observed for catalyst irradiated 0 to 4 minutes after the start of growth. The peak fluence of the laser was 0.20 J/cm^2. The local fluence at the edge of the laser enhanced growth region is 0.10 $\pm$ 0.02 J/cm^2. The inset of Figure 7.1a from outside the laser spot

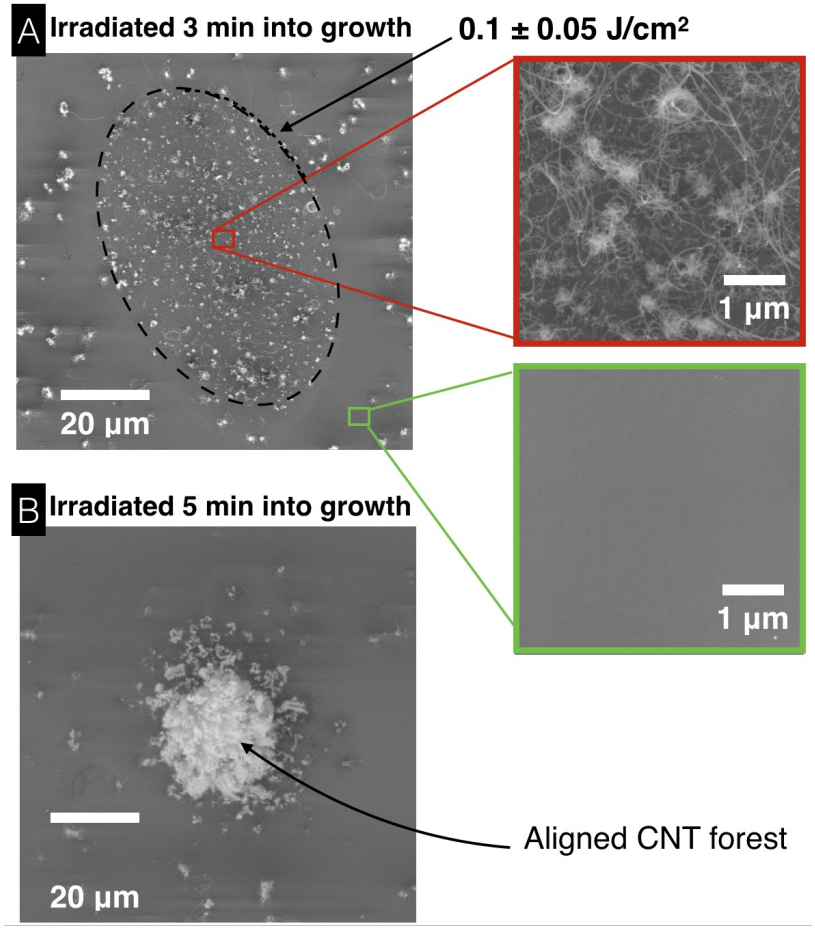

Figure 7.1: Femtosecond Laser stimulated CNT growth where CVD yield from unirradiated catalyst is low. Irradiation with a single pulse increases the coverage of CNTs. The peak fluence of the laser was 0.20 J/cm^2. Non irradiated catalyst produces widely separated clusters of CNTs. a) Irradiation above 0.1 J/cm^2 0 to 4 minutes after the start of CVD growth increases the coverage of CNTs forming an entangled mat. b) Irradiation 4-6 minutes after the start of CVD growth stimulates the growth of an aligned forest, irradiation increased the area density of active CNT catalyst above the threshold for alignment.

shows the area density of CNTs is low with small patches of CNTs separated by empty areas, this is considered to be poor growth conditions for this system. Figure 7.1b shows a spot on the same sample, also irradiated only once, but 5 min after the start of growth. In the irradiated area CNTs grew as an aligned forest. This constitutes the most dramatic improvement in CNT growth via ultrashort laser irradiation providing direct evidence that irradiation greatly increases the area density of active catalyst.

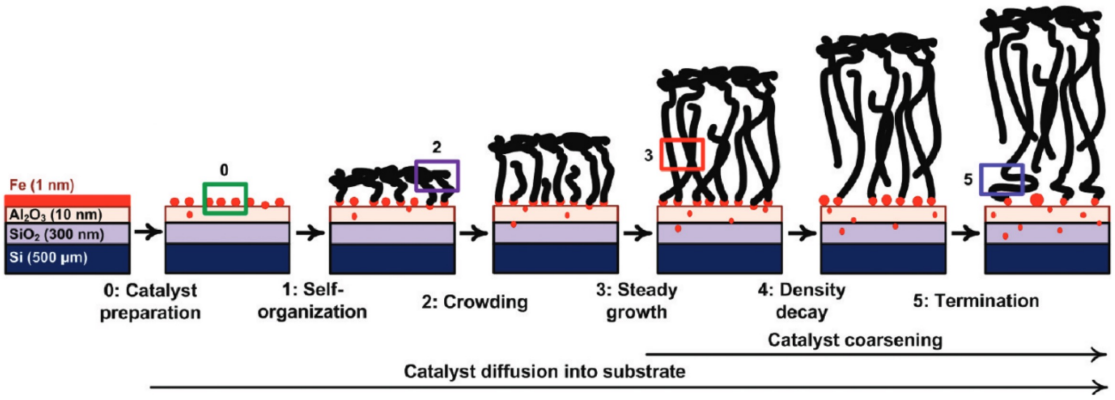

Figure 7.2: Schematic showing mechanism for growth and termination of aligned CNT forests. Aligned forests of CNTs grow where there is a high area density of active catalyst nanoparticles, CNTs crowd one another forcing alignment perpendicular to the surface. Termination of forest growth occurs when the area density of catalyst gradually drops below the minimum for self organization via a combination of mechanisms including catalyst poisoning, Oswald ripening, and diffusion into the substrate. Reprinted from [10].

A schematic of the mechanism for the growth and termination of aligned forests of CNTs is shown in Figure 7.2. Aligned forests only grow where the area density of active catalyst nanoparticles, referring to nanoparticles from which a CNT is currently growing, is above a lower limit near 1 x 10^9 cm^{-2}[10]. Initially the CNTs grow in all directions. CNTs growing parallel to the surface impinge on one another preventing further growth in the plane of the substrate so that there is only one direction for them to grow, directly away from the surface. The CNTs start to grow parallel to one another, away from the substrate, forming the aligned array resembling a forest. At this point the transition to aligned forest growth is most important. The mechanism for termination of forest growth, shown on the

right of Figure 7.2, will be discussed later.

If the concentration of active catalyst is too low, the CNTs cannot support collective forest growth. Instead the CNTs form an entangled mat and growth of individual CNTs is terminated by either steric hindrance from crowding, catalyst poisoning, Oswald ripening, or diffusion of catalyst into the substrate. The laser stimulation of forest growth in irradiated regions relative to non-irradiated regions shown in Figure 7.1b indicates that laser irradiation has increased the area density of catalyst above the threshold for aligned forest growth.

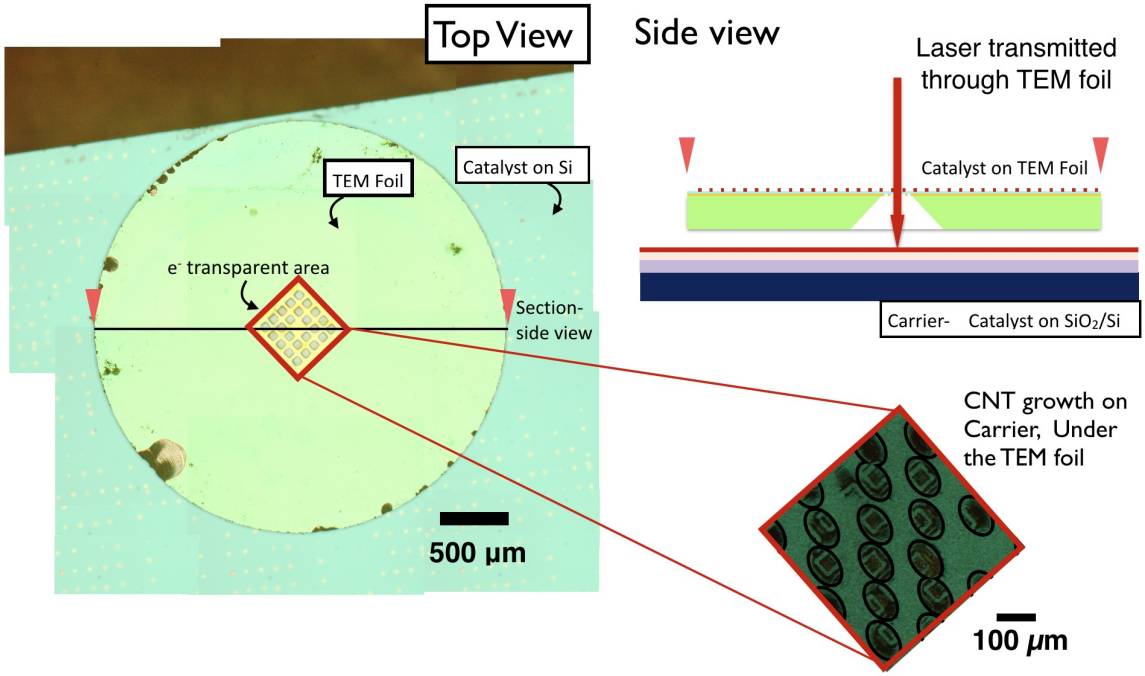

Figure 7.3: Method for locating laser spots on TEM foil using enhancement of growth on a catalyst support. A disk shaped TEM foil 3 mm in diameter covered with catalyst was placed on a carrier wafer of SiO_2/Si also covered with catalyst. At the center of the TEM foil there are 24 SiO_2 windows supported by a Si_3N_4 grid, the grid is yellow in optical microscopy. The foil was irradiated with a rectangular array of laser pulses. The laser was partially transmitted through the Si_3N_4 and SiO_2 in the TEM foil and irradiated the catalyst on the carrier. CNT growth was enhanced on the carrier in well defined spots making is possible to determine where the center of the laser spots was on the carrier and on TEM foil.

Ex-situ HRTEM was performed to directly measure an increase in the area density of

CNTs after irradiation. The Fe/Al_2O_3 catalyst was deposited on an ultrathin SiO_2 TEM foil (Ted Pella Prod #21530), replacing the standard substrate of SiO_2 on Si. The TEM foil was placed on top of another SiO_2/Si substrate with catalyst, here called the carrier, as shown in the side view of Figure 7.3. CNTs grew on both the TEM foil and the carrier surfaces. The TEM foil was irradiated with a rectangular pattern of laser spots 5 min after the start of growth, the same time as the greatest increase in area coverage of CNTs observed previously shown in Figure 7.1b. The peak fluence of the laser was 0.20 J/cm^2.

The electron transparent area of the TEM foil is also transparent to laser light. When the TEM foil was removed, well defined regions of enhanced CNT growth were observed on the carrier, shown in Figure 7.3. The enhanced patches were used to define the center of the laser spots on both the carrier and the TEM foil.

High Resolution Transmission Electron Microscopy (HRTEM) images of the irradiated foils were taken using a defocus of 2000 nm to increase the contrast of individual CNTs. Images were captured for each of the 24 ultrathin windows in the electron transparent area of the TEM foil visible in Figure 7.3. Using the ImageJ software, the HRTEM images were converted to binary, so that only contrast from CNTs was captured, and the binary images were skeletonized, defining each CNT as a line in the TEM window. Figure 7.4a shows the position of CNTs in the original TEM using yellow lines and the spatial distribution of laser fluence in the same area. It is clear upon inspection that the density of CNTs is significantly greater at higher fluence, near the center of the gaussian laser pulse, as shown in the accompanying schematic diagram in Figure 7.4b.

All 24 windows in the TEM foil were processed as in Figure 7.4a and histogram of the unit length of CNTs per unit area was measured for 60 bins of fluence between 0 to 0.20 J/cm^2. Figure 7.4c shows that coverage of CNTs in nm/μm^2 increases proportionally with the fluence.

In Figure 7.4 it is shown that the area density of CNT increases proportional to the local intensity. The sharp edges of the Si_3N_4 support grid caused a knife-edge diffraction pattern

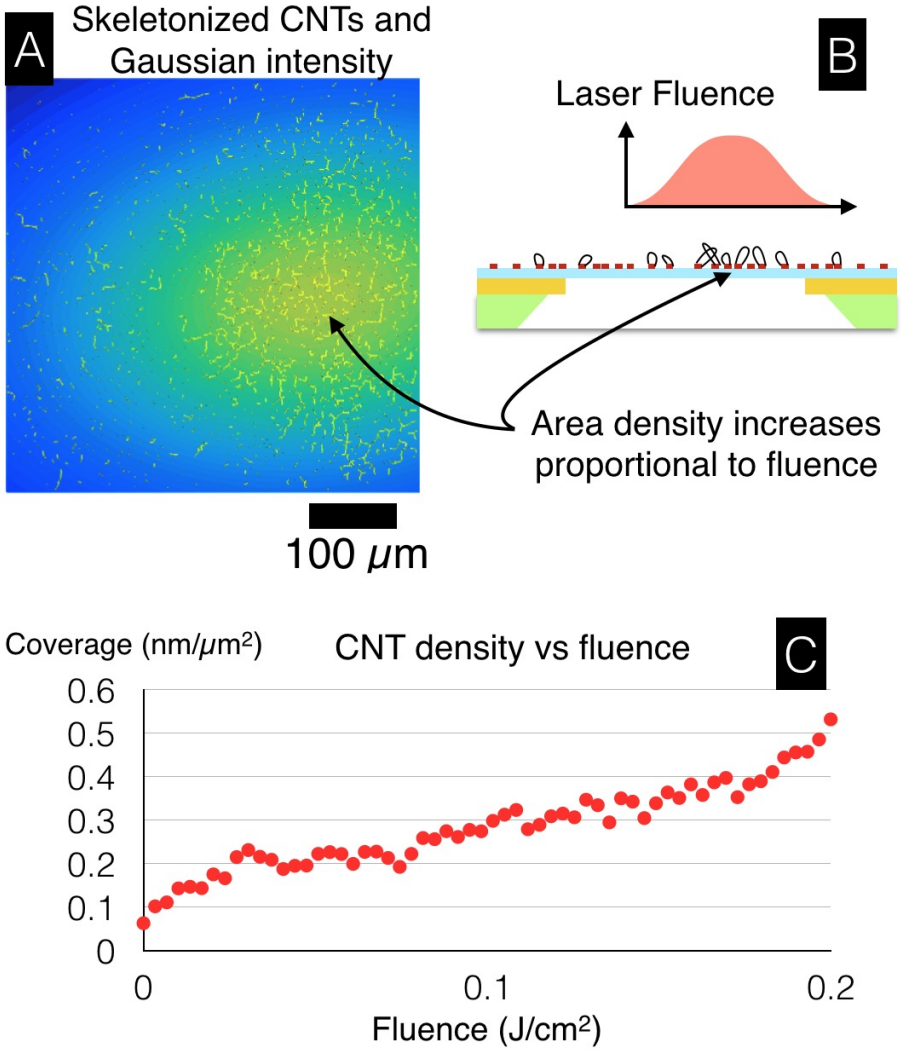

Figure 7.4: TEM measurements showing the area coverage of CNTs is proportional to laser intensity. a) TEM images of CNTs were processed using ImageJ to measure the location of CNTs, shown as yellow lines. The intensity of the laser pulse was overlaid with the CNTs. It is clear that there are more CNTs at higher fluence. b) a schematic diagram in profile showing the area density of CNTs increases with the laser intensity. c) A histogram of CNTs per unit area was measured using 24 images similar to (a) for 60 fluence bins. The area coverage of CNTs is proportional to laser intensity.

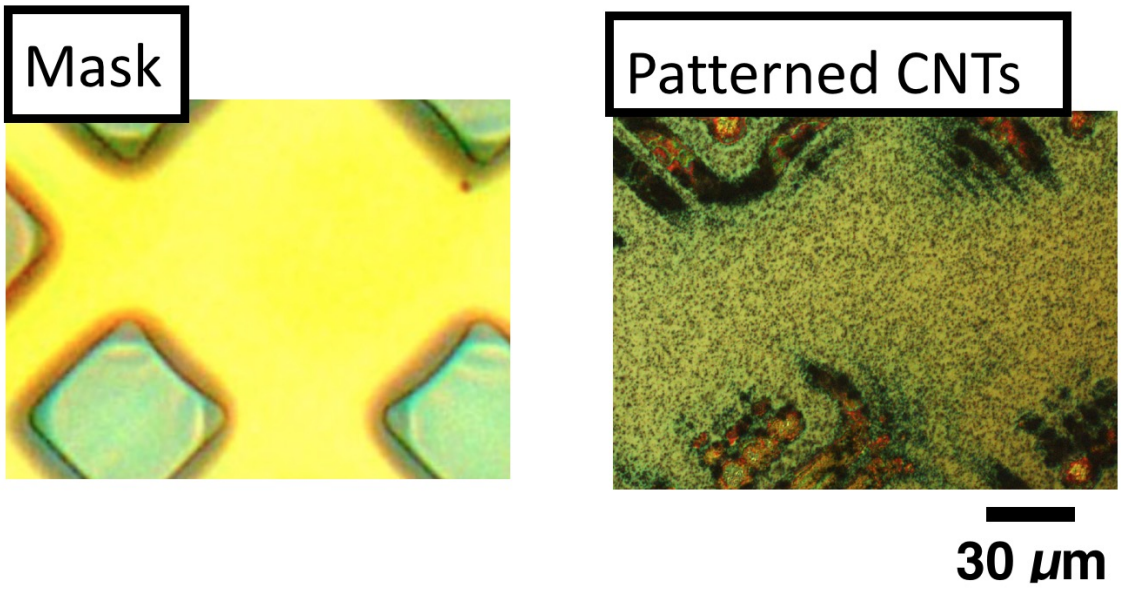

Figure 7.5: Laser patterned CNTs growth using photomasked irradiation of catalyst. The area coverage of CNTs increases proportional to the local intensity of the knife-edge diffraction pattern caused by clipping of the beam on the Si_3N_4 TEM grid. CNT enhancement, on the right, was observed to emulate the fringes formed from diffraction of laser light scattered from the Si_3N_4 support grid from the same area, shown on the left.

to form on the underlying carrier wafer. In Figure 7.5 the yellow regions are the Si_3N_4 grid acting as a photomask for the incident laser pulse; the spatial pattern of CNT enhancement on the right emulates the diffraction fringes formed by the mask.

In Summary, CVD growth of CNTs was enhanced with a single femtosecond pulse. Without laser irradiation the activity of catalyst in these experiments was very low, resulting in a diffuse entangled mat. SEM microscopy showed that irradiation of the catalyst with a single pulse 0-3 minutes after the start of CVD growth increases the area density of CNTs creating a denser mat. With increasing delay after the start of CVD growth the effect of irradiation increases. Irradiation 4-6 minutes after the start of growth resulted in the formation of an aligned forest of CNTs in the laser spot. The laser stimulation of aligned forest growth indicated that irradiation increased the area density of active catalyst in the laser spot above the critical value for crowding and self organization. To verify that irradiation increases area density catalyst was deposited on a TEM foil, was irradiated during CVD growth, and the area density of CNTs was counted HRTEM. Few nanotubes grew on the TEM foil, so the grids were placed on another catalyst covered Si wafer. The TEM foil transmits some laser light creating areas of laser enhanced growth on the underlying substrate. The patches of enhanced growth on the carrier were used to positively locate the laser irradiated regions on the TEM foil. The CNTs were counted with respect to the local fluence and it was found that the area density of CNTs increases proportional to the local fluence.

Where the laser spot was clipped by the edges of the TEM grid, a diffraction pattern was created on the underlying catalyst covered substrate. The enhanced CNT growth follows the fringes of the diffraction pattern. It is apparent that the method of femtosecond laser enhanced CVD can be combined with spatial patterning techniques including beam scanning or photomasking.

7.3 Enhancing Terminal Length of Forests

This section explores the effect of irradiation in the case of efficient CVD growth of CNTs. Without laser irradiation the density of active catalyst is sufficient for growth of aligned forests 5 to 30 microns in length. This length is still far from efficient from an outside perspective; using the Sabre furnace CNT forests 10 mm in length can be produced.

It was found that the terminal length of carbon nanotube forests could be increased by up to 150X if the catalyst was irradiated with a single pulse early after the start of CVD growth. The terminal length of the forest refers to the length of CNTs achieved before attrition of the active catalyst causes loss of alignment, as shown in the second half of Figure 7.2. Figure 7.6a shows several stalks formed when the forest in the irradiated spots grew to a much longer terminal length than the forest in the surrounding non-irradiated areas. Figure 7.6b shows an array of CNT stalks formed after the catalyst was irradiated with a square pattern of laser spots.

For Figure 7.6 the peak fluence of the laser pulses was 0.20 J/cm^2. The diameter of the stalk corresponds to a local fluence of 0.1 ± 0.02 J/cm^2, the same fluence threshold as shown in Figure 7.1a where the area density increased. The model that irradiation increases the area density of active catalyst, as seen for mild growth conditions, is consistent with a greater terminal length of CNT forests here.

Forest termination is shown in Figure 7.2. In the same way that aligned forest is initiated when the area density of active catalyst is above a critical value, termination of forest growth occurs when the area density falls below the critical value. During forest growth the area density of active catalyst is gradually dropping due to several proposed mechanisms including catalyst poisoning[11], catalyst coarsening, and diffusion into the substrate [4, 12]. Eventually the number density of active catalyst falls below a minimum for self organization and the remaining active catalyst grow CNTs in random directions forming an entangled mat at the base of the forest. It is reasonable that given the same growth environment and rates for the attrition of active catalyst, a forest with a larger population of active

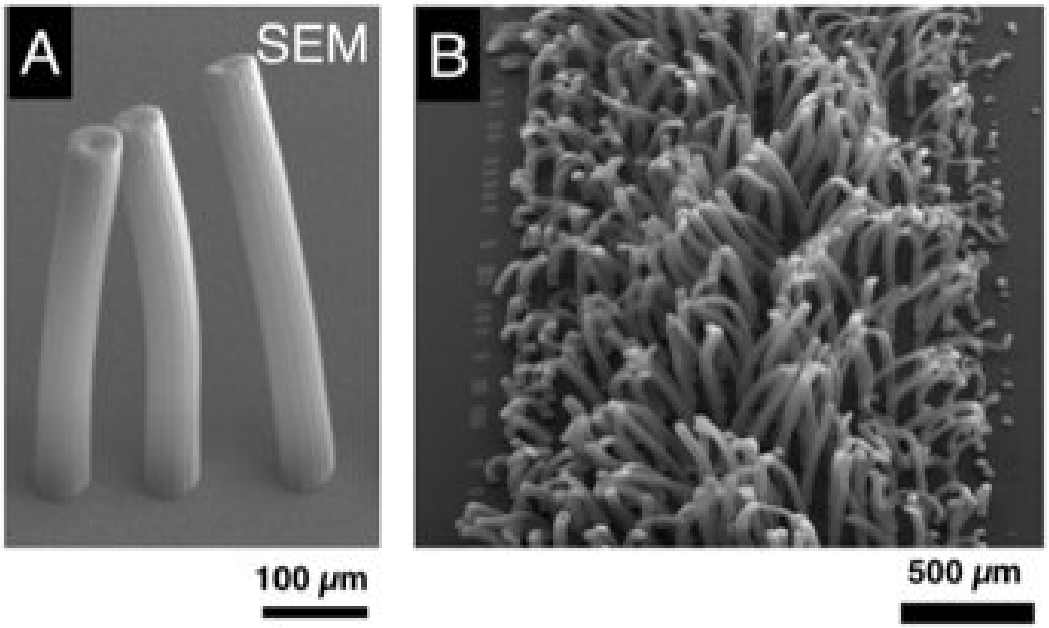

Figure 7.6: Laser patterned CNT stalk growth by beam scanning. a) A CNT forest was irradiated 20 seconds after the introduction of acetylene and the start of the growth step. Over the subsequent 10 minute growth step the forest in the irradiated region grew 500 μm in length forming the stalks. Around the stalks, in non-irradiated regions, the aligned CNT grew only 5 μm in length. The area at the base of the stalks corresponds to the center of the Gaussian laser pulse above a threshold of 0.1 J/cm^2. b) A catalyst wafer was irradiated with single pulses in a square array forming an array of stalks.

catalyst will take longer to terminate. Consequently, if the forest grows for a longer time, it grows to a greater ultimate length.

It was discovered that the terminal length of the CNT stalks depends on when the catalyst was irradiated during CVD growth. Catalyst on a SiO_2/Si wafer was irradiated from 15 seconds before to 60 seconds after the start of CNT growth in 1 second increments, each time in a pristine area. The start of CNT growth defined by the introduction of acetylene. Figure 7.7a is an SEM image of the spots irradiated between 0 and 26 seconds after the start of CVD growth. The start of CVD growth is defined as the moment acetylene flow into the reactor starts. The base of each stalk was irradiated with a single pulse at the time indicated by the labels along the bottom of the image. After growth for a total of 10 min-

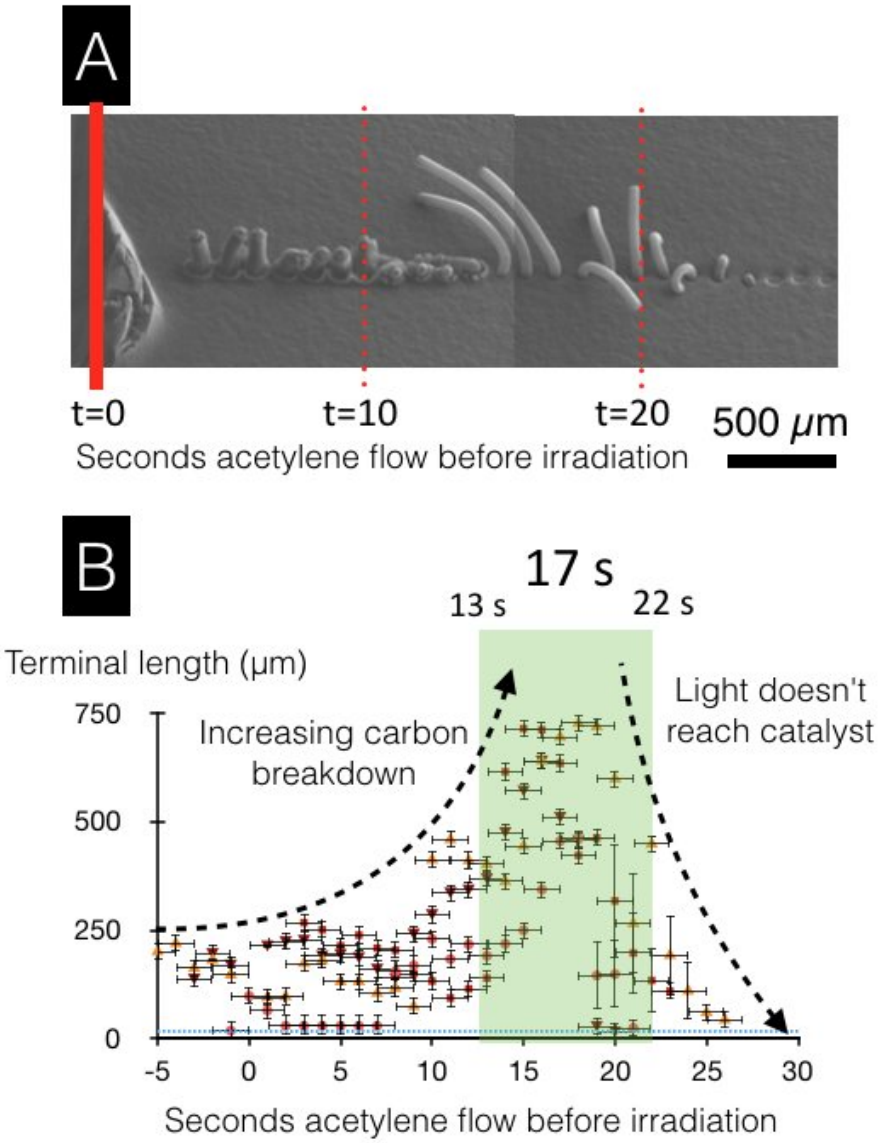

Figure 7.7: Dependance of femtosecond laser enhancement of CVD on the time for irradiation after the start of growth. The terminal length of CNT forest depends on the dynamic process of CNT nucleation and growth. The terminal length of stalks, measured in SEM, are shown with respect to the time for irradiation after the start of the growth step. Irradiation 13 to 22 seconds after the start of the growth step produces the longest CNT forest at the end of the 10 minute growth. CNT nucleation and forest growth cause two competing effects that determine the degree of laser enhanced nucleation of CNTs.

utes, the silicon heater was turned off and the flow of acetylene was stopped, ending the growth step. In-situ video showed that the stalks stopped growing taller 6 minutes after the start of growth.

The terminal length of each stalk was measured in SEM. Figure 7.7 shows the height of CNT stalks vs the time for irradiation from four experiments with the same growth parameters and irradiation conditions. The length of the tallest stalk and the optimal delay for irradiation varies slightly, but the same trends are observed in each experiment. The maximum stalk length is achieved when the catalyst is irradiated 13 to 22 seconds after the start of the growth step. If the catalyst is irradiated later than 30 seconds after the start of growth, no stalks are observed – instead, the CNT forest is partially removed forming a crater as shown in Figure 7.8. A similar damage crater is observed when a CNT forest is irradiated long after growth in a He atmosphere at 750, shown in 7.8. The threshold for damage in both cases was 0.10 ± 0.02 J/cm^2. Femtosecond laser ablation of the crust of a dense CNT forest has been observed in previous work by this research group above a threshold of 0.11 J/cm^2[13].

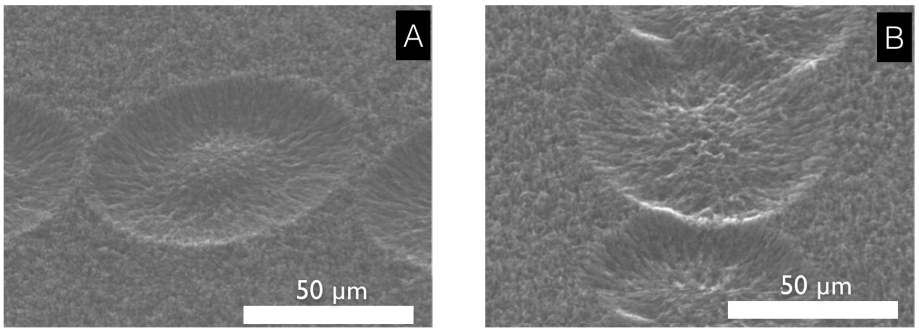

Figure 7.8: Femtosecond laser damage at the surface of CNT forests. a) Damage crater in a CNT forest irradiated during CVD growth 30 seconds after growth starts. b) Damage crater in a CNT forest irradiated long after growth ended, in a pure He atmosphere at 750 °C.

By scanning the laser beam, it was possible to create areas of continuous enhanced CNT growth. The catalyst was irradiated with single pulses in a square array with 50% overlap of laser spots, using a peak fluence of 0.20 0.02 J/cm^2, and 1000 Hz repetition

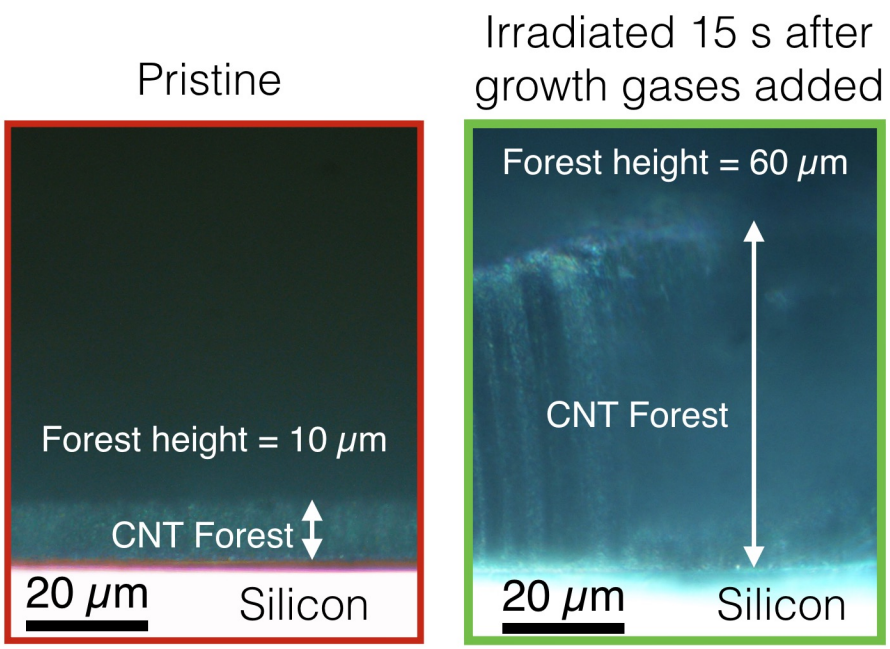

Figure 7.9: Cross section view of CNT forest in pristine and laser treated regions of catalyst. Enhanced forest growth in areas larger than the laser spot was achieved by irradiation with a square array of laser spots. The substrate was cleaved, and the forest was viewed in profile using dark field optical microscopy. a) The forest in a pristine region grew 10 μm in length. b) The forest irradiated with the laser pattern 15 sec after the start of growth grew 60 μm in length.

rate. The SiO_2/Si substrate was cleaved to view the forest in profile and measure the length of the pristine forest and the enhanced forest. Figure 7.9 shows that the terminal length of the forest where the catalyst was irradiated 15 sec after the start of CVD growth was 60 microns long, 6X greater than in pristine regions. The top of the enhanced forest was not uniform, featuring random fissures and stalk tips protruding several microns above or below the average level of the crust in the enhanced pattern.

Previous studies using a multilayer metal catalyst have shown that pre-irradiation with a nanosecond laser in air, before annealing or growth, increases the CVD growth rate of aligned forests by a factor of 3[5]. It was found that the catalyst activity in the irradiated region was unchanged, but CNTs had a significantly lower wall thickness and diameter. CNTs with a smaller diameter and wall thickness contain less carbon per unit length. The

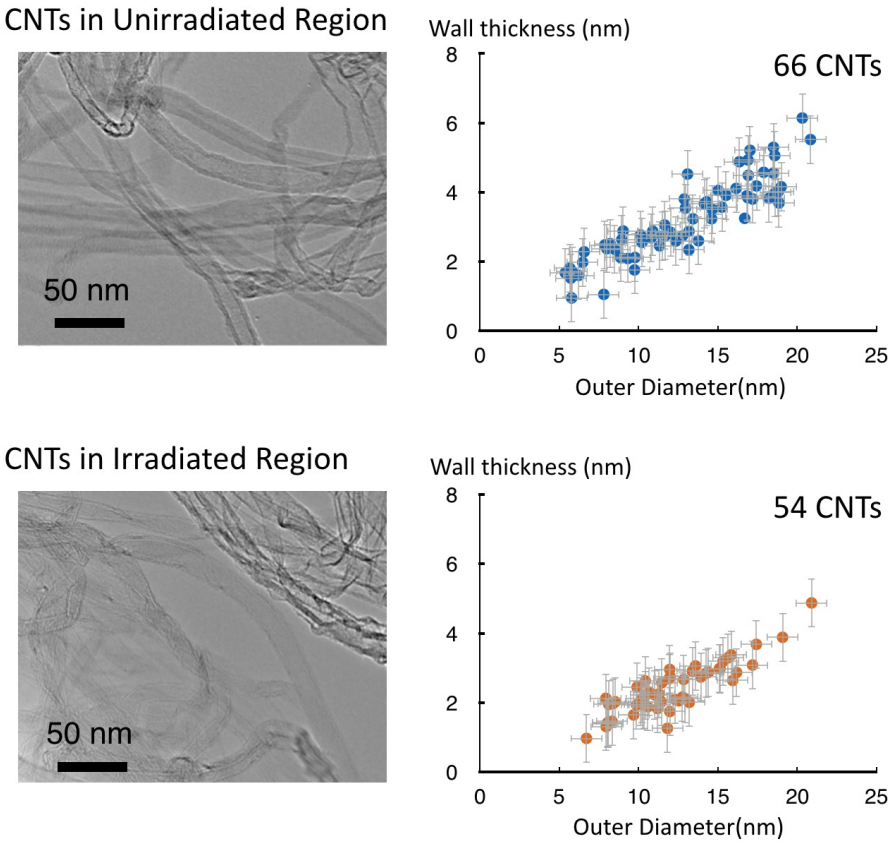

Figure 7.10: Distribution of CNT diameter and wall thickness from pristine and laser irradiated catalyst. CNTs from non-irradiated and laser enhanced forest were observed using HRTEM.The average wall thickness and outer diameter of tubes in the stalk showed a small shift toward smaller wall thickness and diameter, but not as significant as in the case of nanosecond laser pre-treatment of catalyst[5]. The minor reduction in the wall thickness and diameter does not account for the 50 to 150X greater length of CNTs observed in this work.

authors proposed that for the same catalyst activity, meaning mass of CNTs per unit area and per unit time, the narrow CNTs must grow a greater length resulting in a faster growth rate of the forest. This possibility was investigated in this work.

CNTs were collected from the stalks and non-irradiated forest, distributed on lacey carbon grids, and observed using HRTEM, as shown in Figure 7.10. Figure 7.10 shows the outer diameters and wall thickness of approximately 60 CNTs from both the pristine forest and the irradiated stalk. On average, CNTs in the stalk have marginally smaller wall thickness and diameter than CNTs from pristine areas, insufficient to account for up to 150% increase in the length.

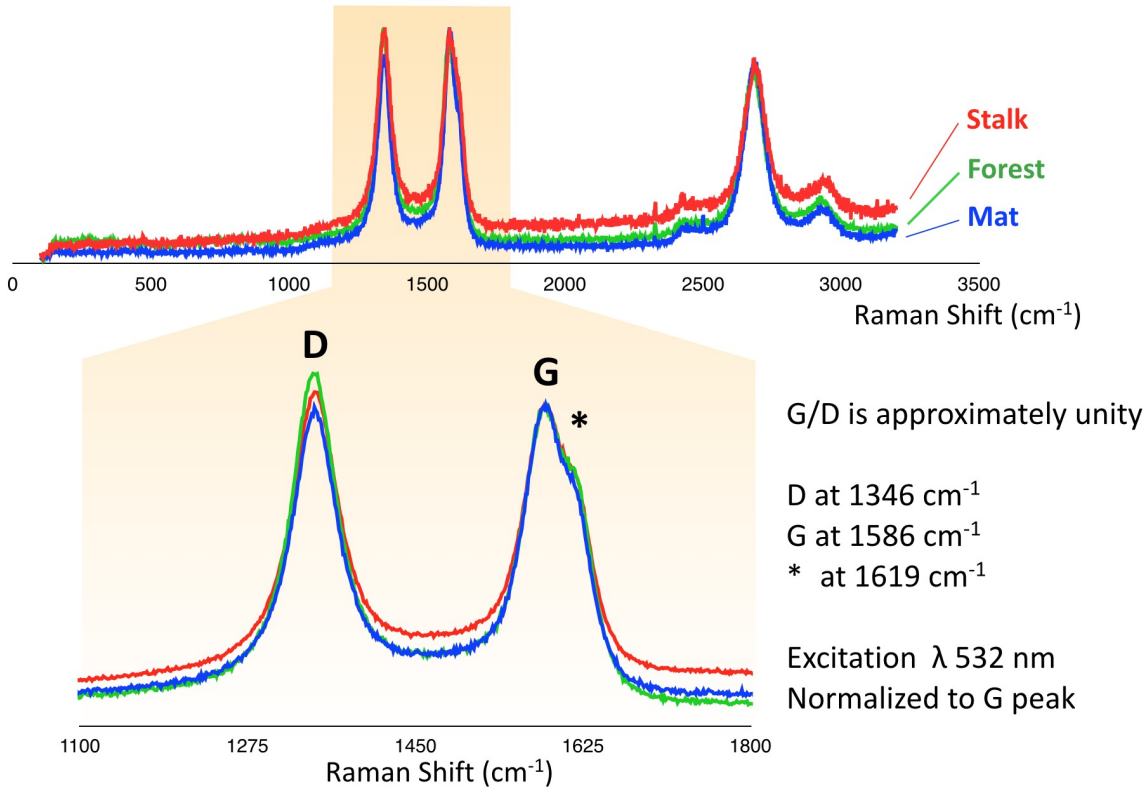

Figure 7.11: Raman Spectra of CNTs from pristine and laser irradiated regions. Raman spectroscopy was performed using an excitation wavelength of 532 nm. The Raman spectra of CNTs from pristine and laser irradiated catalyst were identical and indicate highly defected, multiwalled CNTs.

Raman spectra were collected using an excitation wavelength of 532 nm for CNTs in

irradiated areas (the stalks) and from pristine catalyst. The traces labeled "forest" and "mat" both correspond to pristine catalyst, but for growth runs where pristine CNTs formed an aligned forest or a disorganized mat respectively. The spectra are nearly identical for each sample. The peak ratios observed are indicative of highly defective graphite or amorphous carbon[14, 15], also consistent with highly defective multiwalled CNTs.

In summary, femtosecond laser irradiation can enhance the method of CVD growth of CNTs. Single or multiple pulse irradiation with the femtosecond laser does not cause CNTs to grow at room temperature or temperatures below the minimum for thermal CVD. In poor CVD growth conditions, where very few CNTs grow in diffuse clusters, irradiated areas have increased coverage of CNTs forming an entangled mat or an aligned CNT forest. Promoting forest growth via irradiation indicates that the area density of active catalyst was increased in the laser spot. Delaying irradiation longer after the start of growth promoted more CNT growth in the laser spot.

In good growth conditions, where the area density is near or above the limit for aligned forest growth, irradiation with a single laser pulse can increase the terminal length of aligned CNT forests by up to 150X. Increased forest growth is consistent with increasing the area density of catalyst, as previously discovered for poor growth. Aligned forest growth terminates when the area density of active catalyst falls below a threshold due to the gradual loss and poisoning of active catalyst. Irradiation increases the initial density of active catalyst so it takes longer to drop below the threshold for alignment; delaying forest termination leads to a longer forest. By scanning the laser beam it was possible to create areas of continuous enhanced CNT growth. It was found that the terminal length of the forest in laser irradiated regions was very sensitive to the delay for irradiation, the maximum length of the forest was observed for irradiation 13 to 22 seconds after the start of CVD growth. The mechanism for laser activation of the CNT catalyst, consistent with the precise dependence on the time for irradiation, is discussed in the next section.

7.4 Femtosecond Laser Activation of Catalyst

In this section, a model is presented for femtosecond laser activation of catalyst during CVD growth. Observations using in-situ optical microscopy are presented. It is shown that laser absorption in the catalyst/substrate and ablation of CNTs on the surface are critical factors. The dependence of enhanced growth on the delay for irradiation after the start of growth is explained in terms of the laser interaction with the dynamics of CNT growth.

In-situ video of CNT growth was captured from an 80 degree angle of incidence, nearly in profile, as shown in Figure 7.12. The in-situ camera is sensitive to visible and near infrared light. It has been shown that blackbody emission increases with increasing CNT coverage [16]. The brightness of in-situ images is proportional to the coverage of CNTs. During growth several 2 mm x 3 mm areas were irradiated with a square array of laser spots, as shown in Figure 7.12a. The pattern used a peak fluence of 0.2 0.02 J/cm^2, 50% overlap of spots in both directions, and 1000 Hz repetition rate. Because of the limited spot size and repetition rate each pattern took six seconds to write. Half of the surface was left pristine as a control.

Three patterned areas are shown in Figure 7.12b and d. Figure 7.12b shows an image captured 16 seconds after the start of growth, the pattern ranging from 12-18 seconds is in progress. Areas irradiated 12 to 14 seconds after growth are brighter than the pristine region indicating the CNT coverage is higher after only a few seconds. The coverage of CNTs was observed using bright field optical microscopy in Figure 7.12d. Areas with higher CNT coverage absorb more visible light, and appear darker. The area irradiated 12 to 18 seconds has higher coverage of CNTs than both the unirradiated area and the area irradiated 0 to 6 seconds after the start of growth. This result is consistent with Figure 7.7b where the optimum timing for irradiation was 13 to 22 seconds after the start of CVD growth.

In-situ images also show that light is emitted from the catalyst surface during irradiation later than 12 seconds after the start of growth. Light emission at early times is shown on

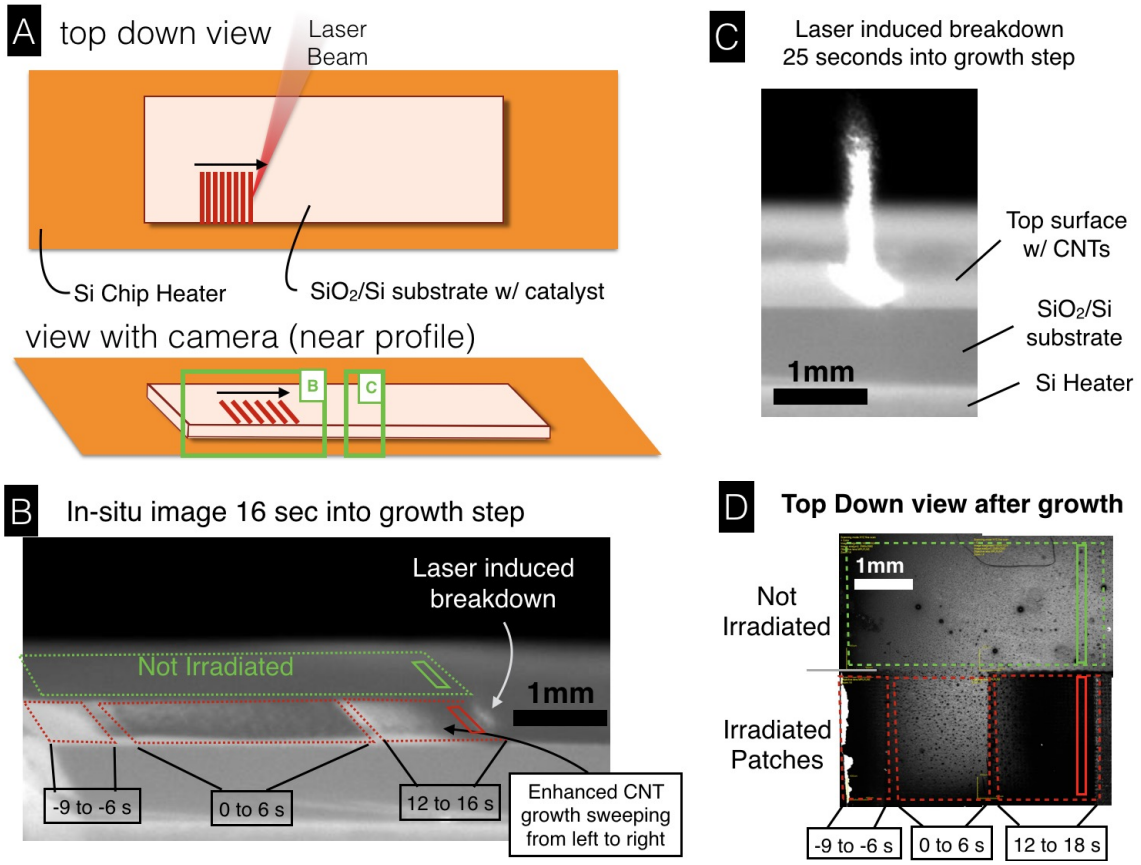

Figure 7.12: In-situ optical microscopy of laser irradiation of CNTs during CVD growth. a) The front half of a SiO_2/Si substrate with catalyst was irradiated with 2-d pattern of laser spots. Limited spot size and repetition rate meant that the patterns took several seconds to write. Patterns were written left to right, the starting and ending times are labeled b) In-situ image captured 16 seconds after the start of growth, the pattern from 12-18 seconds is in progress. The camera captures blackbody emission, brighter areas on the surface correspond to higher CNT coverage. CNT coverage in areas irradiated 12 to 14 seconds after growth is higher than the pristine region, several seconds later. c) Example of laser induced breakdown when a surface with high coverage of CNTs is irradiated. d) An ex-situ optical image of the catalyst after growth, top down. Areas with higher CNT coverage absorb more visible light. The area irradiated 12-18 seconds after growth has the highest concentration of CNTs.

the right of Figure 7.12b. At later times when more CNTs have grown and the coverage is higher, a bright plume is formed after irradiation shown in Figure 7.12c. No light emission is observed when the SiO_2/Si substrate was irradiated with the same peak fluence in atmospheres of acetylene, helium, or hydrogen. No light emission is observed when the catalyst is irradiated at room temperature or during the annealing step at 750 °C. The spark is not formed by the laser induced breakdown of acetylene, the Si/SiO_2 substrate, or Fe/Al2O3 catalyst. The observed light emission is caused by the laser induced breakdown of CNTs, possibly similar to previous studies of femtosecond laser breakdown of graphite. Light emission after irradiation of graphite was caused by blackbody emission and characteristic emission from carbon atoms and clusters[17].

The contrast in in-situ optical images, for example Figure 7.12b, is a combination of blackbody emission and the breakdown of CNTs. Each source of contrast was measured separately to examine the dynamics of growth and laser interaction with CNTs was measured and is shown in Figure 7.13. The minimum, mean, and maximum grey value was measured within a 1x3 mm region surrounding the laser spot for each image 12 to 18 seconds after the start of CVD growth, shown in Figure 7.13a. The data shows the intensity of light from laser breakdown emission of CNTs is proportional to the coverage of CNTs at the time of irradiation, shown in Figure 7.13b. The brightness of IR emission, proportional to the area coverage of CNTs, was measured with respect to time for pristine catalyst and catalyst irradiated 18 seconds after the start of growth using the regions of interest shown with solid rectangles in Figure 7.12 b and d. Before irradiation, the brightness increases the same in both regions. Spikes in the measured brightness 18 seconds after the start of growth are caused by laser induced breakdown of CNTs. After irradiation, the brightness of the irradiated region is lower than the pristine area, indicating the coverage of CNTs has been reduced. Between 19 and 21 seconds, several seconds after irradiation the brightness in the irradiated region increases rapidly, indicating the area density of CNTs recovers rapidly and exceeds the pristine region. The irradiated region has higher coverage of CNTs at the

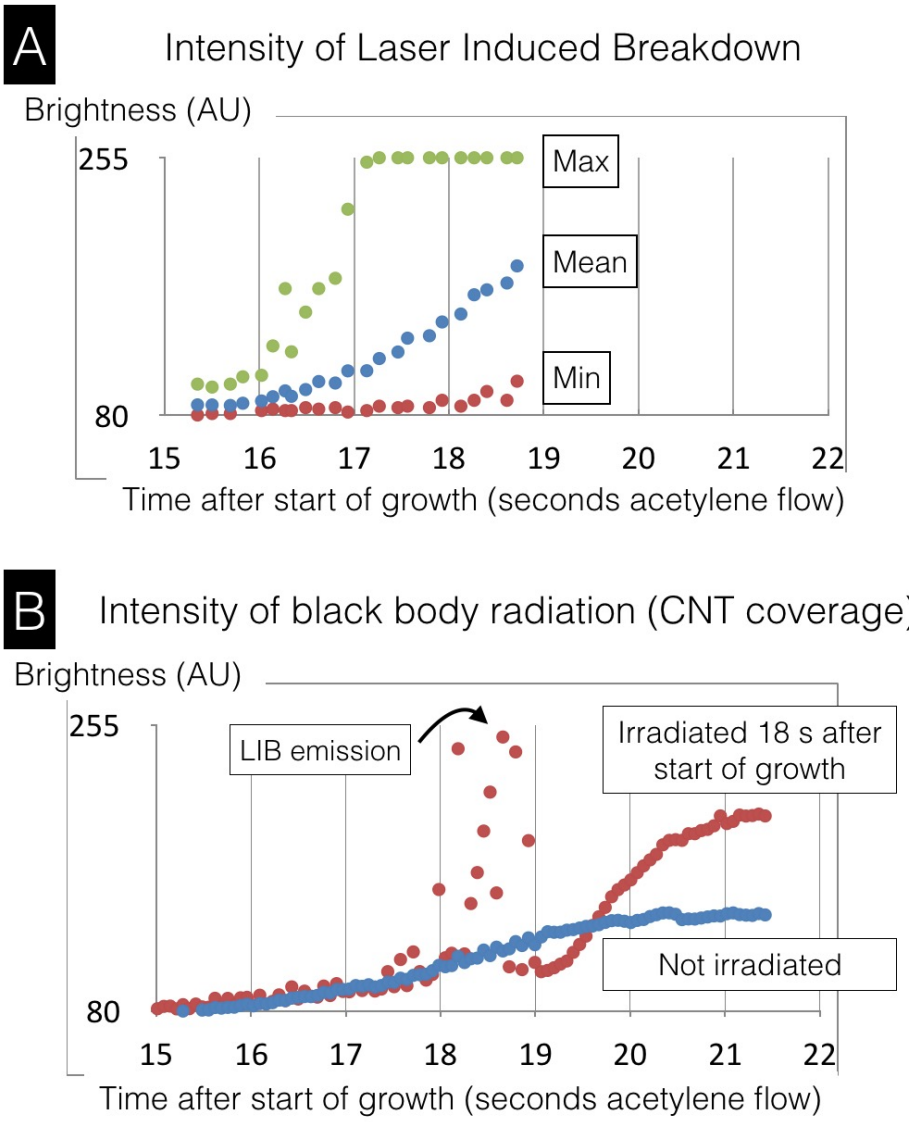

Figure 7.13: Laser induced breakdown emission and blackbody emission from CNTs measured for fs-laser irradiation early during CVD growth. a) The intensity of light emitted from the laser induced breakdown of CNTs was monitored 12 to 18 seconds after the start of CVD growth. The minimum, mean and maximum grey value was monitored for a 1x3 mm region following the laser spot. b) The IR emission from pristine catalyst and catalyst irradiated 18 sec after the start of growth was monitored with respect to time for the CVD growth run shown in Figure 7.12. The two regions of interest are shown in Figure 7.12b and d. Before irradiation the brightness increases the same in both regions. Spikes in the irradiated region at 18 seconds are caused by laser induced breakdown of CNTs. After irradiation the brightness of the irradiated region is lower than the pristine area, indicating CNTs have been destroyed. Between 19 and 21 seconds the brightness in the irradiated region increases well above the pristine region.

end of growth as shown in Figure 7.12d.

A possible mechanism for femtosecond laser stimulated nucleation was developed considering two key observations. First, irradiation breaks down CNTs on the surface, then the CNT coverage increases beyond its original level. Second, with increasing delay for irradiation relative to the start of CVD growth, and therefore increasing coverage of CNTs at the time of irradiation, the terminal length of the stalks initially increases as shown in Figure 7.7 and in inefficient growth conditions the area coverage of CNTs increases as shown in Figure 7.1.

However, it was also observed that irradiation late in the growth step does not enhance CNT growth. In the case of efficient CNT growth this could occur due to light absorption in the aligned forest: instead of laser energy reaching the catalyst it is absorbed in the crust of the CNT forest and forms an ablation crater. In the case of inefficient CVD growth the number density of catalyst may have already fallen due to coarsening or diffusion into the substrate before irradiation.

Femtosecond laser irradiation changes the environment of the catalyst in two ways. Irradiation destroys CNTs on the catalyst surface producing an atmosphere that is likely similar to PLV of graphite, consisting of ionized carbon and carbon clusters[18–21]. Irradiation also heats the catalyst through a combination of absorption by the metal nanoparticle and absorption by the attached nanotubes similar to previous studies using nanosecond laser irradiation[22] and continuous wave lasers[23]. Transient heating of the catalyst in an atmosphere rich with CNT breakdown products could drive a process of carbon absorption and precipitation similar to femtosecond laser driven hyperdoping. It has been shown that melting and quenching of silicon in an atmosphere containing a dopant species at high pressure drives absorption of dopant atoms in the liquid phase that are trapped as the Si rapidly solidifies. After irradiation with multiple pulses the dopant concentration in the solid can far exceed the equilibrium solubility limit.

The growth temperature the Fe catalyst is near the eutectoid temperature in the Fe-C

phase diagram [24]. Laser induced heating of the catalyst nanoparticle into the gamma phase would increase the carbon solubility approximately linearly between 750 °C and 1153 °C [24], or dramatically increase the solubility if the nanoparticle is melted. Nanoparticles heated by the laser are exposed to a high concentration of gaseous carbon from PLV of nanotubes. As the nanoparticle cools and the solubility limit of carbon falls and excess carbon precipitates possibly leading to nucleation of a CNT.

The trend of increasing impact of laser irradiation later in the growth step, correlating with the increasing CNT coverage, may be caused by ablation of more CNTs increasing the density of carbon vapor or increasing absorbance of the surface leading to higher peak temperature and longer time at high temperature. Either effect could increase the carbon dissolved by irradiated catalyst nanoparticles and promote laser stimulated nucleation of CNTs.

Recent work has shown that the formation of Fe catalyst nanoparticles is not complete during the annealing step. The FeO catalyst is partially reduced and begins to dewet, but nanoparticles of Fe that will form a CNT do not appear until after absorption of carbon[25] from the growth gas or from residual carbon in the growth chamber. Femtosecond laser breakdown of the existing CNTs produces a rich carbon atmosphere that could promote restructuring the Fe catalyst thin film into nanoparticles ready to nucleate a larger population of CNTs.

In summary, we demonstrate that the femtosecond laser irradiation can be used to enhance thermal CVD of CNTs by increasing the area density of active catalyst. In poor growth conditions, where CNTs grow in a diffuse mat, it was shown that the area density of CNTs was increased by laser irradiation of the catalyst during CVD growth. In some cases the area density of active catalyst was increased above the limit for self organization and growth of aligned forests of CNTs. In that case aligned forests only grew where the catalyst was irradiated.

In the case of more efficient CVD growth conditions, sufficient for the growth of aligned

forests without irradiation, the aligned forests grew to much greater terminal length where the catalyst was irradiated. The mechanism for increasing the terminal length of aligned CNT forests was not positively determined, but laser stimulated nucleation is consistent with increased terminal length of aligned forests. Increasing the area density could delay forest termination since the initial population of active catalyst is increased and will take longer to fall below the limit for self organization.

A mechanism was proposed for laser stimulated nucleation consistent with the experimental observation that laser stimulated growth depends on PLV of preexisting CNTs. Irradiation heats the catalyst, increasing the carbon solubility, and vaporizes the existing CNTs, creating an atmosphere rich with carbon. The catalyst absorbs carbon, then upon cooling precipitates the carbon, potentially as a CNT. While more study is required to verify the proposed mechanism, the combination CVD synthesis and PLV synthesis demonstrated here provides a novel and simple route to efficient growth in systems where the static growth parameters are not optimized. The methods demonstrated here may also be used to pattern growth of aligned CNT forests without pre-pattering catalyst via photolithography, or post processing.

References

1. Volder, M. F. L. D., Tawfick, S. H., Baughman, R. H. & Hart, A. J. Carbon Nanotubes: Present and Future Commercial Applications. *Science* **339,** 535–539 (Feb. 1, 2013).
2. Zhang, R., Zhang, Y., Zhang, Q., Xie, H., Qian, W. & Wei, F. Growth of Half-Meter Long Carbon Nanotubes Based on Schulz–Flory Distribution. *ACS Nano* **7,** 6156–6161 (July 23, 2013).
3. Vinten, P., Marshall, P., Lefebvre, J. & Finnie, P. Distinct termination morphologies for vertically aligned carbon nanotube forests. *Nanotechnology* **21,** 035603 (Jan. 22, 2010).
4. Bedewy, M., Meshot, E. R., Reinker, M. J. & Hart, A. J. Population Growth Dynamics of Carbon Nanotubes. *ACS Nano* **5,** 8974–8989 (Nov. 22, 2011).
5. Rouleau, C. M., Eres, G., Cui, H., Christen, H. M., Puretzky, A. A. & Geohegan, D. B. Altering the catalytic activity of thin metal catalyst films for controlled growth of chemical vapor deposited vertically aligned carbon nanotube arrays. *Applied Physics A* **93,** 1005–1009 (July 3, 2008).
6. Prasek, J., Drbohlavova, J., Chomoucka, J., Hubalek, J., Jasek, O., Adam, V. & Kizek, R. Methods for carbon nanotubes synthesis—review. *Journal of Materials Chemistry* **21,** 15872–15884 (2011).
7. Szabó, A., Perri, C., Csató, A., Giordano, G., Vuono, D. & Nagy, J. B. Synthesis Methods of Carbon Nanotubes and Related Materials. *Materials* **3,** 3092–3140 (May 7, 2010).
8. Nikolaev, P., Hooper, D., Webber, F., Rao, R., Decker, K., Krein, M., Poleski, J., Barto, R. & Maruyama, B. Autonomy in materials research: a case study in carbon nanotube growth. *npj Computational Materials* **2,** 16031 (2016).
9. Liu, Z., Styers-Barnett, D. J., Puretzky, A. A., Rouleau, C. M., Yuan, D., Ivanov, I. N., Xiao, K., Liu, J. & Geohegan, D. B. Pulsed laser CVD investigations of single-wall carbon nanotube growth dynamics. *Applied Physics A* **93,** 987–993 (Dec. 2008).
10. Bedewy, M., Meshot, E. R., Guo, H., Verploegen, E. A., Lu, W. & Hart, A. J. Collective Mechanism for the Evolution and Self-Termination of Vertically Aligned Carbon Nanotube Growth. *Journal of Physical Chemistry C* **113,** 20576–20582 (Dec. 3, 2009).

11. Stadermann, M., Sherlock, S. P., In, J.-B., Fornasiero, F., Park, H. G., Artyukhin, A. B., Wang, Y., De Yoreo, J. J., Grigoropoulos, C. P., Bakajin, O., Chernov, A. A. & Noy, A. Mechanism and Kinetics of Growth Termination in Controlled Chemical Vapor Deposition Growth of Multiwall Carbon Nanotube Arrays. *Nano Letters* **9,** 738–744 (Feb. 11, 2009).

12. Kim, S., Pint, C., Amama, P., Zakharov, D., Hauge, R., Maruyama, B. & Stach, E. Evolution in catalyst morphology leads to carbon nanotube growth termination. *The Journal of Physical Chemistry Letters* **1,** 918–922 (2010).

13. Murphy, R. D. *Femtosecond Laser Interactions at Interfaces and Their Applications.* PhD thesis (University of Michigan, 2013).

14. Ferrari, A. C. & Robertson, J. Raman spectroscopy of amorphous, nanostructured, diamond-like carbon, and nanodiamond. *Philosophical Transactions of the Royal Society A: Mathematical, Physical and Engineering Sciences* **362,** 2477–2512 (Nov. 15, 2004).

15. Ferrari, A. C. & Robertson, J. Interpretation of Raman spectra of disordered and amorphous carbon. *Physical Review B* **61,** 14095–14107 (May 15, 2000).

16. Haluska, M., Bellouard, Y., van de Burgt, Y. & Dietzel, A. In situ monitoring of single-wall carbon nanotube laser assisted growth RID B-6920-2008. *Nanotechnology* **21** (Feb. 19, 2010).

17. Amoruso, S., Ausanio, G., Vitiello, M. & Wang, X. Infrared femtosecond laser ablation of graphite in high vacuum probed by optical emission spectroscopy. *Applied Physics A* **81,** 981–986 (Oct. 2005).

18. Puretzky, A. A., Schittenhelm, H., Fan, X., Lance, M. J., Allard, L. F. & Geohegan, D. B. Investigations of single-wall carbon nanotube growth by time-restricted laser vaporization. *Physical Review B* **65** (June 24, 2002).

19. Guo, T., Nikolaev, P., Thess, A., Colbert, D. T. & Smalley, R. E. Catalytic growth of single-walled manotubes by laser vaporization. *Chemical Physics Letters* **243,** 49–54 (Sept. 8, 1995).

20. Jeschke, H., Garcia, M. & Bennemann, K. Theory for the Ultrafast Ablation of Graphite Films. *Physical Review Letters* **87,** 015003 (June 2001).

21. Lenner, M., Kaplan, A., Huchon, C. & Palmer, R. Ultrafast laser ablation of graphite. *Physical Review B* **79,** 184105 (May 2009).

22. Puretzky, A. A., Eres, G., Rouleau, C. M., Ivanov, I. N. & Geohegan, D. B. Real-time imaging of vertically aligned carbon nanotube array growth kinetics. *Nanotechnology* **19,** 055605 (Feb. 6, 2008).

23. Bock, M. C. D., Denk, R., Wirth, C. T., Goldberg-Oppenheimer, P., Hofmann, S. & Baumberg, J. J. Optical feedback mechanisms in laser induced growth of carbon nanotube forests. *Applied Physics Letters* **100** (Jan. 2, 2012).

24. Chipman, J. Thermodynamics and phase diagram of the Fe-C system. *Metallurgical Transactions* **3,** 55–64 (Jan. 1972).

25. Bedewy, M., Viswanath, B., Meshot, E. R., Zakharov, D. N., Stach, E. A. & Hart, A. J. Measurement of the Dewetting, Nucleation, and Deactivation Kinetics of Carbon Nanotube Population Growth by Environmental Transmission Electron Microscopy. *Chemistry of Materials* **28,** 3804–3813 (June 14, 2016).

CHAPTER 8

Conclusions

This dissertation explores the effect of irradiation with a single femtosecond laser pulse on the microstructure and composition of thin metal films using time resolved and post mortem microscopy methods. The primary feature of femtosecond laser irradiation is that it deposits a high energy density in materials. After irradiation of metals, thin layers at the surface of materials are driven to extreme temperatures and pressures, thereby creating sharp gradients that lead to relaxation along a non-equilibrium path and into extreme metastable states. The materials that were irradiated in this work had complex structures including interfaces, previously unexplored alloy compositions, and in the case of metal catalyst nanoparticles and CNTs, two materials with dramatically different responses to irradiation along with a dynamic chemical reaction. It would be difficult to predict the response of these materials to femtosecond laser irradiation, every aspect of the problem is complicated from the absorption and redistribution of energy to the issue of phase transformations or mass transport given rapid heat transport and quenching. By exploring complex systems experimentally, relying on some intuition to guide the sequence of experiments, the experimental results in this dissertation provided a fundamental understanding of materials response to femtosecond laser irradiation, as in the case of spinodal-like decomposition of metal stabilized by an interface. Simultaneously, new materials processing techniques were discovered as in the case of laser stimulated nucleation of CNTs during thermal CVD or the formation of nanocrystalline alloy films after irradiation.

This dissertation seeks to determine the mechanism for separation of ultrathin metal films from a substrate after irradiation by

1. Observing the dynamics of removal for ultrathin Ni thin film on glass substrates using time-resolved pump-probe microscopy.

2. Identifying a mechanism for the rapid formation of vapor that severs the Ni-substrate interface.

Removal of ultrathin Ni films can occur by two distinct mechanisms. Liquid spallation removes a uniform layer less than half of the film thickness. At higher fluences removal occurs at the interface by the heterogeneous nucleation of voids. The configuration and velocity of the moving layers was measured using Newton's rings that formed through thin film interference between the stationary substrate and moving films. It was shown that two separate systems of Newton's rings were formed corresponding to the intrafilm and interface removal regions respectively, therefore after irradiation a 7 nm layer is removed above the intrafilm removal threshold and a second 13 nm layer is ejected from the interface removal region. The velocity of the intrafilm removal layer is 300 to 500 % faster than the interface removal layer. The measured velocity of each ejected film were consistent with simulations of ultrathin Pt films[1] where intrafilm removal occurred by liquid spallation and interface removal occurred by the heterogeneous nucleation of vapor at the Pt/substrate interface. However, in that MD simulation the ejected layers accelerated to their final velocity over ~1 ns due to the expansion of vapor between the substrate and the ejected layers. Pump-probe measurements in this work showed that the layers removed by intrafilm and interface removal both reached the final velocity within 50 ps.

A mechanism was proposed for the rapid development of Ni vapor at the Ni/substrate interface. Hydrodynamic simulations of the Ni film at the fluence for separation at the interface showed that the Ni film entered the vapor dome in the temperature-pressure phase diagram near, but not within, the critical point phase separation region defined as $>$90%

of the critical temperature[2]. For irradiation of bulk metals such that the surface layer is driven into the critical point phase separation region, the material becomes unstable and undergoes a spinodal-like decomposition leading the the homogeneous nucleation of vapor within a few picoseconds after irradiation. The same instabilities exist after irradiation at lower fluences, but are not strong enough to lead to the formation of stable homogeneous nuclei of vapor. It is suggested that at temperatures below the critical point phase separation region the Ni-glass interface can stabilize vapor that forms via spinodal-like decomposition separating the Ni-glass interface within a few picoseconds. The temporal resolution using Newton's rings was limited and it was not possible to measure separation of the Ni-substrate interface on the picosecond timescale.

The Ni-substrate interface plays two roles in this study. Ultrathin Ni films irradiated by a femtosecond pulse exhibit liquid spallation limited to a depth slightly less than the film thickness. Material driven into the vapor dome at high temperatures, as in the case of interface removal of 20 nm Ni films, is normally within the depth of liquid spallation in a bulk material so it is difficult to observe. Second the interface provides a location for the formation of heterogeneous nuclei. The characteristics of material that enters the vapor dome after irradiation is of great interest because this state is often entered after femtosecond laser irradiation but remains difficult to study experimentally. This work indicates that material in the vapor dome is unstable over a wider range of temperatures than perviously studied and that a process similar to critical point phase separation can occur outside the previously described temperature range given the correct energetic environment, e.g. an interface.

This dissertation explores femtosecond laser irradiation of ultrathin multilayer, multicomponent metal films as a technique to form alloys of metals with limited solubility by

1. Demonstrating that homogeneous mixtures of elements can be formed by femtosec-

ond laser melting and quenching.

2. Observing the morphology of the removal craters and microstructure of alloys formed via irradiation in terms of the local fluence.

3. Defining the conditions after irradiation that lead to the observed range of removal craters and microstructures in multicomponent, multilayer metal films.

It was found that ultrathin multilayer Ni-W films on Ni substrates exhibit intrafilm and interface removal similar to removal of pure Ni films. The thresholds for intrafilm and interface removal were 0.20 J/cm^2 and 0.47 J/cm^2 respectively. Intrafilm removal by liquid spallation causes removal of the top half of the multilayer film, interface removal occurs at the interface between the Ni-W film and the Ni substrate. After irradiation above the melting threshold and even above the liquid spallation threshold, the as-deposited layers of Ni and W remain distinguishable. In STEM images the Ni-W multilayer transitions from distinguishable layers of Ni and W to an uniform composition over a local fluence range from 0.28 to 0.34 J/cm^2. STEM images of the mixed films did not exhibit lattice contrast but NBED patterns indicate a polycrystalline film indicating that the Ni-W film was nanocrystalline or possibly approaching an amorphous microstructure.

After fs-laser irradiation of metals rapid heating and quenching via thermal transport deeply undercools molten material at the metal surface. Using other methods such as splat or melt spinning, with lower quench rates glassy and nanocrystalline metals are routinely produced. However, nanocrystalline surface layer is not observed experimentally after irradiation of pure metals which undergo much faster cooling rates. Instead the melt resolidifies epitaxially with the underlying solid material or nanocrystalline material coarsens and is consumed by large grains in the bulk material. We attempted to determine if nanocrystalline material was produced via femtosecond laser melting and stabalize it using solute stabilization of grain boundaries. It is suggested that during rapid quenching and solidification of molten Ni-W films nanocrystalline grains form, however, unlike after irradiation

of a pure metal, the nanograins are stabilized due to segregation of W to grain boundaries similar to electrodeposited nanocrystalline Ni-W films[3, 4]. Using the Ni-W system two aspects of the materials response to irradiation were considered: what fluence range heats the multilayer Ni-W films sufficiently for mixing and will the solidification of the mixed material permit forming nanocrystalline microstructure that is thermally stable. Thermally stable nanocrystalline Ni-W films were produced via laser irradiation of multilayer Ni-W films. In electrodeposited Ni-W films with an overall composition of 25% the average grain size was ~2 nm. STEM images and NBED of the laser mixed Ni-W film with an overall composition of 27% indicate very small grains and a large volume fraction of grain boundaries, consistent with the electrodeposited films.

The existence of layers of Ni and W after irradiation above the liquid spallation threshold show melting and quenching is not sufficient for mixing. It was inferred from the similarity of the removal mechanisms that the thermal and hydrodynamic response of multilayer metal films near each threshold may be similar in to the pure Ni films. It was hypothesized that as the state of the component metals pass into the vapor dome at high temperature and cool along the liquid line the state of Ni is characterized by weak interatomic interactions and high kinetic energy, favorable conditions for mixing of strongly segregating alloys. The relative importance of thermally driven diffusion and the interaction with the vapor dome in the process of mixing the Ni and W layers remains unclear.

It was then considered if the high degree of mixing that is observed in the Ni-W system can possibly be replicated in the immiscible Ni-Ag system. After irradiation the Ni-Ag film does not exhibit interface removal. The threshold for interface removal of a 24 nm thick multilayer Ni-Ag film was 0.17 J/cm^2. Near the interface removal threshold the Ni-Ag film dewets forming large droplets, in cross section STEM the droplets exhibit separate domains of Ni and Ag. To retain material irradiated with higher local fluences, in the range for mixing of Ni-W, irradiation was performed using SiO_2 or sapphire tamping layers. As with the Ni-W system melting and quenching the Ni-Ag films was not sufficient to mix the

Ni and Ag layers. It was confirmed that material melted due to the appearance of voids in the Ni substrate likely caused by intense tensile stress after irradiation, similar to intrafilm removal. At higher local fluences fluence the as-deposited layers of Ni and Ag were no longer observed, but the film did not exhibit uniform composition. Instead the Ni-Ag film exhibited separate Ni and Ag rich domains measured with z-contrast STEM, EDS mapping, and APT. There is evidence that the Ni-Ag film rapidly quenched, resolidifying epitaxially with the Ni substrate and with the [111] plane parallel to the surface. The Ni and Ag separated forming domains in the epitaxial layer leading to a single crystal mixture of Ni and Ag.

In ultrathin films where intrafilm and interface removal occur separately, it is possible to suppress the amount of material lost by liquid spallation and retain material in the intrafilm removal region that was excited with extremely high energy density. This is a simple method to study materials driven into extreme states after fs-laser irradiation using post mortem microscopy or spectroscopy methods including cross section TEM. Fs-laser mixing of ultrathin multilayer Ni-W and Ni-Ag films is a novel method to create nanocrystalline microstructures and could be applied to create nanocrystalline surface layers for a wide range of alloy compositions that possess robust mechanical properties, increased corrosion resistance, and unique magnetic properties. This method could be potentially applied to almost any alloy system; it is only necessary that the materials can be deposited in a sufficiently thin film on the same substrate. Fs-laser driven melting and solidification could also provide an alternative route to create exotic alloys, where previous work relied on vapor deposition or electrodeposition.

This dissertation seeks to modify Chemical Vapor Deposition of Carbon Nanotubes using femtosecond laser irradiation

1. Demonstrating that femtosecond laser irradiation of catalyst during CVD growth dramatically increases the terminal length of aligned CNT forests.

2. Demonstrating that the enhancement of forest growth is highly dependent on the dynamics of nucleation and growth of CNTs.

3. Identifying the mechanism for enhancement of aligned forest growth as laser stimulated nucleation of CNTs via combination of PLV and CVD synthesis.

It was shown that femtosecond laser irradiation during CVD growth can dramatically increase the area density of CNTs by activating catalyst and possibly directly stimulating CNT nucleation. It was shown that in relatively poor growth conditions, where CNTs grew in widely separated clusters, irradiation 1-3 min after the start of growth with a single pulse resulted in a higher density of CNTs forming an entangled mat. The threshold fluence to enhanced growth was 0.10 J/cm^2. Irradiation 4-6 min after the start of growth resulted in the growth of a short aligned forests. The growth of aligned CNT forests is governed by the area density of actively growing CNTs. The formation of aligned forests in the laser irradiated region shows that irradiation increased the area density above the threshold for alignment ~1x10^9 cm^{-2}. The increase in the area density of carbon nanotubes was confirmed using ex-situ TEM. It was shown that the number of CNTs per unit area was proportional to the local fluence.

When catalyst was irradiated in efficient growth conditions, sufficient for the growth of aligned forests without irradiation, irradiation caused the aligned forests to grow up to 150 X greater terminal length. Increasing the terminal length of forest growth is consistent with increasing the area density of catalyst. With a higher initial density of active catalyst it could take longer for the area density of growing CNTs to drop below the threshold for alignment; delaying forest termination leads to a longer forest. It was found that the terminal length of the forest in laser irradiated regions was very sensitive to the delay for irradiation, the maximum length of the forest was observed for irradiation 13 to 22 seconds after the start of CVD growth.

Laser stimulated CNT growth depended on having carbon nanotubes present at the time

of irradiation. In-situ optical microscopy and ex-situ SEM showed that some CNTs are removed after irradiation and that irradiation of CNTs causes emission of light. Irradiation breaks down CNTs on the catalyst surface producing an atmosphere that is likely similar to PLV of graphite, consisting of ionized carbon and carbon clusters.

Femtosecond laser stimulated CVD is a combination of the CVD and PLV methods for carbon nanotube synthesis. The short lived effects of irradiation, only nanoseconds long, increase CNT nucleation but in doing so impact CVD growth of CNTs over a period of minutes. The precise mechanism for laser stimulated nucleation of CNTs is not known, but it is reasonable that irradiation heated the catalyst and, by breaking down carbon nanotubes, produced an atmosphere rich in carbon creating conditions ideal for nucleation. It is proposed that laser heating of the catalyst in an atmosphere rich with CNT breakdown products drives a process of carbon absorption and precipitation similar to femtosecond laser driven hyperdoping. It is also possible that irradiation removed amorphous carbon from catalyst, reactivating them for CNT growth.

Enhancing CNT nucleation with the femtosecond laser provides a novel route to improve CVD growth in situations where the chamber and growth recipe are not optimized, and also compensate for natural variation in growth runs, making efficient growth of aligned CNT forests more easy to achieve. New methods to widen the range of parameters for efficient growth are critical for the widespread application of CNT based materials that are derived from aligned forests, including fibers, sheets, or coatings[5–7]. Additionally the methods demonstrated here may be used to pattern growth of aligned CNT forests without pre-pattering catalyst, masking, or post processing. It is also shown here that enhanced growth can be patterned by using diffraction or photo lithography masks to change the spatial distribution of the laser energy at the surface.

References

1. Rouleau, C. M., Shih, C.-Y., Wu, C., Zhigilei, L. V., Puretzky, A. A. & Geohegan, D. B. Nanoparticle generation and transport resulting from femtosecond laser ablation of ultrathin metal films: Time-resolved measurements and molecular dynamics simulations. *Applied Physics Letters* **104,** 193106 (May 12, 2014).
2. *Private Communication* in collab. with Torralva, B. 2016.
3. Detor, A. J., Miller, M. K. & Schuh, C. A. Solute distribution in nanocrystalline Ni-W alloys examined through atom probe tomography. *Philosophical Magazine* **86,** 4459–4475 (Oct. 1, 2006).
4. Chookajorn, T., Murdoch, H. A. & Schuh, C. A. Design of Stable Nanocrystalline Alloys. *Science* **337,** 951–954 (Aug. 24, 2012).
5. Zhang, X., Li, Q., Tu, Y., Li, Y., Coulter, J. Y., Zheng, L., Zhao, Y., Jia, Q., Peterson, D. E. & Zhu, Y. Strong Carbon-Nanotube Fibers Spun from Long Carbon-Nanotube Arrays. *Small* **3,** 244–248 (Feb. 5, 2007).
6. Zhang, M. Strong, Transparent, Multifunctional, Carbon Nanotube Sheets. *Science* **309,** 1215–1219 (Aug. 19, 2005).
7. Volder, M. F. L. D., Tawfick, S. H., Baughman, R. H. & Hart, A. J. Carbon Nanotubes: Present and Future Commercial Applications. *Science* **339,** 535–539 (Feb. 1, 2013).

CHAPTER 9

Future Work

9.1 Higher Time Resolution of the Dynamics of Removal at an Interface

It was shown in Chapter 4 that the interface and intrafilm layers separate from the Ni substrate and accelerate to their final velocity within 50 ps. During the process of critical point phase separation the vapor phase forms homogeneously in the melt within several ps[1, 2]. Future work should determine if the metal substrate interface separates on the same timescale as critical point phase separation in bulk using pump-probe microscopy methods with higher temporal resolution. The current method, using a probe wavelength of 390 nm and a 45°, can be used to measure displacements on the order of 100 nm. Because the interface removal layer has a velocity of 300 to 700 m/s, depending on the local fluence, the first measurable extrema is observed 300 to 150 ps after irradiation respectively. The displacement of the ejected layers could not be measured with accuracy on timescales shorter than the generation of thin film interference extrema, so separation of the film at earlier times is inferred from changes in reflectivity or by extrapolation of the linear fit. Higher resolution of the film displacement is required to define the timescale for separation at the interface. A pump-probe Linnet imaging interferometer has been used previously to study ablation via liquid spallation of bulk metals and semiconductors[3]. The height resolution of the interferometer was reported to be on the order of 1 nm. In future experiments using

an imaging interferometer, the timescale for separation of the Ni-glass interface should be determined at the threshold for interface removal. At the interface removal threshold the velocity of the interface removal layer is approximately 200 m/s, this was determined using a linear extrapolation of the interface removal velocity vs. fluence in Figure 4.12. If it is assumed that the velocity of the ejected layer is constant after separation, as indicated in Chapter 4, the displacement could be measured with resolution of 5 ps, two orders of magnitude greater time resolution than Newtons rings.

An alternative mechanism has been proposed for interface removal of Ni thin films; the heterogeneous formation of vapor at the interface severs the Ni-glass interface, but the Ni vapor is not at high pressure and does not cause the film to accelerate away from the substrate, instead the Ni film is ejected as the surface of the glass substrate "rebounds" after the strain wave passes through the interface. Future work using should distinguish between interface removal via the vapor expansion or the glass substrate "rebound" mechanism by measuring the acceleration of the interface removal layer after separation. Separation of the Ni film due to the rebound of the substrate should have no measurable acceleration. Acceleration due to the pressure of vapor in the gap between the layer and the substrate should take longer.

This dissertation has focussed on the removal of Ni from glass substrates. It was proposed that Ni vapor formed by spinodal-like decomposition was stabilized by reducing the interfacial free energy between the liquid Ni and the substrate. Future work should determine if the free energy of the metal-substrate interface significantly effects the interface removal threshold. In future work a selection of metal thin films should be deposited on different substrates, irradiated, and then the threshold for interface removal should be measured. If fluctuations in density can drive heterogeneous nucleation over a range of temperatures within the the vapor dome one should find that the threshold for interface removal is inversely related to the interfacial free energy. For each film-substrate combination a hydrodynamic simulation should be performed to determine at what temperature the

thin metal film enters the vapor dome in the temperature-density phase diagram after irradiation. Simulations of each substrate would be performed to account for the differences in how pressure evolves near the film-substrate interface, since each film and substrate have a different impedance mismatch, and determine the temperature of the metal in the vapor dome.

9.2 Determine the Removal Mechanisms of Ni Films Where Intrafilm Removal is Not Observed Post Mortem

The threshold fluences for interface and intrafilm removal of Ni thin films on glass substrate converge as the thickness of the Ni film is reduced. It has been suggested previously that at very small film thicknesses only interface removal is observed because the tensile stress in the film cannot develop a deep tensile trough and cavitation cannot occur in the liquid layer, Instead only interface removal via the heterogeneous nucleation of vapor occurs. Future work should include pump-probe microscopy to determine if cavitation occurs in the liquid film at local fluences higher than the interface removal threshold. In that case the Ni film would be removed with the configuration shown in Figure 9.1. Using pump-probe microscopy of Newton's Rings it would be possible to distinguish the separate removal layers despite the fact they are not visible post mortem.

In this dissertation, pump probe microscopy showed the existence of a third layer removed from Ni after irradiation above a threshold fluence of 0.09 J/cm^2. The velocity of the ejected layer was 1680 $\pm$ 100 m/s after irradiation at a local fluence of 0.14 J/cm^2. In the removal area there was no change in the reflectivity of the Ni film. It was not possible to identify the removal crater using optical microscopy. Newton's rings corresponding to the third film could not be generated with a second shot, strongly indicating that a physical layer was removed and that the fringes were not generated by surface vaporization, a shockwave, or any other nondestructive and repeatable phenomenon. It is suggested that

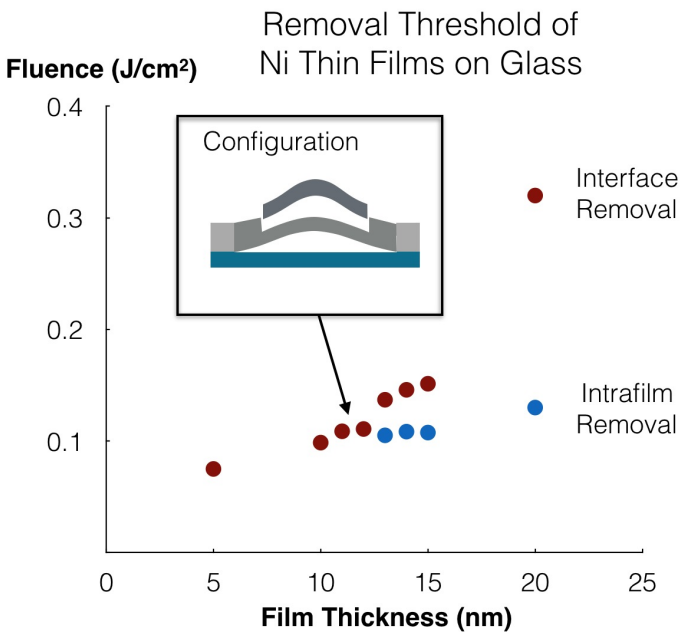

Figure 9.1: Thresholds for interface and intrafilm removal vs thickness for Ni thin films on glass substrates. Thresholds for removal of Ni thin films were measured using post-mortem optical microscopy. The intrafilm and interface thresholds converge as the film thickness decreases. It is possible that intrafilm removal still occurs by liquid spallation for films less than 13 nm thick, but above a higher threshold fluence. A schematic cross section of the possible configuration of layers ejected after irradiation above the threshold for liquid spallation of films less than 13 nm thick is shown.

the removed layer is the Ni native oxide. This is consistent with a vanishingly small impact on the reflectivity of the layer in optical microscopy and the ablation of a layer of material. Future work should be performed to confirm the composition of the third removed. The surface of Ni at the edge of the removal region should be examined using AFM confirming the existence of a step edge. Pump-probe microscopy of the same area on a Ni film should be performed a second time after a long enough period to grow a native oxide layer to see if another film is ejected. Machining of native oxide layers could provide a route for machining metals and semiconductors with vertical resolution on the nanometer length scale.

9.3 Determining The Role of Extreme Thermodynamic States in Mixing Multilayer Metal Films

We do not know the relative importance of laser driven extreme states, including entering the vapor dome or relaxation along the liquid line, compared to the thermally driven diffusion of atoms in the melt. The two parameters are difficult to isolate because the extremely high temperatures, on the order of 8000 K are essentially impossible to produce in any other conditions to use as a comparison. After irradiation of a tamped metal film the pressure at the film-tamper interface does not fall to zero, as it would in the case of a free surface. As a result of the positive pressure at the surface the relaxation path changes such that it does not penetrate the vapor dome as deeply or remain there for a very long time, as shown in Figure 9.2.

Future work should attempt to decouple the effects of the vapor dome and thermal diffusion at high temperatures by preventing the expansion of the multilayer film after irradiation. By manipulating the depth of the metal layer, adding tampers, and varying the substrate and tamper materials the material can be heated without coming into contact with the vapor dome. Multilayer Ni-W films should be tamped with 1.5 μm to replicate the relaxation pathways shown in Figure 9.2. The effectiveness of mixing the Ni-W layers with a tamping layer, and consequently without significant interaction with the vapor dome, should be compared with the case of an untamped Ni-W film. The same methodology must also be applied to a suitable case with Ni-Ag where the vapor dome is theoretically more critical to mixing because Ni and Ag readily phase separate.

It was observed after the irradiation of multilayer Ni-Ag thin films with thick Ni substrates that voids form in the Ni substrate, as shown in Figures 6.6, 6.4, and 6.1. At high fluences the void have a diameter of up to 200 nm. The sapphire tamper is not deformed by irradiation. The creation of voids causes the Ni substrate to bend, forming a blister. The melting temperature of Ag is significantly less than Ni, it is reasonable that critical tem-

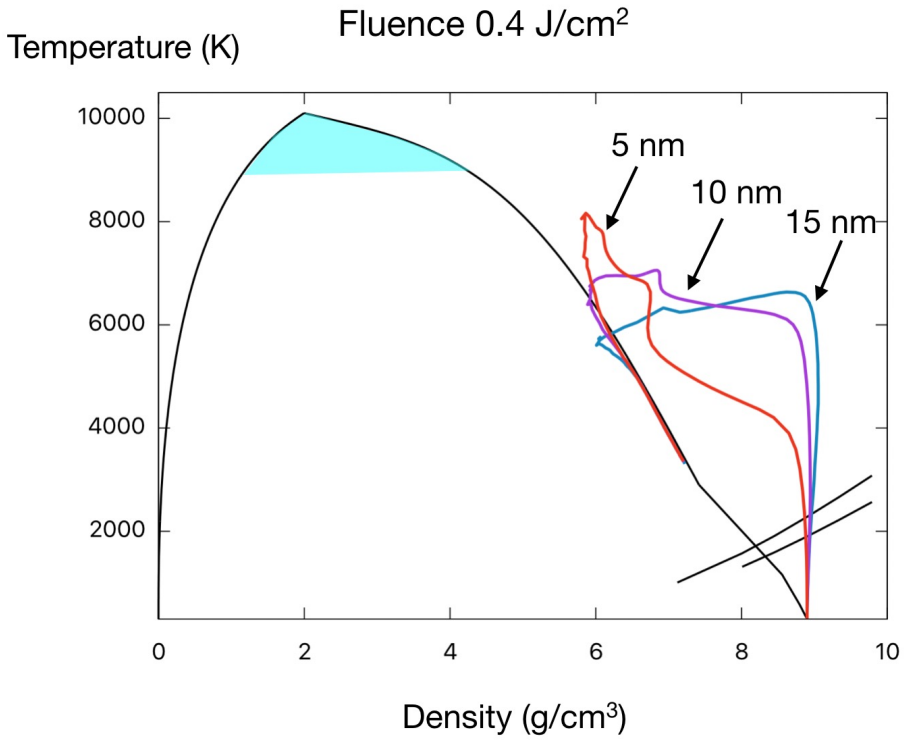

Figure 9.2: Hydrodynamic simulations of ultrathin Ni film after irradiation with glass tamping layer. The trajectories are shown for several depths within a 20 nm Ni film after irradiation with a 1.5 μm glass tamper. The positive pressure maintained at the Ni-tamper interface leads material not to penetrate the vapor dome as deeply as in previous simulations of untamped Ni films, shown in Figure 4.14. Reprinted with the permission of Ben Torralva.

perature of the vapor dome is also significantly lower. The extreme plastic deformation of the Ni layer at modest peak fluence could indicate that the silver film is entering the vapor dome and decomposing into liquid and vapor, creating high pressure at the interface with the sapphire tamper, and forming the blister. Future work should investigate the mechanism for forming a large blister by irradiating thick Ni films through the sapphire tamper that have no silver at the interface, the Ni-Ag multilayer film at the interface, and a pure Ag layer at the interface. The height of blister should be determined for each composition for the same absorbed fluence.

9.4 Laser Mixing of Multilayer Films: Varying Composition

In Chapter 5 of this dissertation mixing of multilayer Ni-W films was studied for only an overall composition of 27 at% W. In previously studied electrodeposited films the average grain size at this composition was several nanometers. The very small grain size and relatively thick STEM samples made it impossible to see the lattice contrast of nanograins and measure their size directly. Future work should investigate fs-laser mixing of Ni-W films with a range of W composition. It should be determined if the average grain size in the irradiated Ni-W film increases with decreasing W concentration similar to electrodeposited Ni-W[4]. If it is found in the course of that work that that the size of nanograins is not significantly affected by W composition, the grain size could be determined only by the density of homogeneous nuclei during rapid solidification of the the fs-laser melted film.

The microstructure of laser irradiated Ni-W should be studied using X-Ray Diffraction (XRD) or plan view TEM. This dissertation suggests that future experiments regarding mixing of multilayer films not be performed using a substrate material that is similar to material of interest, e.g. Ni should be avoided when studying Ni-W or Ni-Ag layers. It was found that intrafilm and interface removal of multilayer Ni-W films occurs on both Ni

substrates, as shown in this dissertation and on glass substrates. Ni-W films directly on glass substrates exhibited intrafilm and interface removal above threshold fluences of 0.15 and 0.29 J/cm^2 respectively. Because thermal transport into the glass substrate is limited, this dissertation suggests using a sapphire substrate. The probe size for XRD is ~1 mm. To produce a large enough area for XRD characterization it would be necessary to pattern an area with laser spots. This dissertation suggests using a square, flat-top beam to create a uniform pattern of laser irradiation to mix the Ni-W film. Alternatively it is possible with the laser used in this work to reach a peak fluence of 0.5 J/cm^2 using a 1/e^2 spot 500 μm in diameter. An area nearly 350μm in diameter would be mixed after irradiation, possibly sufficient for XRD characterization.

Two methods could be used in future work to examination laser mixed Ni-W using plan view TEM. A plan view liftout of a multilayer Ni-W film on a sapphire substrate could be created or a multilayer film of Ni-W could be deposited on a substrate that could be dissolved, for instance on salt. After irradiation the substrate material could be dissolved, freeing the Ni-W layer. The NiW film could then be collected on a TEM grid and examined using STEM, TEM, and Selected Area Diffraction (SAD). SAD would provide a significant advantage over NBED in determining the microstructure of mixed Ni-W. It should be determined nanograins in the mixed film correspond to Ni to confirm whether the Ni-W film exhibits solute stabilization of grain boundaries.

Ni-Ag films investigated in Chapter 6 had a composition of 50 at% Ag. This composition is near the peak of the monotectic and will therefore be the most difficult to form, will most readily phase separate, and will expel the most heat as it cools and phase separates almost ensuring that the Ni and Ag will not remain mixed. Future work should attempt to mix Ni-Ag for a range of lower compositions of Ag. It should be investigated if a uniform mixture of Ni-Ag can be synthesized by laser irradiation if the enthalpy of mixing is lower.

APT is becoming a standard method to examine the microstructure of nanocrystalline alloys. APT of fs-laser mixed Ni-W films should be performed and compared with previous

studies of electrodeposited Ni-W[5]. APT of Ni-Ag after irradiation was seriously complicated by the drastically different evaporation fields of Ni and Ag. Future work should replicate fs-laser mixing of multilayer films using an immiscible metal system where the components have similar evaporation fields. Candidate immiscible systems [6–8] should be selected to minimize the difference in the evaporation field of each species[7]. The Cu-Co system may be acceptable, the evaporation field of Co is 6% higher than Cu. For comparison, the evaporation field of Ag is 33% higher than Ni.

9.5 Determining the Mechanism for Fs-Laser Stimulated CNT Nucleation

The precise mechanism of laser stimulated nucleation of CNTs is uncertain. One possible explanation is that absorption of carbon by causes catalyst to dewet, forming the nanoparticles necessary to nucleate nanotubes. In previous studies using in-situ TEM, nanoparticles transitioned from broad scales of partially reduced FeO to distinct nearly spherical nanoparticles after the introduction of carbon with the growth gas[9]. Future work should investigate to determine if the PLV of existing nanotubes provides a source of carbon to dewet catalyst at an earlier time or with an increased population. TEM foils like in Figure 7.3 should be irradiated with a single pulse shortly after the introduction of carbon and the initiation of some CNT growth. After irradiation growth should be stopped immediately. Using conventional TEM the shape of catalyst in the irradiated and pristine regions should be observed to determine if a larger population of fully formed catalyst nanoparticles exists in the irradiated region.

Future work should determine if the products of laser breakdown of CNTs play the primary role in laser enhanced nucleation, as opposed to laser induced heating. First, the products of laser induced breakdown of CNTs should be examined using optical spectroscopy of the ablation plume shown in Figure 7.12. In previous studies the emission of

blackbody radiation was associated with larger carbon clusters >50 atoms and emission of characteristic wavelengths and radiation in the swan bands was associated with carbon ions and radicals [10]. It is very likely that carbon ions and radicals would contribute to growth of CNTs, while large carbon cluster would not[11]. Second, the role of PLV carbon in CNT nucleation could be further explored by introducing carbon breakdown products to the catalyst during growth. A pure target of graphite or compacted carbon nanotubes could be placed in the furnace next to the catalyst. The surface of the carbon target would be directed toward the catalyst surface then irradiated at grazing incidence to produce a plume of laser breakdown products. The plume could be introduced early in the CVD growth step for a brief period, as in experiments shown in Chapter 7, and the resulting growth would be compared with laser irradiation of the catalyst.

Future work should determine if absorption of laser light in the catalyst nanoparticles plays a role in laser stimulated nucleation of CNTs. In Figure 7.7 the terminal length of CNT stalks sharply declines for irradiation 22 seconds after the start of growth. This reduction was not associated with the possible role of carbon breakdown products, with increasing time the amount of available carbon continues to increases. It was speculated that the reduction in terminal length of the forests was caused by the organization of a CNT forest that prevented the laser light from reaching the catalyst. The relationship of absorbed fluence in the catalyst vs forest height should be investigated. The amount of light incident on the catalyst should be measured during growth by measuring the reflectivity of the catalyst as CNTs grow. Further, the temperature of catalyst nanoparticles should be calculated as a function of the absorbed intensity.

The technique of laser stimulated nucleation of CNTs would be most effectively understood by performing in-situ femtosecond laser irradiation of CNTs in an environmental TEM holder where CNTs can be produced by CVD growth. The structure of the catalyst could be monitored before and after irradiation verifying that the laser either causes nanoparticle formation or that irradiation drives a phase change in the nanoparticle. A

transformation of the catalyst to a phase with higher carbon solubility could be monitored using HR TEM or Selected Area Diffraction of catalyst in the laser spot. It could also be determined if CNTs must exist on the surface, as was suggested in Chapter 7.

9.6 Practical Applications of Laser Stimulated Nucleation of CNTs

A parametric study of the effect of irradiation on CNT growth should be performed with respect to common factors such as the growth gases and growth temperature. It is important that the efficacy of laser irradiation as a route to improve growth in poorly controlled systems is understood. The addition of a simple step such as laser irradiation to dramatically increase the efficiency of CVD growth of CNT has a substantial economic impact.

Techniques for patterning of laser stimulated growth should be developed. Patterning of CNT growth with a photomask was demonstrated serendipitously, but should be replicated with forest growth. Irradiation and enhancement of forest terminal length through a mask could make it possible to produce complicated 3D CNT structures. A single fs-laser exposure could be used to replace the messy and time consuming process of photolithography[12].

References

1. Povarnitsyn, M. E., Itina, T. E., Sentis, M., Khishchenko, K. V. & Levashov, P. R. Material decomposition mechanisms in femtosecond laser interactions with metals. *Physical Review B* **75,** 235414 (June 2007).
2. Vidal, F., Johnston, T. W., Laville, S., Barthélemy, O., Chaker, M., Le Drogoff, B., Margot, J. & Sabsabi, M. Critical-Point Phase Separation in Laser Ablation of Conductors. *Physical Review Letters* **86,** 2573–2576 (Mar. 19, 2001).
3. Vasily V. Temnov. *Ultrafast Laser-induced Phenomena in Solids Studied by Time-resolved Interferometry* PhD thesis (University of Duisburg-Essen, May 2004).
4. Detor, A. & Schuh, C. Tailoring and patterning the grain size of nanocrystalline alloys. *Acta Materialia* **55,** 371–379 (Jan. 2007).
5. Detor, A. J., Miller, M. K. & Schuh, C. A. Solute distribution in nanocrystalline Ni-W alloys examined through atom probe tomography. *Philosophical Magazine* **86,** 4459–4475 (Oct. 1, 2006).
6. Ma, E. Alloys created between immiscible elements. *Progress in Materials Science* **50,** 413–509 (May 2005).
7. Wang, F. E. *Bonding Theory for Metals and Alloys* 219 pp. (Gulf Professional Publishing, Sept. 30, 2005).
8. Ratke, L. & Diefenbach, S. Liquid immiscible alloys. *Materials Science and Engineering: R: Reports* **15,** 263–347 (Dec. 15, 1995).
9. Bedewy, M., Viswanath, B., Meshot, E. R., Zakharov, D. N., Stach, E. A. & Hart, A. J. Measurement of the Dewetting, Nucleation, and Deactivation Kinetics of Carbon Nanotube Population Growth by Environmental Transmission Electron Microscopy. *Chemistry of Materials* **28,** 3804–3813 (June 14, 2016).
10. Amoruso, S., Ausanio, G., Vitiello, M. & Wang, X. Infrared femtosecond laser ablation of graphite in high vacuum probed by optical emission spectroscopy. *Applied Physics A* **81,** 981–986 (Oct. 2005).
11. Geohegan, D. B., Puretzky, A. A., Rouleau, C., Jackson, J., Eres, G., Liu, Z., Styers-Barnett, D., Hu, H., Zhao, B. & Ivanov, I. in *Laser-Surface Interactions for New Materials Production* 1–17 (Springer, 2010).
12. De Volder, M. & Hart, A. J. Engineering Hierarchical Nanostructures by Elasto-capillary Self-Assembly. *Angewandte Chemie International Edition* **52,** 2412–2425 (Feb. 25, 2013).

APPENDIX A

Microscopy Methods

A.1 Optical Microscopy

Optical images were collected using a Zeiss Axiotron 2 or Nikon Optiphot. Scale bars for the different microscopes and objectives were calibrated using a stage micrometer for transmitted and reflected light (Ted Pella PN 2280-13).

Images of laser induced damage spots were collected using Nomarski differential interference contrast mode. Nomarski contrast was sufficient to resolve ~20 nm deep damage craters. Optical images of carbon nanotubes were collected using dark field, for example in Figure 7.9. The carbon nanotube forests are very efficient light absorbers, in bright field or Nomarski contrast the topography of CNT forests could not be resolved. A sufficient amount of light is scattered for very clear dark field images to be collected. Dark field images would have been a sufficient alternative to SEM imaging of CNT forests for most purposes including the measurement of CNT stalk height as in Figure 7.7. Optical images of removal of Ni thin films on glass substrate were collected using bright field. The thinner Ni film after intrafilm removal was darker than the surrounding 20 nm film. The interface removal region appeared dark since the illumination was transmitted through the glass substrate. The three tones of contrast in the area of laser damage made it easy to measure the area of the intrafilm and interface removal regions.

A.2 Atomic Force Microscopy

Atomic force microscopy is a scanning probe technique that is used to determine the height of nanostructures. AFM was used to measure the depth of removal craters in Ni, Ni-W, and Ni-Ag films. A Bruker Dimension ICON AFM at the Michigan Center for Materials Characterization in the North Campus Research Complex was used. Measurements were taken using ScanAsyst® mode, a peak force tapping mode that automatically and continuously changes the acquisition parameters of the AFM including the set point amplitude and peak force. In ScanAsyst® mode ScanAsyst tips were used (Bruker SKU: SCANASYST-AIR). Using Nanoscope® Analysis by Bruker, AFM scans were flattened and line profiles of removal craters were collected.

A.3 Scanning Electron Microscopy

SEM images were collected using an FEI Helios 650 NanoLab SEM/FIB at the Michigan Center for Materials Characterization in the North Campus Research Complex. The instrument provides ~10 nm spatial resolution during regular operation using single lens mode and the Everhart-Thornley detector. For imaging of CNT stalks an accelerating voltage of 5 kV was used. Higher accelerating voltages caused a large proportion of the beam to be transmitted through the CNTs making them appear partially transparent. The resolution could be increased by using immersion mode to increase the collection efficiency of the detector, FEI advertises a maximum spatial resolution of 6 nm. Before imaging alignment of beam center, the condenser aperture, and stigmator lenses were performed.

A.4 Conventional High Resolution Transmission Electron Microscopy

High resolution conventional TEM was used to characterize CNTs. HRTEM images were collected using a JOEL 3100C located at the Michigan Center for Materials Characterization in the North Campus Research Complex. An accelerating voltage of 300 kV was used.

To measure the distribution of diameters and wall thicknesses of CNTs after growth from pristine and laser irradiated catalyst, as shown in Figure 7.10, CNTs were distributed onto 300 Mesh copper TEM grids with a lacey carbon film (Ted Pella PN 01895). Imaging was performed using a defocus of 100 nm to resolve the interior and exterior edges of the nanotubes. Because the stalks of CNTs produced in the irradiated areas were so small CNTs were not distributed in a solvent and sonicated before being distributed on TEM grids. The CNTs from each area were plucked off the catalyst using tweezers and placed on separate grids dry. As a result the CNTs were not lying on a flat plane for HRTEM imaging. Despite a large concentration of CNTs only a few nanotubes were in focus in each image. In the future, if larger areas of the catalyst could be irradiated and larger amounts of CNTs could be produced from those areas, TEM grids should be prepared by sonicating the CNTs in a solvent and then distributing them onto the TEM grid by either sweeping the grid through the solution or dropping solvent onto the grid. A larger number of measurements could be made, and therefore better statistics could be gathered regarding the differences of CNTs in the pristine and laser irradiated areas of catalyst.

In Section 7.2 catalyst was deposited on electron transparent SiO_2 support films (Ted Pella PN 21530-10). Each grid has 24 50x50 μm square windows. CNTs were grown directly on the windows and the catalyst was irradiated during growth. Images of the TEM windows were collected using the JOEL 3100C with an accelerating voltage of 300 kV. Low magnification mode was used to capture images at 5000X, this way an entire 50

micron square window could be captured in a single image. To generate enough contrast from CNTs on the surface at low magnification a defocus of 2000 nm was used. With such a large defocus the diameter of nanotubes was greatly exaggerated. However only the density of nanotubes was of interest, separate nanotubes could be identified on the surface because the area density of active catalyst was low, even in irradiated regions. It is probable that CNT growth on the surface of the SiO_2 grids was low because the temperature of the grids was lower than the intended 750 °C. It is likely that the SiO_2 thin film exhibits low thermal conductivity limiting heat transport from the edges of the Si wafer support and that very little of the infrared light emitted from the Si carrier beneath the grid is absorbed by the transparent SiO_2 window. Additionally the thin suspended SiO_2 window will exhibit more efficient radiative cooling than a bulk Si/SiO_2 support that was used in all other experiments.

A.5 Scanning Transmission Electron Microscopy

High resolution cross section Scanning Transmission Electron Microscopy (STEM) of pristine and irradiated multilayer Ni-W and Ni-Ag films was performed using two microscopes. A JOEL 2100F was used with an accelerating voltage of 200 kV and a JOEL 3100C was used with an accelerating voltage of 300 kV. The microscopes were located at the Michigan Center for Materials Characterization in the North Campus Research Complex. The STEM was operated using camera length of 15 cm and with spot size 7c. The High Angle Annular Dark Field (HAADF) and Bright Field (BF) detectors were both used. The HAADF detector primarily shows mass/thickness contrast, also called z-contrast, where the signal increases for areas of the sample with greater thickness or that contain a larger concentration elements with higher atomic number. For example, in HAADF images of Ni-Ag samples with uniform thickness the brightness increases with increasing concentration of Ag. Bright field images show a combination of mass/thickness contrast and diffraction

contrast. In general with thicker samples or in a dirty microscope, bright field contrast better shows lattice contrast caused by atomic planes and columns in crystals. FFTs of bright field images were used to measure interplanar spacing and zone axes.

STEM samples of pristine materials were prepared by mechanical grinding and polishing. Samples of the pristine multilayer Ni-W and Ni-Ag films were cleaved and then glued together using M-Bond™ 610 (Ted Pella PN 16039). with the metal films in contact. final thinning and polishing was performed using a Gatan 691 Precision Ion Polishing System (PIPS) with an incident angle of 2 degrees, ion beam energy of 4.5 eV, and cryogenic cooling. Samples in the laser irradiated region were prepared using Focused Ion Beam (FIB) in-situ liftout[1, 2]. The exact voltages and beam current used for FIB liftout varied with the substrate material, but the general parameters of the procedure used in this work are given in References[3, 4]. Final polishing was performed at an incident angle of 2 degrees, an ion beam energy of 2 eV, and ~1pA/μm^2.

A.6 Nanobeam Electron Diffraction

Nano-beam Electron Diffraction (NBED) of the irradiated multilayer Ni-W and Ni-Ag films was performed using a JOEL 3100C. The microscope was operated in STEM mode at 300 kV. The size of the condenser aperture was reduced and the condenser Mini lens setting was modified to create an electron probe semi-angle of 3 milliradians, sufficient to distinguish individual diffraction spots from Ni, Ag, or W. The STEM probe was 2-10 nm in diameter depending on the alignment of the microscope. NBED patterns contain disks instead of sharp spots because the beam is focused not parallel[5].

A.7 Atom Probe Tomography

Samples for atom probe tomography of irradiated Ni-Ag films were prepared using the FIB liftout technique[6]. Liftout was performed using the FEI Helios 650 NanoLab SEM/FIB

located at the Michigan Center for Materials Characterization in the North Campus Research Complex. The Ni-Ag films were deposited directly on a sapphire tamper, in this case a 500 μm thick wafer, then the 1.5 μm thick Ni substrate layer was sputter deposited on the Ni-Ag layer. To maintain a consistent discussion of the sample response the substrate material is defined as in the positive direction from the irradiated surface with respect to the propagation direction of the laser beam. Liftout had to be performed through the Ni tamping layer, but laser damage spots were only visible through the sapphire tamper. In order to locate the irradiated spot during liftout fiducial marks were machined through the Ni-Ag/Ni with the fs-laser before irradiation with a single pulse. The fiducial marks were 100 microns away from the irradiated area for TEM or APT examination to prevent modification of the pristine layers. Images of the modified laser spot were collected using optical microscopy thought the sapphire substrate then overlaid with ion beam images gathered during liftout to locate and extract the laser modified area.

A lamella 25 μm wide, 2μm thick, and 5μm deep was extracted for TEM and APT. One half of the lamella was used to create atom probe specimens while the other half was used for cross section STEM. Sections of the lamella 2 μm wide, 2μm thick, and 5μm deep were placed on Si posts. The sapphire tamper was between the Ni-Ag/Ni film and the Si support post. It was attempted to produce specimens with a shank angle of ~5° to prevent fracture of the tips because of the insulating sapphire. The final specimens were prepared by a series of annular milling steps using 30 kV, and final polishing with 5 kV at ~2pA/μm^2. Polishing was ended when the specimen appeared to have 50nm of the Ni Substrate remaining at the tip.

APT was performed on a Cameca LEAP 4000X HR in laser mode using a pulse energy of 40 pJ, a detection rate of 5 atoms per 1000 pulses, a base temperature of 50 K, and a pulse rate of 160 kHz. APT reconstructions and analyses were performed using Cameca IVAS version 3.6.12. The volumetric reconstruction was created using the voltage evolution method assuming an initial tip radius of 30 nm and the evaporation field of Ni of 35 V/nm.

The image compression factor and geometric factor were left at their default values of 1.65 and 3.30, respectively, as no additional information to adjust the reconstruction was available.

References

1. Giannuzzi, L. A. & Stevie, F. A. A review of focused ion beam milling techniques for TEM specimen preparation. *Micron* **30,** 197–204 (1999).
2. *Introduction to focused ion beams: instrumentation, theory, techniques, and practice* (eds Giannuzzi, L. A. & Stevie, F. A.) (Springer, New York, 2005). 357 pp.
3. Schaffer, M., Schaffer, B. & Ramasse, Q. Sample preparation for atomic-resolution STEM at low voltages by FIB. *Ultramicroscopy* **114,** 62–71 (Mar. 2012).
4. Myers, B. *TEM Sample Preparation with the FIB/SEM* (http://www.nuance.northwestern.edu/docs/epic-pdf/TEM%20Sample%20 Preparation_BDM_2009_abridged.pdf, NUANCE Center, 2009).
5. Williams, D. B. & Carter, C. B. *Transmission Electron Microscopy* (Springer US, Boston, MA, 1996).
6. McKenzie, W. R., Marquis, E. A. & Munroe, P. R. Focused ion beam sample preparation for atom probe tomography. *Microscopy: Science, Technology, Applications and Education* **3,** 1800–1810 (2010).

APPENDIX B

Analysis of CNT Coverage After Irradiation of CNT Foil

B.1 Preparing Images with Image J

HRTEM images of catalyst on SiO_2 TEM windows were gathered after CVD growth. A 2000nm defocus was used to increase the contrast from CNTs. The diameter of nanotubes was greatly exaggerated, however, only the density of nanotubes was of interest. Separate nanotubes could be identified on the surface because the area density of active catalyst was low, even in irradiated regions. Images were imported into ImageJ. The images were cropped to 1460x1460 pixels corresponding to real dimensions of 50x50 μm. The brightness and contrast of the images was enhanced. A fourier filter was applied with a pass band of 7 - 40 1/pixels. The contrast was enhanced to saturate 0.4% of pixels. A threshold image was extracted and converted to binary that included all the CNTs. The binary image was skeletonized to represent the CNTs as single pixel lines. The actual CNTs have a diameter less than the real pixel dimension of ~35 nm.

B.2 Matlab Code to Construct Histogram of CNT Coverage with Respect to Fluence

The following code determines where a non-zero pixels exist in the HRTEM images after processing with ImageJ, determines the location of those pixels in the array of SiO_2 windows, and compares those locations with a map of the local fluence. The size of images must be 1460x1460 pixels. The scale is 0.0342 μm/pixel. The total coordinate space encompasses all the windows and the Si_3N_4 support grid, as shown in Figure 7.3. The SiO_2 windows in HRTEM images were overlaid with the optical image of the Si_3N_4 grid and windows in Figure 7.3. The coordinate of the upper left corner of each window was measured. An optical image of the catalyst underneath the TEM grid exhibiting visibly enhanced CNT growth in each laser spot was overlaid with the optical image of the Si_3N_4 grid and windows. The coordinate of the center of each laser spot was measured.

rx=Laser radius minor axis

ry=Laser radius major axis

corners=coordiantes of the upper left corner of the windows

centroids=coordiantes of the center of laser spots

fileindex=variable representing the index of each SiO_2 window in a directory

binsize= number of binsof fluence for histogram, 60 for data in Figure 7.4

xshift and yshift= tool to reposition spots and corners, set to zero.

```
function data=counting(rx,ry,corners,centroids,fileindex,
   binsize,xshiftcent,yshiftcent)

%close all

bins(1,:)=linspace(0,.20,binsize);
```

```
bins(2,:)=zeros(1,binsize);

for im=1:24
im

formatSpec = '%d coverage.txt';
imagefile=sprintf(formatSpec,fileindex(im));
image = importdata(imagefile);
image(image>0) = 1;


FmatrixXindex=repmat(linspace(corners(1,im),corners(1,im)
   +1459,1460),1460,1);
FmatrixYindex=repmat(linspace(corners(2,im),corners(2,im)
   +1459,1460).',1,1460);
Fmatrix=zeros(1460);

%create map of fluence distribution for all 24 windows
Fo=0.2;
theta=3.14159*83/180;
a=cos(theta)^2/(2*rx^2)+sin(theta)^2/(2*ry^2);
b=sin(2*theta)/(4*rx^2)-sin(2*theta)/(4*ry^2);
c=sin(theta)^2/(2*rx^2)+cos(theta)^2/(2*ry^2);
for i=1:20;
        dose=Fo.*exp(-(a.*(FmatrixXindex-centroids(1,i)+
           xshiftcent).^2-2.*b.*(FmatrixXindex-centroids(1,i
           )+xshiftcent).*(FmatrixYindex-centroids(2,i)+
```

```
            yshiftcent)+c.*(FmatrixYindex-centroids(2,i)+
            yshiftcent).^2));
        Fmatrix=max(Fmatrix,dose);
end

%plotting heat map of radiation and cnts
imagesizes=size(image);
imagexsize=imagesizes(1);
imageysize=imagesizes(2);
if imagesizes==size(Fmatrix)
    figure;
hold on
mesh(FmatrixXindex,FmatrixYindex,Fmatrix);
view(2);
axis equal;
mesh(FmatrixXindex(1:imagexsize,1:imageysize),FmatrixYindex
   (1:imagexsize,1:imageysize),image.*0.3);
hold off
else
end
%end plotting

%counts image pixels that are non zero and records the local
    fluence
sizes=size(image);

for i=1:sizes(1);
```

```
    for j=1:sizes(2);
    if image(i,j)>0;
        binstemp=abs(bins(1,:)-Fmatrix(i,j));
        [M,I]=min(binstemp);
        bins(2,I)=bins(2,I)+1;
    end
    end
end
end
data=bins.';

%plot histogram data
figure;
plot(bins(1,:),bins(2,:));
```